

**HUNGARIAN**

**AGRICULTURAL**

**ENGINEERING**







HUNGARIAN  
ACADEMY  
OF SCIENCES

# Hungarian Agricultural Engineering

N<sup>o</sup> 42/2023

*Editors-in-Chief:*  
Dr László TÓTH  
Dr. István SZABÓ

*Secretary of Editorial board:*  
Dr. László MAGÓ

*Editorial Board:*

Dr. David C. FINGER  
Dr. György SITKEI  
Dr. Gábor KESZTHELYI-SZABÓ  
Dr. László TÓTH  
Dr. János BEKE  
Dr. István SZABÓ  
† Dr. István J. JÓRI  
Dr. Béla HORVÁTH  
Dr. Péter SEMBERY  
Dr. László FENYVESI  
Dr. László KÁTAI  
Dr. Zoltán BÁRTFAI  
Dr. László MAGÓ  
Dr. Bahattin AKDEMIR  
Dr. R. Cengiz AKDENIZ  
Dr. József NYERS  
Dr. Mičo V. OLJAČA  
Dr. Zdenek PASTOREK  
Dr. Vijaya G.S. RAGHAVAN  
Dr. Lazar SAVIN  
Dr. Bart SONCK  
Dr. Goran TOPISIROVIĆ  
Dr. Valentin VLADUT

**PERIODICAL OF THE COMMITTEE OF  
AGRICULTURAL AND BIOSYSTEM  
ENGINEERING OF THE  
HUNGARIAN ACADEMY OF SCIENCES**

Published by

**Hungarian University of  
Agriculture and Life Sciences  
Institute of Technology  
H-2103 Gödöllő, Páter K. u. 1.**



HUNGARIAN UNIVERSITY OF  
AGRICULTURE AND LIFE SCIENCES

Institute of Technology

**Gödöllő  
2023**

*Technical Editor:* Dr. László MAGÓ

**Published online: <http://hae-journals.org>  
HU ISSN 0864-7410 (Print)  
HU ISSN 2415-9751(Online)**

# PREFACE

In the name of the Committee of Agricultural and Biosystem Engineering of the Hungarian Academy of Sciences we would like to welcome everyone who is interested in reading our journal. The Hungarian Agricultural Engineering (HAE) journal was published 35 years ago for the very first time with an aim to introduce the most valuable and internationally recognized Hungarian studies about mechanisation in the field of agriculture and environmental protection.

In the year of 2014 the drafting committee decide to spread it also in electronic (on-line and DOI) edition and make it entirely international. From this year exclusively the Hungarian University of Agriculture and Life Science's Institute of Technology (former Szent István University's Faculty of Mechanical Engineering) took the responsibility to publish the paper twice a year in cooperation with the Hungarian Academy of Sciences.

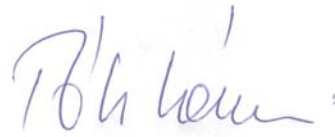
Our goal is to occasionally report the most recent researches regarding mechanisation in agricultural sciences (agricultural and environmental technology and chemistry, livestock, crop production, feed and food processing, agricultural and environmental economics, energy production, engineering and management) with the help of several authors. The drafting committee has been established with the involvement of outstanding Hungarian and international researches who are recognised on international level as well. All papers are selected by our editorial board and a triple blind review process by prominent experts which process could give the highest guarantee for the best scientific quality.

We hope that our journal provides accurate information for the international scientific community and serves the aim of the Hungarian agricultural and environmental engineering research.

Gödöllő, 20.12.2023.



**Dr. István SZABÓ**  
editor in chief



**Dr. László TÓTH**  
editor in chief





# **RAPID DETECTION OF SOIL TEXTURE ATTRIBUTE BASED ON MID- INFRARED SPECTRAL LIBRARY IN SALT AFFECTED SOILS OF HUNGARY**

## **Author(s):**

M. A. MohammedZein<sup>1,2,✉</sup>, E. Micheli<sup>1</sup>, B. Rotich<sup>1</sup>, P. N. Justine<sup>1</sup>, A. E. E. Ahmed<sup>3</sup>, H. Tharwat<sup>1</sup>, A. Csorba<sup>1</sup>

## **Affiliation:**

<sup>1</sup> Institute of Environmental Sciences – Hungarian University of Agriculture and Life Sciences, 2100 Gödöllő, Páter Károly u. 1., Hungary.

<sup>2</sup> Agricultural Research Corporation, Land and Water Research Centre, Wad Medani, Sudan

<sup>3</sup> Mechanical Engineering Doctoral School - Hungarian University of Agriculture and Life Sciences, 2100 Gödöllő, Páter Károly u. 1., Hungary.

## **Email address:**

mohammdzain@yahoo.com; micheli.erika@uni-mate.hu; brotich@chuka.ac.ke; pjustine@mustnet.ac.tz; wadelawad2004@gmail.com; hanaatharwat@hotmail.com; csorba.adam@uni-mate.hu

**Abstract:** Quantifying among others the soil's physical properties is essential for the assessment of the diverse soil environmental functions including water balance of soils and pore structure, water erosion and various soil hydraulic properties. The mid-infrared (MIR) spectroscopy is a useful technique to predict soil attributes with high accuracy, efficiency and low cost. In this study, we examined the ability of our MIR soil spectral library in predicting the clay, silt, sand content of salt affected Hungarian soils. This research is part of a project to establish a MIR spectral library in the frame of the Hungarian Soil Information and Mentoring System (SIMS) survey. Salt affected soils type data was extracted from the spectral library then transformation of spectral reflectance values to absorbance values were performed. Moving average filtering method was applied to absorbance spectra before performing principal components analysis. To determine outlier samples and to select the proper samples for model calibration, Mahalanobis distance-based outlier detection method and Kennard-Stone Sampling selection method were applied on the principal component scores. Spectral and reference soil data were combined and split into training and testing datasets. MIR prediction models were built for sand, clay, and silt content using Partial Least Square Regression (PLSR) method. Coefficient determination, root mean square error and ratio performance to deviation were used to assess the models performance. The prediction accuracies of calibration sets for soil physical texture were excellent while the validation results were slightly lower but still with a good level of prediction.

**Keywords:** Kennard-Stone sampling, partial least square, Soil Information Monitoring System, Diffuse Reflectance Infrared Fourier Transform

## **1. Introduction**

The soil surface layer's characteristics are important because they provide essential information for food production. Soil is a mixture of physical, chemical, mineralogical, and organic compounds, as well as water and air, and these properties have been degraded in many agricultural regions due to ineffective management [1]. Among the soil attributes, particle size distribution is an important soil property related to physical structure, and it is divided into three main fractions: clay (<0.002 mm), silt (0.002-0.02 mm), and sand (>0.02 mm). Soil physical attributes are required for different disciplines' study such as forest ecosystem, general agricultural production and long-term soil use [2]. One of the most essential soil physical features for determining infiltration rate, irrigation, and drainage practices is physical soil texture. It has a big impact on soil hydraulic characteristics including water permeability, soil water retention [3] and solute dispersion in the soil profile. Soil texture is therefore important for the environment, and land reclamation [4]. Soil texture also influences plant water uptake and the overall hydrological cycle [5], [6]. It has an impact on many

important soil attributes such as soil specific surface area and pore structure [7], [8]. On the other hand, convection attributable to upward water movement in reaction to evapotranspiration, diffusion due to a salinity gradient with depth, and limited drainage flow are the major causes of salt transfer to the soil surface [9]. Both soil water dynamics and salt accumulation phenomena are affected by physical soil texture. Furthermore, the relationship between some physical soil characteristics such as soil compaction, plasticity, consistency, mechanical resistance and air capacity are strongly correlated with soil particle size [10]. Additionally, soil mineral weathering rates, ion exchange and buffering capacity, and nitrogen and carbon sequestration are all affected by the relative content of particles within specific size ranges [11], [13]. Many soil processes, including pollutants and microbial activity, are governed by soil texture [14]. It has been used to aid in soil classification, management, and modeling of soil processes.

Knowing and analyzing the texture of the soil is vital to understanding how well it functions are related to plants and other soil processes. Various approaches can be used to identify the physical texture of soil. The two most important traditional assessment methods for soil texture are, hydrometer and the sieve-pipette, both are granulometric measurements of particle size using gravitational-sedimentation techniques. These methods are disadvantageous since they are extremely time-consuming and inaccurate e.g. under-estimate or overestimation of clay [15]. In addition,  $H_2O_2$ ,  $HCl$ ,  $C_6H_5Na_3O_7$  and  $NaHCO_3$  chemical compounds are necessary as pretreatment to remove soil organic matter, Fe oxides and carbonates from soil during measuring the soil physical texture. These compounds may generate toxic wastes that are environmentally harmful. Therefore, its application across large fields (e.g. soil survey activities and soil mapping) is impractical and expensive.

In contrast to the wet chemistry approaches, infrared spectroscopy has emerged as a feasible option for time and cost-effective solution for soil properties determination such soil texture. It is a low-cost and non-destructive method [16]. This approach is cheap, utilizes tiny subsamples and has the advantage that a single spectrum of soil sample integrates many attributes with highly precision [17], [18], do not require the use of chemical extracts that might harm the environment [19] and allows for the scanning of diverse soil types without samples dilution [20]. Fundamentally, soil infrared spectroscopy relies on the interplay of electromagnetic energy with matter to characterize samples' physical and biochemical composition. Fundamental molecular vibrations absorb electromagnetic radiation at specified wavelengths, resulting characteristic spectral fingerprints in mid-infrared (MIR) region (2.5 - 25  $\mu m$ ) which is sensitive to soils' organic and mineral components [14]. Several studies have shown that MIR across a wide range of soil types are more robust and provide accurate predictions of several soil properties such as clay and sand [21, 22, 23]. The reason for this is that the fundamental molecular vibrations of soil components that are absorbed at specific wavelengths of electromagnetic radiation occur in the absorbance MIR region. The MIR spectroscopy spectrum contains a high reflectivity, useful spectral features and gives greater information on soil attributes [24]. Various physical and chemical soil properties, including texture, have been detected using MIR spectroscopy [14], [25]. Nguyen [26] demonstrated Diffuse Reflectance Infrared Fourier Transform (DRIFT) MIR ability to distinguish diverse mineral components abundantly detected in Australian soils, such as kaolinite, quartz, carbonate, gibbsite, illite, and smectite minerals [27]. On the other hand, the soil science community has been recently working to create extensive soil mid-infrared spectral libraries on a national and global scale. Soil spectral libraries often contain significant amounts of soil samples that represent the diversity of soils in a given region. MIR spectral library has been shown to accurately estimate soil texture in addition to many soil attributes such as soil organic carbon, CEC, phosphorus and potassium content.

Due to the scatter effects caused by structure result in overlapping absorption features, diffuse reflectance spectra in soil are non-specific. To extract absorption patterns and correlate spectra with soil properties, multivariate techniques are required. Linear regression approaches for soil applications include stepwise multiple linear regression (SMLR), principal component regression (PCR), and partial least squares regression (PLSR). Thus, generation of prediction models based on the appropriate calibration dataset and robust algorithms is required for the accurate estimation of soil physical texture. In this regard, the PLSR is a powerful technique compared to other algorithms as it is easy to compute and interpret.

This study made use of data from the Hungarian MIR spectral library, which contained approximately 2200 MIR spectra collected on soils from Hungarian Soil Information and Mentoring System (SIMS). This massive database held data on soil samples analyzed using the same standard laboratory methods. As a result, we were able to determine which soil properties could be accurately predicted by MIR spectroscopy for assessing soil functions. The aims of this study therefore were to: a) build multivariate statistical models for

soil texture physical properties using PLSR and b) test the predictive capacity of MIR spectral library for sand, clay, and silt content in salt-affected soils types of Hungary.

## 2. Materials and Methods

### 2.1. Dataset

The soil samples spectral data utilized in this research were obtained from the MIR spectral library in Hungarian University of Agricultural and Life Sciences in Gödöllő which built based on the samples collected in frame of SIMS survey. The MIR spectral library database comprised measurements of about 2200 soil samples representing 10 Hungarian counties and five soil types. Salt affected soils type dataset was extracted from the MIR spectral library which contained about 100 soil samples.

### 2.2. Dataset preprocessing and outlier detection methods

Preprocessing methods for spectral dataset were used to enhance the accuracy of quantitative soil texture analysis. The Salt affected soils type spectra dataset were transformed from reflectance to absorbance value using the equation:

$$\text{Absorbance} = \log (1/\text{Reflectance}) \quad (1)$$

Absorbance spectra dataset were smoothed with a moving average window of 17 bands and Savitzky-Golay filtering methods to reduce and remove noise that represents random fluctuations in the signal. This noise may originate from the instrument or environmental laboratory conditions.

Principal Component Analysis (PCA) was applied to reduce the dimensionality of the spectral dataset, improve computational efficiency and to compress the spectral information into a few variables (Figure 1). Outlier detection was checked and calculated on PCs of spectral dataset using Mahalanobis distance method. The purpose of this methods was to identify samples that deviate from the average population of spectra[28]. Based on standard arbitrary threshold methods, the samples with a Mahalanobis dissimilarity larger than one were considered outliers.

### 2.3. Calibration sample selection and physical soil texture prediction models

In order to develop the best MIR spectral models for soil texture as well as to define how many observations (samples) should be listed as calibration dataset, Kennard-Stone sampling (KSS) selection method [29] was applied (Figure 2).

In terms of building soil texture models, salt affected soils processed dataset including reference soil data was split into training and testing datasets based on the KSS. Accordingly, 27 soil samples were selected for calibration dataset and the remaining samples were retained for the validation set ( $n = 63$ ). In this study, MIR prediction models were built for sand, clay and silt content using PLSR [30] using calibration dataset as well as the highest number of principal components and oscorespls method [31].

Coefficient of determination ( $R^2$ ), root mean square error (RMSE) and ratio performance to deviation (RPD) were used to assess the model's performance.

$$R^2 = \frac{\sum_{i=1}^n (\hat{y}_i - \bar{y}_i)^2}{\sum_{i=1}^n (Y_i - \bar{y}_i)^2} \quad (2)$$

$$RMSE = \sqrt{\frac{1}{n} \sum_{i=1}^n (\hat{y}_i - Y_i)^2} \quad (3)$$

$$RPD = s_y / RMSE \quad (4)$$

$\hat{y}$  indicates the spectral library's predicted value, while  $\bar{y}$  and  $\mathbf{y}$  represent the observed value average and observed value of reference soil database respectively  $\mathbf{n}$  represents the sample number where  $\mathbf{I}$  is equivalent to 1, 2, ..., while,  $s_y$  the observed values' standard deviation.

RStudio software [32] was used for spectral displaying, analysis and modelling processes using several packages, functions and operators. Models development were performed using the caret package interface [33] and PLSR function from pls package [34].

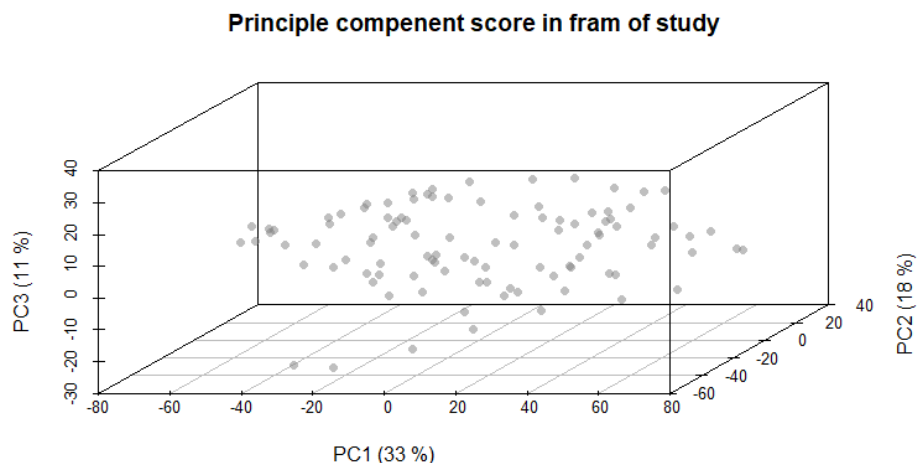


Figure 1. Principle component scores

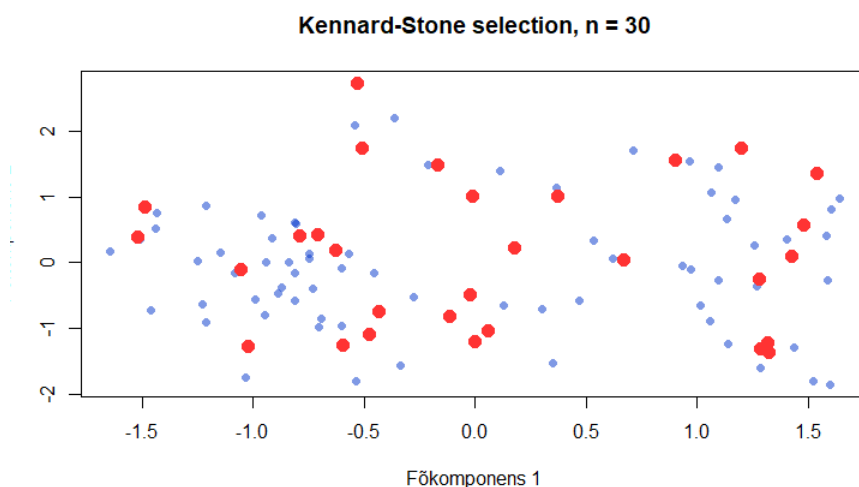


Figure 2. Kennard-stone sampling distributions

### 3. Results and Discussion

#### 3.1. Mid-Infrared spectral signature

Generally, the MIR absorbances were caused by fundamental molecular vibrations, which were characterized by clearly identified peaks related to either organic or mineral compounds. Soil samples MIR spectra of salt affected soil dataset extracted from spectral library are given in (Figure 3). The general shape and the position of the absorption features are determined by the physical-chemical composition of the soil samples. Since the clay, silt and sand content refers to particle size classes that involves a wide range of mineral particles, the direct visual attribution of spectral features to these soil properties are limited. However, careful visual interpretation of the spectral data revealed that the spectral features of clay minerals were clear while the ones for quartz were less identifiable. For example, due to OH stretching, clays or aluminosilicates display

strong peaks around 3700 1/cm. Furthermore, the band about 1630 1/cm is usually assumed to be caused by water in the clay. The complex band at roughly 1048 1/cm may be due to clay mineral spectra, which is connected to the stretching vibrations of Si-O groups, similar finding were obtained by [35]. The hydroxyl stretching vibrations of kaolinite, smectite, and illite are thought to be responsible for the absorption bands amongst 3800 and 3600 (1/cm). More specifically, the absorption peak at 3620 (1/cm) might be due to clay minerals, a similar result was obtained by [26]. A sharp band at 798 1/cm with a shoulder around 779 1/cm prove the existence of quartz mixes [36]. According to Nguyen [26], weak spectra signatures near 1100–1000  $\text{cm}^{-1}$  can also related to quartz. In addition, the clear band ranging between 2562 - 2480 1/cm may assigned to the vibration of molecules in quartz minerals.

**Spectra recorded in the frame of the study**

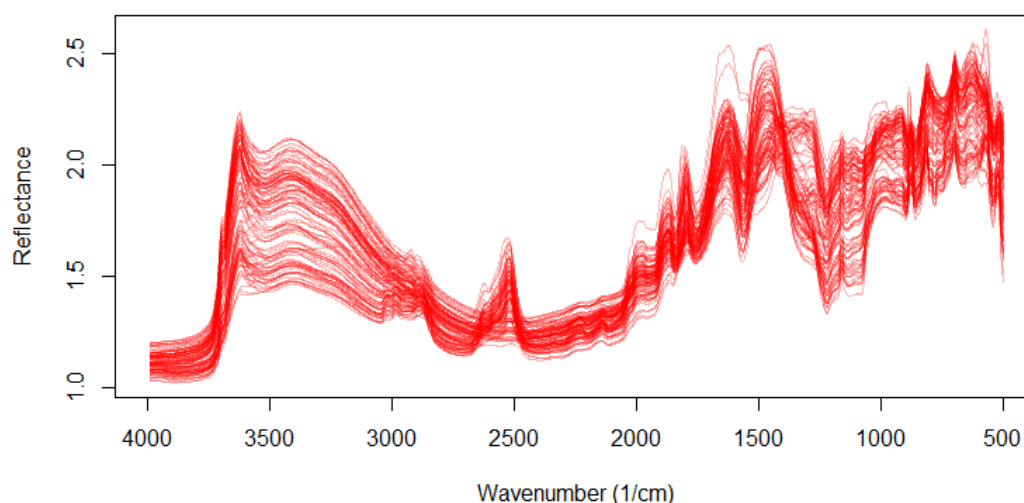


Figure 3. Mid-infrared spectra of salt affected soil dataset

### 3.2. Salt affected soil spectral dataset model performance

The pursuit of an efficient model for estimating soil texture is a common topic in soil science research [15]. Tables 1, 2 and 3 represent the test set validation and calibration of the spectral-based soil texture. Overall, components of physical soil texture were predicted excellent with the highest accuracy using the testing sets. Generally, the good performance models for sand, clay and silt content may be attributed to the high spectral activity of these materials in the MIR region.

#### 3.2.1. Sand

Amongst all soil texture in this study, especially, sand content showed the highest prediction accuracy at training and testing datasets (Table 1). The coefficient determination was 0.88, ratio performance to deviation was 2.92, while root mean square error was 8.42 at testing dataset (Table 1). The model parameters for the testing set represent the real performance of the models. The high coefficients determination of the sand content predictive models are attributed to fundamental vibrations of associated minerals in the MIR regions [14]. According to Mohanty [37], the majority of the absorption peaks that are directly or indirectly related to  $\text{SiO}_2$  fall in the MIR region. Thus, the MIR spectra predicted sand or  $\text{SiO}_2$  with greater accuracy.

Table 1. Results of the prediction models.

Sand %	Training Dataset				Testing Dataset			
	Mean	R <sup>2</sup>	RMSE	RPD	Mean	R <sup>2</sup>	RMSE	RPD
	26.59	0.96	4.3	5.33	29.05	0.88	8.42	2.92

### 3.2.2. Clay

The testing datasets show that clay prediction accuracy is good but not as high as the sand component (Table 2). Total clay content had  $R^2 = 0.80$ , RMSE = 7.11 and RPD = 2.23 (Table 2). The high  $R^2$  of clay content predictive models are attributed to specific strong absorption bands associated with chemical bonds [38] as well as fundamental vibrations of associated minerals in the MIR regions [14]. According to Urselmans [39], predicting clay content from MIR spectra was more direct because the absorption of the spectra was primarily concentrated in the mineral regions of the spectrum.

Table 2. Results of the prediction models.

Clay %	Training Dataset				Testing Dataset			
	Mean	R <sup>2</sup>	RMSE	RPD	Mean	R <sup>2</sup>	RMSE	RPD
	34.35	0.92	4.30	3.56	31.52	0.80	7.11	2.23

### 3.2.3. Silt

The prediction accuracy for total silt of the training dataset was high with the coefficient determination of 0.94 and ratio performance to deviation of 4.13 (Table 3). Whereas the root mean square error was 3.85. The prediction accuracy of testing set was good but slightly lower than the training set as well as sand content, but almost the same as clay content (Table 3). The total silt had ( $R^2 = 0.80$ , RMSE = 6.38, RPD = 2.27). The rather good silt prediction was surprising because it outperformed many previous findings, as reviewed by [14]. However, the achieved good results could be attributed to indirect effects on predicted silt. This assumption is supported by the strong negative correlation between conventionally measured silt and sand contents.

Table 3. Results of the prediction models.

Silt %	Training Dataset				Testing Dataset			
	Mean	R <sup>2</sup>	RMSE	RPD	Mean	R <sup>2</sup>	RMSE	RPD
	39.05	0.94	3.85	4.13	40.03	0.80	6.38	2.27

Generally, these results were similar to the findings by other researchers who achieved sand with  $R^2$  of 0.94, silt with  $R^2$  of 0.84 and clay with  $R^2$  of 0.79 [40]. Thomas [41], showed good results in MIR-based predictions for clay with  $R^2 = 0.88$  and sand with  $R^2 = 0.90$  for soils from a Kenyan farm validation set as well as Madari [25] who obtained  $R^2$  of 0.99, 0.8 and 0.96 for the estimation of sand, silt and clay, respectively. Hati [42], obtained  $R^2$  of 0.79 for the sand and clay predictions, while an  $R^2$  of 0.73 for the silt prediction from Eastern India soils which are lower prediction accuracy than our results. Similarly, Pirie [43] were unable to achieve high accuracy with predictions: clay ( $R^2 = 0.72$ ), followed by sand ( $R^2 = 0.62$ ) and silt ( $R^2 = 0.34$ ).

## 4. Conclusions

The goal of this study is to predict sand, clay and silt from a salt-affected soil types dataset consisting of 100 soil samples extracted from the Hungarian MIR spectral library, using PLSR statistical model. This study has demonstrated that MIR spectral libraries contain useful information related to soil texture and could be used as a cheap, fast and reliable alternative in the prediction of sand, clay and silt in salt-affected soil types in Hungary and elsewhere globally in soils with similar characteristics.

The PLSR model and technique outlined here can provide rapid predictions of physical soil texture in frame of these soil types.

## References

- [1] **S. Mantel, C. J. E. Schulp, and M. van den Berg**, “Modelling of soil degradation and its impact on ecosystem services globally,” *Report; ISRIC—World Soil Inf. Wageningen, Netherlands*, 2014.
- [2] **L. Duchesne and R. Ouimet**, “Digital mapping of soil texture in ecoforest polygons in Quebec, Canada,” *PeerJ*, vol. 9, p. e11685, Jun. 2021, doi: 10.7717/peerj.11685.
- [3] **J. H. M. Wösten, Y. A. Pachepsky, and W. J. Rawls**, “Pedotransfer functions: Bridging the gap between available basic soil data and missing soil hydraulic characteristics,” *J. Hydrol.*, vol. 251, no. 3–4, pp. 123–150, Oct. 2001, doi: 10.1016/S0022-1694(01)00464-4.
- [4] **X. Li, S. X. Chang, and K. F. Salifu**, “Soil texture and layering effects on water and salt dynamics in the presence of a water table: a review,” *Environ. Rev.*, vol. 22, no. 1, pp. 41–50, Mar. 2014, doi: 10.1139/er-2013-0035.
- [5] **K. R. Hultine, D. F. Koepke, W. T. Pockman, A. Fravolini, J. S. Sperry, and D. G. Williams**, “Influence of soil texture on hydraulic properties and water relations of a dominant warm-desert phreatophyte,” *Tree Physiol.*, vol. 26, no. 3, pp. 313–323, Mar. 2006, doi: 10.1093/treephys/26.3.313.
- [6] **K. E. Saxton and W. J. Rawls**, “Soil Water Characteristic Estimates by Texture and Organic Matter for Hydrologic Solutions,” *Soil Sci. Soc. Am. J.*, vol. 70, no. 5, pp. 1569–1578, Sep. 2006, doi: 10.2136/sssaj2005.0117.
- [7] **J. C. Fiès and A. Bruand**, “Particle packing and organization of the textural porosity in clay-silt-sand mixtures,” *Eur. J. Soil Sci.*, vol. 49, no. 4, pp. 557–567, Dec. 1998, doi: 10.1046/j.1365-2389.1998.4940557.x.
- [8] **J. C. Santamarina, K. A. Klein, Y. H. Wang, and E. Prencke**, “Specific surface: Determination and relevance,” *Can. Geotech. J.*, vol. 39, no. 1, pp. 233–241, Feb. 2002, doi: 10.1139/t01-077.
- [9] **S. Kessler, L. Barbour, K. C. J. Van Rees, and B. S. Dobchuk**, “Salinization of soil over saline-sodic overburden from the oil sands in Alberta,” *Can. J. Soil Sci.*, vol. 90, no. 4, pp. 637–647, Dec. 2010, doi: 10.4141/CJSS10019.
- [10] **C. T. Fongaro et al.**, “Improvement of clay and sand quantification based on a novel approach with a focus on multispectral satellite images,” *Remote Sens.*, vol. 10, no. 10, p. 1555, Sep. 2018, doi: 10.3390/rs10101555.
- [11] **R. K. Kolka, D. F. Grigal, and E. A. Nater**, “Forest soil mineral weathering rates: Use of multiple approaches,” *Geoderma*, vol. 73, no. 1–2, pp. 1–21, Sep. 1996, doi: 10.1016/0016-7061(96)00037-7.
- [12] **E. de C. C. Telles et al.**, “Influence of soil texture on carbon dynamics and storage potential in tropical forest soils of Amazonia,” *Global Biogeochem. Cycles*, vol. 17, no. 2, p. n/a-n/a, Jun. 2003, doi: 10.1029/2002gb001953.
- [13] **L. Wiklander**, “The role of neutral salts in the ion exchange between acid precipitation and soil,” *Geoderma*, vol. 14, no. 2, pp. 93–105, 1975, doi: 10.1016/0016-7061(75)90068-3.
- [14] **J. M. Soriano-Disla, L. J. Janik, R. A. Viscarra Rossel, L. M. MacDonald, and M. J. McLaughlin**, “The performance of visible, near-, and mid-infrared reflectance spectroscopy for prediction of soil physical, chemical, and biological properties,” *Appl. Spectrosc. Rev.*, vol. 49, no. 2, pp. 139–186, Feb. 2014, doi: 10.1080/05704928.2013.811081.
- [15] **C. L. Thomas, J. Hernandez-Allica, S. J. Dunham, S. P. McGrath, and S. M. Haefele**, “A comparison of soil texture measurements using mid-infrared spectroscopy (MIRS) and laser diffraction analysis (LDA) in diverse soils,” *Sci. Rep.*, vol. 11, no. 1, p. 16, Dec. 2021, doi: 10.1038/s41598-020-79618-y.
- [16] **W. Ng, B. Minasny, S. H. Jeon, and A. McBratney**, “Mid-infrared spectroscopy for accurate measurement of an extensive set of soil properties for assessing soil functions,” *Soil Secur.*, vol. 6, p. 100043, Mar. 2022, doi: 10.1016/j.soisec.2022.100043.
- [17] **L. Raphael**, “Application of FTIR Spectroscopy to Agricultural Soils Analysis,” *Fourier Transform. - New Anal. Approaches FTIR Strateg.*, 2011, doi: 10.5772/15732.
- [18] **B. K. Waruru, K. D. Shepherd, G. M. Ndegwa, A. Sila, and P. T. Kamoni**, “Application of mid-infrared spectroscopy for rapid characterization of key soil properties for engineering land use,” *Soils Found.*, vol. 55, no. 5, pp. 1181–1195, Oct. 2015, doi: 10.1016/j.sandf.2015.09.018.
- [19] **R. A. Viscarra Rossel, R. N. McGlynn, and A. B. McBratney**, “Determining the composition of

- mineral-organic mixes using UV-vis-NIR diffuse reflectance spectroscopy,” *Geoderma*, vol. 137, no. 1–2, pp. 70–82, Dec. 2006, doi: 10.1016/j.geoderma.2006.07.004.
- [20] **G. Siebielec, G. W. McCarty, T. I. Stuczynski, and J. B. Reeves**, “Near- and Mid-Infrared Diffuse Reflectance Spectroscopy for Measuring Soil Metal Content,” *J. Environ. Qual.*, vol. 33, no. 6, pp. 2056–2069, Nov. 2004, doi: 10.2134/jeq2004.2056.
- [21] **W. Ng et al.**, “Convolutional neural network for simultaneous prediction of several soil properties using visible/near-infrared, mid-infrared, and their combined spectra,” *Geoderma*, vol. 352, pp. 251–267, Oct. 2019, doi: 10.1016/j.geoderma.2019.06.016.
- [22] **J. B. Reeves**, “Near- versus mid-infrared diffuse reflectance spectroscopy for soil analysis emphasizing carbon and laboratory versus on-site analysis: Where are we and what needs to be done?,” *Geoderma*, vol. 158, no. 1–2, pp. 3–14, Aug. 2010, doi: 10.1016/j.geoderma.2009.04.005.
- [23] **R. A. Viscarra Rossel, D. J. J. Walvoort, A. B. McBratney, L. J. Janik, and J. O. Skjemstad**, “Visible, near infrared, mid infrared or combined diffuse reflectance spectroscopy for simultaneous assessment of various soil properties,” *Geoderma*, vol. 131, no. 1–2, pp. 59–75, Mar. 2006, doi: 10.1016/j.geoderma.2005.03.007.
- [24] **K. D. Shepherd and M. G. Walsh**, “Infrared Spectroscopy—Enabling an Evidence-Based Diagnostic Surveillance Approach to Agricultural and Environmental Management in Developing Countries,” *J. Near Infrared Spectrosc.*, vol. 15, no. 1, pp. 1–19, Feb. 2007, doi: 10.1255/jnirs.716.
- [25] **B. E. Madari, J. B. Reeves, P. L. O. A. Machado, C. M. Guimarães, E. Torres, and G. W. McCarty**, “Mid- and near-infrared spectroscopic assessment of soil compositional parameters and structural indices in two Ferralsols,” *Geoderma*, vol. 136, no. 1–2, pp. 245–259, Dec. 2006, doi: 10.1016/j.geoderma.2006.03.026.
- [26] **T. T. Nguyen, L. J. Janik, and M. Raupach**, “Diffuse reflectance infrared fourier transform (Drift) spectroscopy in soil studies,” *Aust. J. Soil Res.*, vol. 29, no. 1, pp. 49–67, 1991, doi: 10.1071/SR9910049.
- [27] **L. J. Janik, R. H. Merry, S. T. Forrester, D. M. Lanyon, and A. Rawson**, “Rapid Prediction of Soil Water Retention using Mid Infrared Spectroscopy,” *Soil Sci. Soc. Am. J.*, vol. 71, no. 2, pp. 507–514, Mar. 2007, doi: 10.2136/sssaj2005.0391.
- [28] **B. K. Waruru, K. D. Shepherd, G. M. Ndegwa, P. T. Kamoni, and A. M. Sila**, “Rapid estimation of soil engineering properties using diffuse reflectance near infrared spectroscopy,” *Biosyst. Eng.*, vol. 121, pp. 177–185, May 2014, doi: 10.1016/j.biosystemseng.2014.03.003.
- [29] **R. W. Kennard and L. A. Stone**, “Computer Aided Design of Experiments,” *Technometrics*, vol. 11, no. 1, pp. 137–148, Feb. 1969, doi: 10.1080/00401706.1969.10490666.
- [30] **A. Lorber, L. E. Wangen, and B. R. Kowalski**, “A theoretical foundation for the PLS algorithm,” *J. Chemom.*, vol. 1, no. 1, pp. 19–31, Jan. 1987, doi: 10.1002/cem.1180010105.
- [31] **A. Wadoux, B. Malone, B. Minasny, M. Fajardo, and A. Mcbratney**, *Soil Spectral Inference With R*, vol. 49, no. 0. Cham: Springer International Publishing, 2020.
- [32] **R Core Team**, “R: A language and environment for statistical computing. R Foundation for Statistical Computing, Vienna, Austria,” 2022.
- [33] **K. Max et al.**, “Classification and Regression Training,” *Packag. R CRAN*, p. 198, 2016, [Online]. Available: <https://github.com/topepo/caret/%5CnBugReports>.
- [34] **B.-H. Mevik, R. Wehrens, and K. H. Liland**, “Partial Least Squares and Principal Component Regression,” *Packag. R CRAN*, pp. 1–59, 2016, [Online]. Available: <https://cran.r-project.org/web/packages/pls/pls.pdf>.
- [35] **A. Tinti, V. Tugnoli, S. Bonora, and O. Francioso**, “Recent applications of vibrational mid-Infrared (IR) spectroscopy for studying soil components: a review,” *J. Cent. Eur. Agric.*, vol. 16, no. 1, pp. 1–22, 2015, doi: 10.5513/JCEA01/16.1.1535.
- [36] **J. Madejová**, “FTIR techniques in clay mineral studies,” *Vib. Spectrosc.*, vol. 31, no. 1, pp. 1–10, Jan. 2003, doi: 10.1016/S0924-2031(02)00065-6.
- [37] **B. Mohanty, A. Gupta, and B. S. Das**, “Estimation of weathering indices using spectral reflectance over visible to mid-infrared region,” *Geoderma*, vol. 266, pp. 111–119, Mar. 2016, doi: 10.1016/j.geoderma.2015.11.030.
- [38] **R. A. V. Rossel and T. Behrens**, “Using data mining to model and interpret soil diffuse reflectance spectra,” *Geoderma*, vol. 158, no. 1–2, pp. 46–54, Aug. 2010, doi: 10.1016/j.geoderma.2009.12.025.
- [39] **T. Terhoeven-Urselmans, T.-G. Vagen, O. Spaargaren, and K. D. Shepherd**, “Prediction of Soil

- Fertility Properties from a Globally Distributed Soil Mid-Infrared Spectral Library,” *Soil Sci. Soc. Am. J.*, vol. 74, no. 5, pp. 1792–1799, Sep. 2010, doi: 10.2136/sssaj2009.0218.
- [40] **L. J. Janik, R. H. Merry, and J. O. Skjemstad**, “Can mid infrared diffuse reflectance analysis replace soil extractions?,” *Aust. J. Exp. Agric.*, vol. 38, no. 7, pp. 681–696, 1998, doi: 10.1071/EA97144.
- [41] **C. L. Thomas, J. Hernandez-Allica, S. J. Dunham, S. P. McGrath, and S. M. Haefele**, “A comparison of soil texture measurements using mid-infrared spectroscopy (MIRS) and laser diffraction analysis (LDA) in diverse soils,” *Sci. Rep.*, vol. 11, no. 1, 2021, doi: 10.1038/s41598-020-79618-y.
- [42] **K. M. Hati et al.**, “Mid-Infrared Reflectance Spectroscopy for Estimation of Soil Properties of Alfisols from Eastern India,” *Sustain.*, vol. 14, no. 9, p. 4883, Apr. 2022, doi: 10.3390/su14094883.
- [43] **A. Pirie, B. Singh, and K. Islam**, “Ultra-violet, visible, near-infrared, and mid-infrared diffuse reflectance spectroscopic techniques to predict several soil properties,” *Aust. J. Soil Res.*, vol. 43, no. 6, pp. 713–721, 2005, doi: 10.1071/SR04182.

## PRODUCTION AND PRODUCTION-INCREASING FACTORS OF BIOCHAR

### Author(s):

V. Madár<sup>1</sup>, A. Betovics<sup>2</sup>, L. Tóth<sup>2</sup>

### Affiliation:

<sup>1</sup> Pyrowatt Kft., 6120 Kiskunmajsa, Vágóhíd utca 91., Hungary;

<sup>2</sup> Institute of Technology - Hungarian University of Agriculture and Life Sciences, 2100 Gödöllő, Páter Károly u. 1., Hungary.

### Email address:

Madar.Viktor@pyrowatt.hu; Betovics.Andras.Mate@phd.uni-mate.hu; Toth.Laszlo.emeritus@uni-mate.hu

**Abstract:** In the article, we deal with biochar-related research and our own developments. Studies in the literature show that biochar can be used as a soil conditioner in agriculture and horticulture. It improves many physical, chemical, and biological properties of the soil and substrate. It increases the water retention capacity while reducing the leaching of nutrients. Through these, you can improve the profit of producers, the sustainability of production, and the efficiency of fertiliser use. By increasing water retention, biochar can reduce irrigation needs and enable production on limited water resources. The developed and presented equipment was called the resting bed (fixed bed) version. Drying and carbonization are also carried out by direct heat transfer. The material, with a temperature equalised by moving drying and a homogeneous composition, enters the reactor. The high-temperature gas and air mixture is introduced into the dryer by a gas jet pump. The energy obtained by burning the pyrolysis gases produced during carbonization ensures the heating of the system, so there is no need for significant external energy input. Due to the structure of the system, the PAH content of the final product is low.

**Keywords:** biochar, effect of biochar on soils, production of biochar

### 1. Introduction

Nowadays, the price increases in the secondary materials traditionally used for agricultural production – energy, insecticide, fertilizer – have become an everyday occurrence.

For the population on planet Earth is on the rise, which means that a growing population requires a growing food supply. The necessary area to produce foodstuffs is reducing in concert with the climate change. Another factor influencing the process is the incorrect land usage, which is the cause of, among other issues, desertification. Parallel to these issues, an increase in water demand from both plant production and other organic lifeforms is also apparent. Today, these are the most notable, and most critical issues for humanity to solve.

As a possible solution to produce foodstuffs, producing a larger amount of food on the same unit of area is an option. However, this may only be implemented if the richness of the soil and the other circumstances and conditions of production make it possible.

There are many various instances of research dealing with the improvement of soil that degraded due to incorrect use, but the areas so far determined to be unsuited to agricultural production being improved to a point where they can host agriculture is also an often-explored option. Most of the researchers consider the renewable energy sources found in nature to be the source of technologies and techniques supporting these goals. Such sources are the various forms of bio-waste used for energy production, and producing materials which conserve the productivity of soil, or even improve it.

In this paper, we explore one of these options, related to the production and application of using biochar.

## 2. Materials and Methods

### 2.1. What is biochar?

Biochar is a material reminiscent of coal (Fig. 1), which is produced out of plant materials like wood waste, secondary products made from herbaceous plants, and remains of agri- and silviculture. These materials are decomposed using heat, which also generates renewable energy (depending on the process).

During the process, the physical and chemical nature of the plant materials are changed into a porous and from a biological perspective, structurally stable (hard to decompose) material rich in carbon.

Research done with this material shows that it can be used as a soil improvement material in agriculture and gardening (which means it influences several physical, chemical and biological attributes of the soil).

However, its beneficial effects rely on the method of the coal's production, whether the source materials used are applicable or not, and the system of usage (production) the end product will be implemented in.



Figure 1. Wood waste (A), processed into biochar (B) and biochar processed from short-blade grass (C).

Biochar (also called biocoal, or syn-coal, for synthetic coal) improves the nutrient accessibility of plants and improves the water-sealing capacity as well. It also prevents nutrients from getting washed out of the soil. Due to the improvement in water-sealing, biochar can reduce watering needs, and makes the expansion of production possible even in the case of limited access to water sources.

The abovementioned advantages together can modify the microbe culture in the rooting zone of plant life, which leads to a higher richness of microbes and activity of them. This increases the yield. A high number of studies show that biochar was successful in improving the growth of plant life (Tab. 1), though others reported that there's no observable effect in specific types of soil.

Table 1. Biochar attributes by base material [1]

What do we produce biochar from?	Soil and soil substance used for	Effect on plant growth	Analysis using
Hardwood	In soil (as is)	Increase	Corn
Hardwood pellet and straw pellet	Mixed with muskeg	Small- or no increase	Tomato
Hardwood mixture	Hardwood and pine bark	Increase	Flowers

### 2.2. Production of biochar

Fig. 2 shows the *generic pyrolysis process (thermic decomposition)* of biomass materials. If the process requires a temperature higher than the one noted on the figure, it is required for a different specified process, for example, production of power-gas.

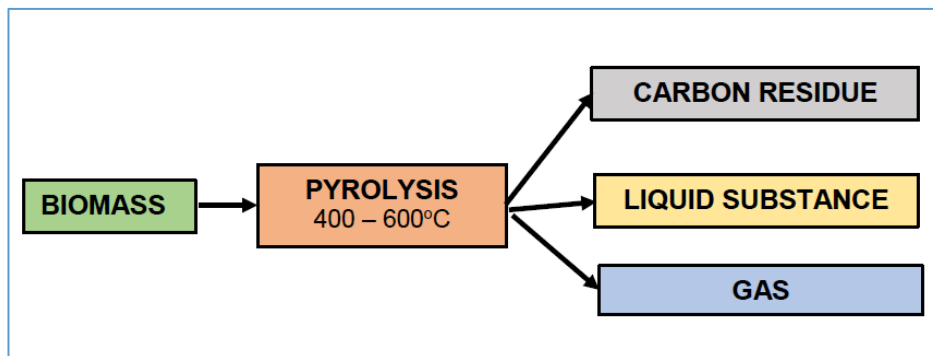


Figure 2. Generic thermic decomposition (pyrolysis in general)

The varied use of thermic decomposition is illustrated on Fig. 3, where the process separates into two parts. One is the creation of coal called torrefaction, which basically includes heat tempering of biomass only, meaning we're processing a heat-tempered (coal-like) biomass. Real biochar is more stable than this, which means it won't decompose even in the case of being left in soil for longer periods of time. The other branch of the process includes energy-production goals as well. If the goal is only the production of power-gas, only a small quantity of by-products in the form of ashes remain, amounting to a few percent. However, in this process, the quantity of coal can be increased, while improving its quality simultaneously.

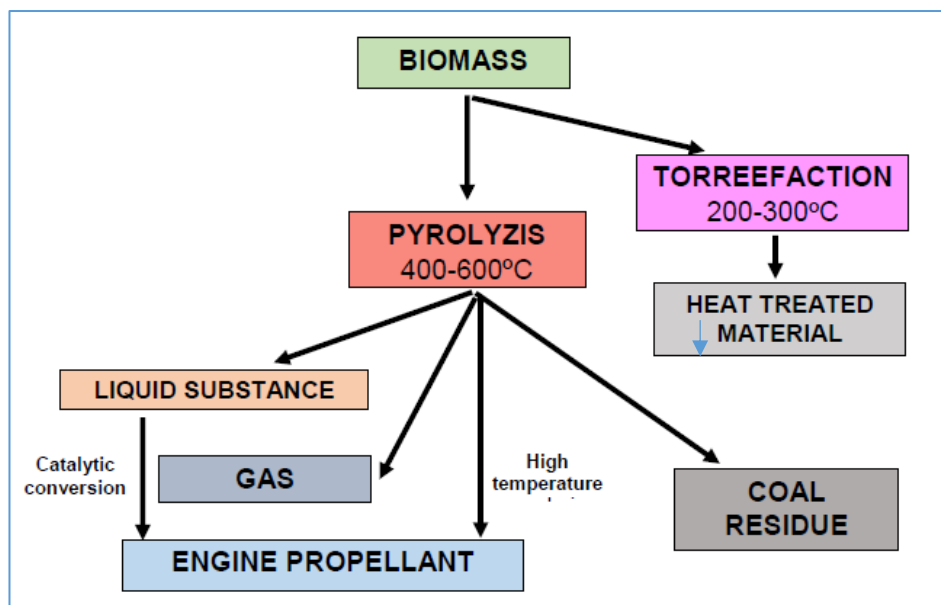


Figure 3. Thermic process producing biomass materials for several uses

Pyrolysis is a thermochemical process which consists of the decomposition of organic polymers and some biomass minerals, mainly restricted to lingo-cellulose sources. The decomposition results are produced somewhere between 400 and 800 degrees centigrade without oxygen (Fig. 4). The product is usually generator gas, or liquid-phase bio-oil. The so-called "slow pyrolysis" (300 to 400 degrees centigrade) is mainly used to produce coal with long reaction times (this is usually conducted on 500 to 650 degrees centigrade when accelerated). In order to produce a gaseous product usable as fuel, a temperature higher than 7-800 degrees centigrade is required.

A wide variety of technological systems were designed for these processes, with the fundamental goal of improving the end materials, and the performance of the process. This means that the goal is to get the highest possible usable energy resources from a single unit of energy content input (biomass). In other words, reducing the difference between source material and end energy output as much as possible, while simultaneously keeping the negative environmental effects of the production process to a minimum.

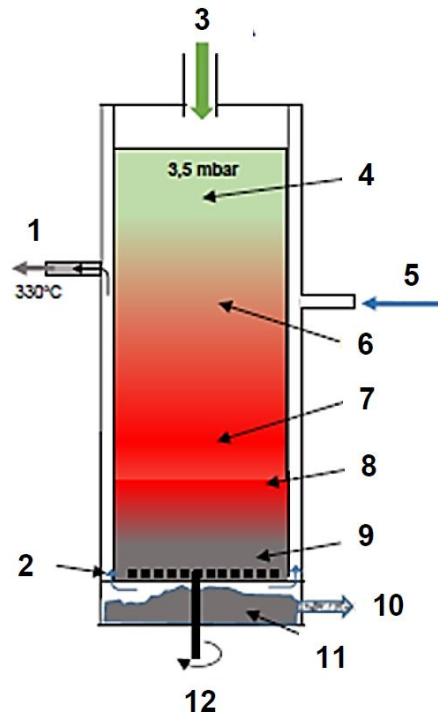


Figure 4. Technological process of thermic decomposition (resting bed system)

- |                                       |                       |
|---------------------------------------|-----------------------|
| - gas air mixture,                    | - start of combustion |
| - gas between the walls of the mantle | - burn                |
| - biomass                             | - start of cooling    |
| - dryness, humidity                   | - cooling coal        |
| - air intake                          | - biochar removal     |
| - start of combustion                 | - biochar             |
|                                       | - scraper unit        |

### 2.2.1. Effects of biochar production conditions on attributes

The zones, ie. the various temperature areas have no distinct differences, the oxidation agent may be air, steam, etc. In the end, the heating temperature of the input material, and the time being subject to heating are important [2]. In other words, the temperature transmission process may be fast or slow, depending on the heating velocity and duration of exposition. If the heating process is fast, and the plant material reaches a high temperature (roughly above 660 degrees centigrade) in a short timeframe, the biochar product will generally contain very fine grains. Similarly, lower temperatures (between 450 and 550 degrees centigrade) and slower heating velocity will create biochar with larger grains.

When creating biochar in practice, the goal is to achieve the optimal temperature (Fig. 5), meaning the temperature to heat to needs to be chosen to reach the highest possible specific grain area size in the remaining coal. At the same time, the carbon content compared to the base material should be acceptable (meaning its carbon-sealing is good), and its capacity for exchanging cations (CEC) should also be good. The cation exchange capacity of coal is very important, because negative polarity cations sticking to the grains are replaced by other cations (for example, potassium is changed by hydrogen, or vice-versa). Finally, the capacity for exchanging cations is fundamentally the quantity the soil is capable of sealing off. During production, one must aim to reach the highest possible number for this attribute. We can see the optimum temperature of the heat zones on Fig. 5, when the median of the temperature is somewhere around 500 degrees centigrade. At this point, the inner surface area is the highest, the pH value is the most advantageous, and the CEC value is average as well. We can obtain roughly 65% of the initial coal amount in biochar. In a short cycle, the material also goes through a higher temperature zone than this, which is advantageous for the degradation of PAH materials. The material may not be in higher temperatures for long, because the quantity of biochar we can produce decreases significantly, but the surface area is also reduced at the same time.

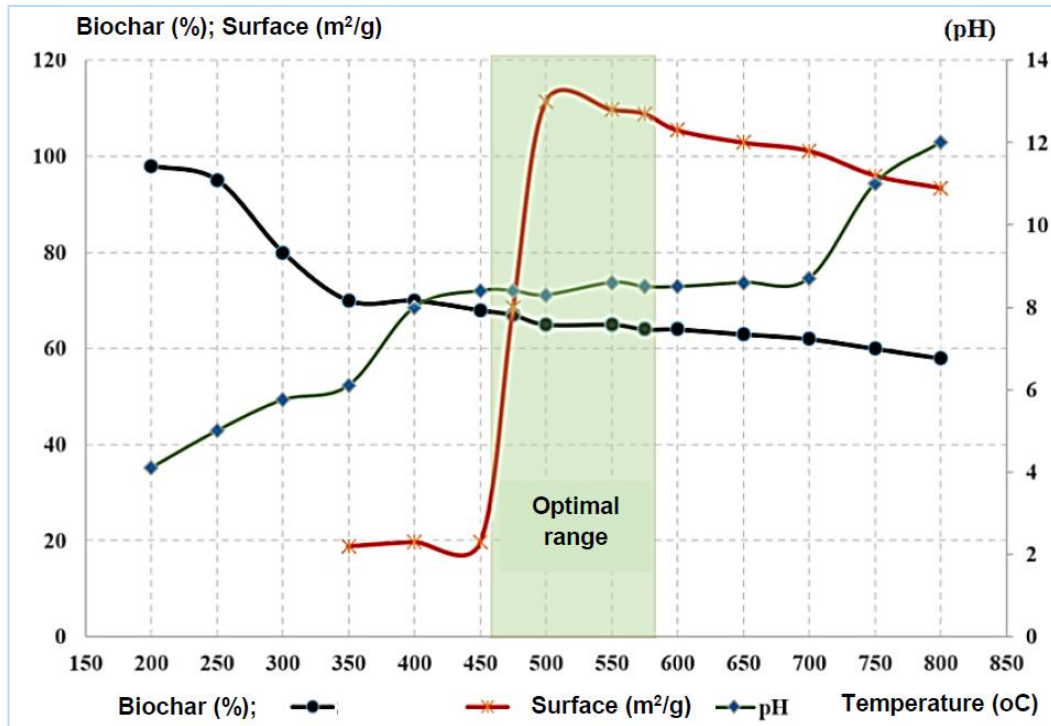


Figure 5. Changes in biochar attributes based on temperature.

In the case of a faster heating with higher temperature, a more porous, higher inner surface area biochar will be produced, with a higher pH value. Therefore, the production attributes have to be closely followed, such as: types of biomass, temperatures of decomposition, times of lingering in parts of the system, heating velocity values, pressure of the production area, etc. [3, 4, 5].

In summary, the advantages of biochar shine when:

- surface area is big,
- porosity is substantial,
- has a high CEC value,
- highly stable in different applications, etc.

Other attributes in more detail can be seen on Fig. 6.

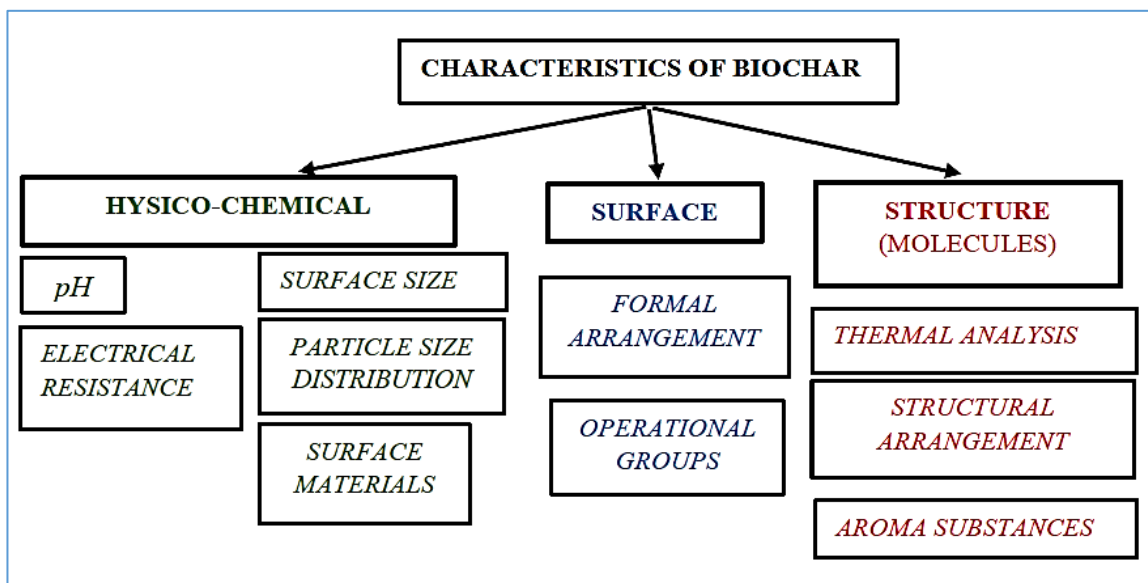


Figure 6. Physical-chemical surface area and structural attributes of biochar. [6]

## 2.3. Usage of biochar

### 2.3.1. Effects on agriculture

Degraded, dry soils and bad production capacity, low organic nutrient-content soils can improve in quality, and be more useful with the modifications accessible through biochar. In several documented cases, biochar improved nutrient- and water-sealing capacity, improved production capacity, and the efficiency of yield management. Further advantages are offered by the biochar's nature of absorbing the inorganic and organic impurities found in the water washing out the soil.

Biochar is capable of holding distributed fertiliser and other nutrients, which can be used later on. For clarity's sake, we must differentiate between biochar and compost. Biochar is different compared to the compost generally added to the soil for traditional agricultural production in that compost is a direct source of nutrients, decomposing with other nutrients when used. Biochar, however, doesn't decompose even after a longer timeframe, thereby making new additions to the soil unnecessary. Spokas and colleagues concluded that biochar may lead to positive effects in agricultural production, after reviewing the literature on biochar [7]. Laird conducted research using biochar on strongly fragmented and infertile soil, where advantages of its use were documented plentifully, for example, in the low fertility, sandy soil of Florida [8].

On rich, fertile soil, using biochar is only advised in smaller amounts. Carbon has a very important role in the various chemical and biological reactions during its cycle. The carbon source of plants is both the soil and the atmosphere, from where they absorb carbon in the form of  $\text{CO}_2$  (Fig. 7).

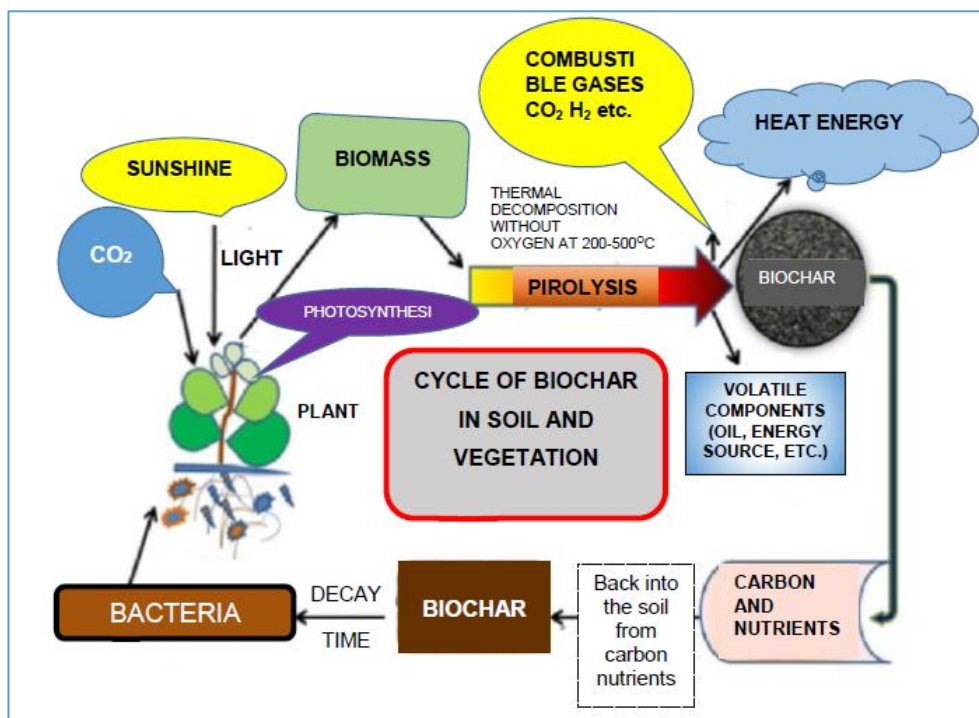


Figure 7. Carbon cycle in nature

Advantageous effects on the environment can be measured during the process:

- In the biochar manufactured from a kilogram of biomass, roughly 300g  $\text{CO}_2$  is sealed, and remains in the soil for a long-term.
- Therefore, unlike the natural degradation of biomasses, instead of 900 g  $\text{CO}_2$ , only 600g  $\text{CO}_2$  returns into the atmosphere – in other words, the difference is 'subtracted' from the GHG effect, while,
- ~1,0 kWh energy is obtained.

Fine grain biochar is a strongly porous material, with the most notable attribute of having a large surface area (200-300m<sup>2</sup>/g), which is basically created during the 500°C-os heat tempering [9]. Compared to other soil improvement agents, its large specific area and porosity makes it possible to absorb water and conserve nutrients within itself, while it also offers a habitat for useful micro-organisms [10]. They also concluded that the reproduction rate of microbes showed an increase within soil treated using biochar [11].

Porosity has an influence on the processes that happen in the root zone, including the breathing of plants, and the absorption of root water. Biochar also modifies the soil, improving its porosity and structure. Sandy soil and clay soil improved significantly in SBD, porosity, and water content. Porous structure (Fig. 8) aids with conserving water in the soil, but in truth, doesn't increase water content to utilise.

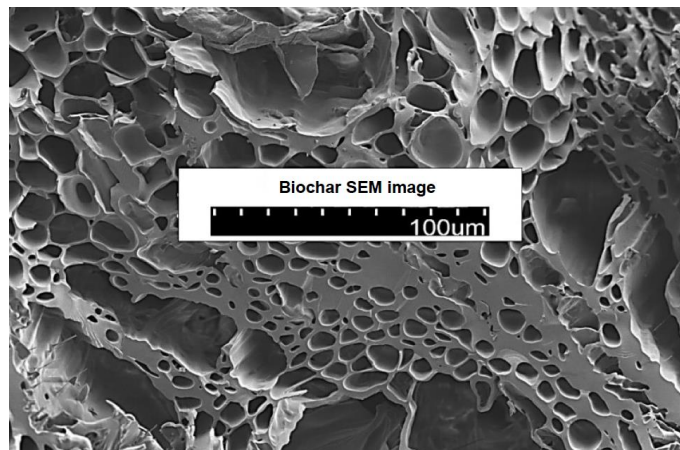


Figure 8. Porosity of biochar made out of rice straw, (SEM image after heat tempering on 500°C)

Raw organic materials serve as nutrients in the soil, for plants and the micro-organisms found inside the same soil, while biochar acts as a catalysing agent, improving the absorption of nutrients done by plant life [12]. Commercially available biochar-based soil improvement agents can increase the specific surface area of soil by changing the pore sizes and density of the original soil [13].

The chemical and physical attributes of biochar are improved if the material interacts with steam and carbon-dioxide during the manufacturing process. The carbon content of biomass can only be changed into aromatic carbon groups, amorphous- and graphite structures like this. During the pyrolysis, organic mixtures within the biomass may be diluted into the mass, and may unify dioxides, furans, but mostly polycyclic aromatic carbon hydrogens. The resulting PAH-s are contaminating the soil due to their lipophilic structures, meaning the biochar with such content has no advantages, or is disadvantageous [14]. The most important quality markers of biochar are high absorption and CEC values, and low mobile material content (sludge, resin, and similar short life cycle mixtures) [10].

Production temperature is also a definitive factor. Wood-based biochars produced above 450 degrees centigrade are more prone to result in higher stability and porosity, and absorption capacity products, compared to those manufactured on lower temperatures [15]. On lower temperature spectrums (300–350°C) carbonization only concludes partially, which results in smaller pores, and smaller surface area [16].

Often advertised plant conditioning products primarily affect plant life cycles through influencing the nutrient cycles. Biochar can also be placed in this group, and often a part of these wares, but is also sold as a separate ware (Fig. 9)



Figure 9: Domestic<sup>1</sup> and USA-sold<sup>2</sup> material Source: <sup>1</sup> Agrofutura Hungary Co. Ltd.,  
<sup>2</sup> <https://www.biogreen-energy.com/biochar-production>.

### 3. Results and Discussion

#### 3.1. Domestic-developed carbonizer and measurement results

Based on literature sources and our own measurements, the design of the carbonizer were created. The goals of the manufacturer and the designer were to create simple, but automated, easily applicable machine for smaller enterprises and industrial units. From a mechanical-technological perspective, we wanted to design a system that produces excellent quality products at a lower PAH (pollutant) content compared to other domestic products, which gets closer to the standard (EU requirements).

Finally, the detailed designs and manufacturing were done by Pyrowatt Co. Ltd. (Fig. 10).

Main attributes of the machine are detailed below.

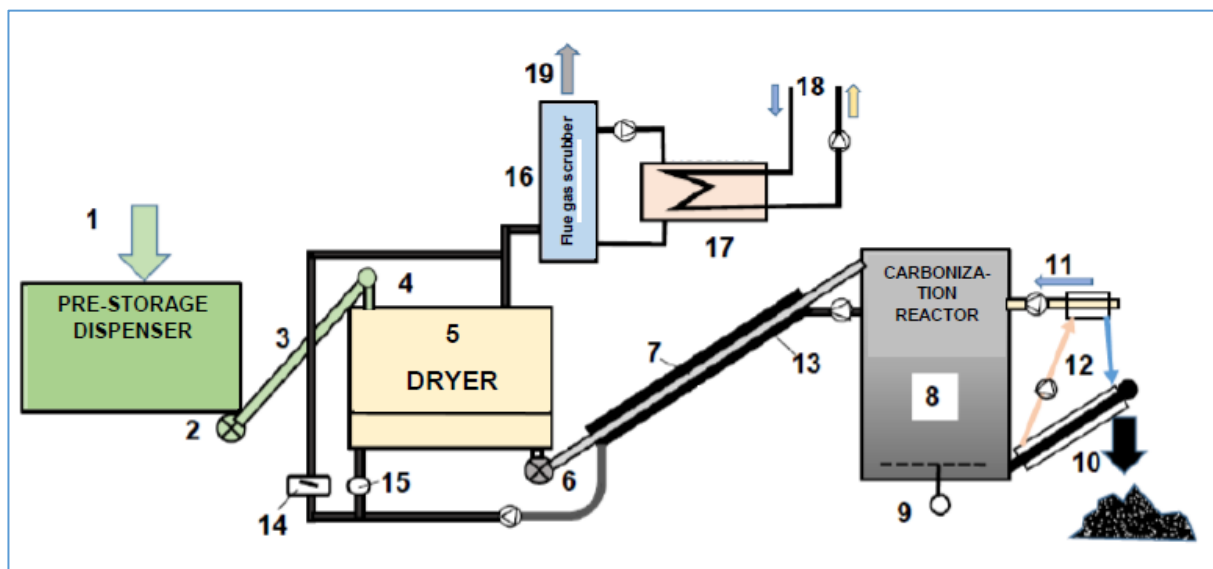


Figure 10. The process of the system

where:

- |  |   |
|--|---|
| 1. Biomass into the precontainer-feeder intake           | 11. air intake  |
| 2. cell feeder   | 12. preheating of air (through the mantle of the biochar excavator and air intake pipe) |
| 3. conveyor transport                                    | 13. heating mantle pipe   |
| 4. material intake into the dryer                        | 14. regulator (with applicable heat exchanger)  |
| 5. double dryer (fan mixer and screw excavator unit)     | 15. air-gas mixture intake into the dryer   |
| 6. cell feeder   | 16. intake of the gas flowing out from the dryer, into the washing unit                 |
| 7. conveyor transport                                    | 17. heat exchanger (heat absorption recuperator)  |
| 8. reactor   | 18. regain of recuperated heat, intake of external airflow                              |
| 9. mixer- and excavator structure (with electric engine) | 19. cleaned smoke gas   |
| 10. biochar excavator screw (and the processed material) |   |

The open fuel container has a filter on top, in order to separate the very big grains (material remains). Carrying out the completed fuel is done by the rotating excavator at the bottom part of the containment unit (electric, 0,75 kW). The size class of the required fuel is G30 - G50, M7133 in the Önorm classification.

- Containment unit width: 1,5m
- Containment unit length: 1,0 m
- Maximum size of fuel: 1,0 m
- Nominal capacity: 1,5 m<sup>3</sup>
- Highest mass flow of the excavator: 400 kg/h

Operating the carbonizer requires fuel with ~18% moisture content, if it's any higher, the fuel needs to be dried [17, 18]. The drying of the fuel was done using screw churning. Fuel input is done through a feeder

going from the precontainment unit to the dryer. Energy necessary for drying is obtained from the 300-400 °C gas coming out of the carbonizer. The gas is transported with a radial ventilator. The dryer has a steel structure, and is completely enclosed, its surface insulated. The maximum temperature of the part is 65 °C. The performance of drying can be modified with the gas used to dry, the temperature of the steam, and its capacity flow. At the end of the drying section, an excavator screw is placed, which transports the dry fuel into the carbonizer.

Main data:

- Necessary heat performance: 200 kW (for biggest mass flow)
- Material performance 240,0 kg/h (from 40% moisture content to 15%)
- Drying temperature: 180-230 °C
- Required electric performance: 3,0 kW

Drying and carbonizing are done through direct heat exchange. Using the material transport, identical material is consistently being fed into the internal space, which makes the processed material consistent in homogeneity and quality. Better heat exchange and equalised heat energy distribution is supported by circulating the gas sourced from the reactor mantle, and the drying space filled by it. The intake of high-temperature gas is done by a gas stream pump. In truth, during the carbonization process, pyrolysis gases from the process are being combusted, which supplies the energy required for the system's heat requirement.

The carbonization reactor's:

- temperature setting is 600-900 °C.
- biochar production capacity is 50-100 kg/h
- exhaust gas temperature is 300-400 C°
- electric performance requirement is 5,0 kW
- main dimensions are 6,0 x 2,4 x 3,6 m
- weight is 3400 kg
- manufactured material temperature is 180 C°
- performance from absorbing exhaust gas temperature is 100 kW.

The control of the entire system is done via a digital interface. The central panel shows not only the current data of the process, but also possible errors in real time (Fig. 11)

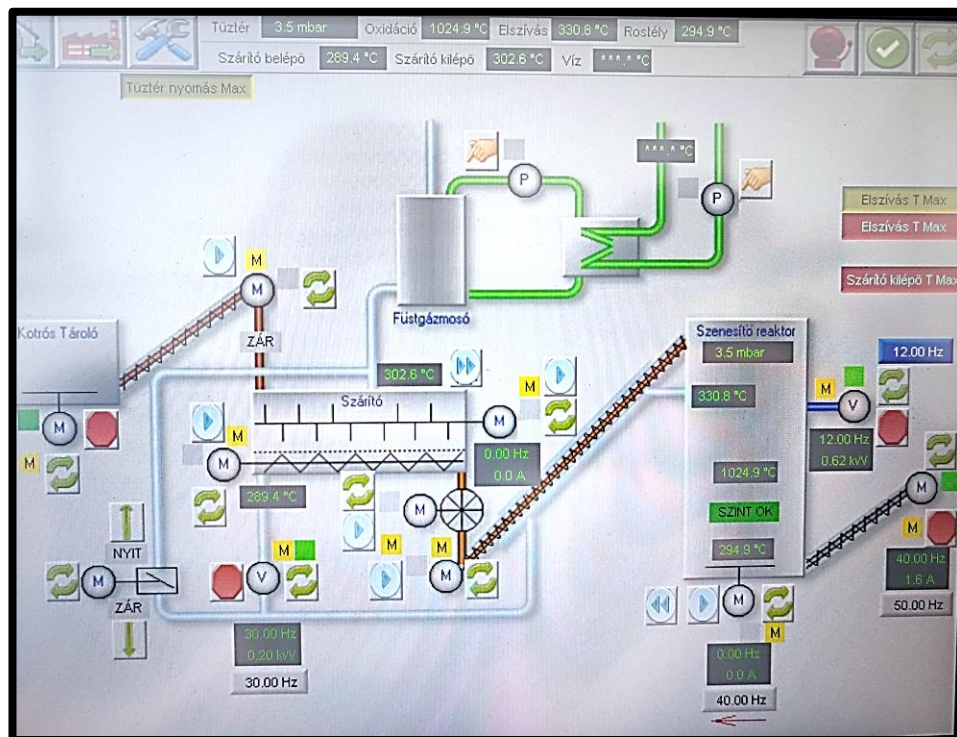


Figure 11. Management panel of the device

The filtered hardwood fed into the machine during startup was carbonized. We determined the size dimensions of the resulting carbon grains (Table 2)

Table 2. Biochar grains classified by size

Grain size [mm]	Mass [%]
3,15-6,3	3,9
2,0 - 3,15	15,1
1,6 – 2,0	8,2
1,0- 1,6	<b>26,2</b>
0,63 -1,0	<b>19,5</b>
0,1 - 0,63	<b>18,18</b>
0,05	8,3

Hao Liang, et al stress the importance of this analysis, as within the biochar, several different size groups of pores exist, classified into micro- (<2 nm), mid- (2 - 50 nm) and macro- (>50 nm) sized [19]. Smaller pore size biochar can only absorb f.e. pesticides in limited amounts. Grain size groups are better when biochar is made with a machine, roughly 65-70% if the resulting grains in the 1-1,6mm range. Therefore, the internal surface and the porosity are advantageous.

We analysed the composition of the material in an accredited lab, mainly from the perspective of various micro-element contents. Mulched and minced materials turned into biochar had a large variety of elements, of which heavy metals are way above the tolerable content limits. Due to the short-term heat zone, PAH materials decompose, which results in a low PAH content (PAH: 1,27mg/kg, total PCB <0,01mg/kg).

### 3.2. Biochar cost

The usage of biochar changes the properties of the soil, the production capacity of the soil is increased, and the costs of plant production are decreased (both in agricultural fields and greenhouses). Biochar remains in the soil in the long-term, throughout several production cycles, by which it expends its advantageous effects in the long-term too. Its usage reduces the necessity of phosphorus and potassium-containing fertilizers, which also reduces expenses used for these. The investment comes with an assured return.

Considering that biochar can be made out of various biological materials, waste, by-products, which are usually at hand in areas where plant production is also conducted, there is a possibility of making biochar a locally procurable resource. Local production reduces the transport costs, and the income of the production process also remains in local cashflows.

## 4. Conclusions

Biochar is a material reminiscent of coal, which is produced out of plant materials like wood waste, secondary products made from herbaceous plants, and remains of agri- and silviculture. These materials are decomposed using heat, which also generates renewable energy. During the process, the physical and chemical nature of the plant materials are changed into a porous and from a biological perspective, structurally stable material rich in carbon. Research done with this material shows that it can be used as a soil improvement material in agriculture and gardening, which means it influences several physical, chemical and biological attributes of the soil. It may also increase the water-sealing capacity. It minimises the alkalisation of nutrients, may improve the income of producers and sustainability of their businesses by increasing efficiency of fertilizer usage and reducing fertilizer costs. By increasing water-sealing capacity, biochar can decrease watering requirements, and may enable the extension of production even in less water-rich areas.

In summary, it modified the microbe culture of plants' root zones, and their habitat, which often leads to a bigger abundance of microbes, and better activity of them as well. This increases production yield. One must know that the usage of biochar is the most advantageous in a controlled environment. In the case of sandy, sour soil variants, every feedback is positive. We cannot exclude the fact that considering the production

process, and entire effect mechanism of biochar, reduces the carbon-dioxide emission into the atmosphere. Therefore, it is also an advantageous material for climate protection.

The machinery introduced is a so-called fixed bedding structure. Drying and carbonization is done via direct heat transfer. The material fed into the reactor is equalised in quality due to the pre-dryer. Better heat exchange and equalised heat energy distribution is supported by circulating the gas sourced from the reactor mantle, and the drying space filled by it. The intake of high-temperature gas is done by a gas stream pump. In truth, during the carbonization process, pyrolysis gases from the process are being combusted, which supplies the energy required for the system's heat requirement.

### Acknowledgement

The research was supported by the project 'Preparation for the transition to circular economy in the case of agricultural and green waste' of Environment and Energy Efficiency Operational Programme grant scheme of Ministry of Technology and Industry Hungary under grant no.: KEHOP-3.2.1-15-2021-00037.

### References

- [1] **Nastaran B. J. et al.** (2020) Photosynthesis, growth, and water use of *Hydrangea paniculata* 'Silver Dollar' using a physiological-based or a substrate physical properties-based irrigation schedule and a biochar substrate amendment. Springer-Verlag GmbH Germany, part of Springer Nature 2020, <https://www.researchgate.net/publication/339776264> [Downloaded: Jul 14. 2023.].
- [2] **Cégény Zs. et al.** (2017) Impact of torrefaction on woody biomass properties, *Energy Procedia* Elsevier, Volume 105 Pages 1149-1154, <https://www.sciencedirect.com/science/article/pii/S1876610217305271>
- [3] **Awasthi M. K., Wang M., Chen H., Wang Q., Zhao J., Ren X., Li D.-S., Awasthi S. K., Shen F., Li R., Zhang Z.** (2017) Heterogeneity of biochar amendment to improve the carbon and nitrogen sequestration through reduce the greenhouse gases emissions during sewage sludge composting, *Bioresour. Technol.* 224 (2017) 428–438.
- [4] **Babu B. V., Chaurasia A.S.** (2003) Modeling, simulation and estimation of optimum parameters in pyrolysis of biomass, *Energ. Convers. Manage.* 44 (2003) 2135– 2158.
- [5] **Cha J.S., Park S.H., Jung S.C., Ryu C., Jeon J.K., Shin M.C., Park Y.K.** (2016) Production and utilization of biochar: a review, *J. Ind. Eng. Chem.* 40 (2016) 1–15.
- [6] **Yaashikaaa P.R., Senthil K. P., Varjanic S.** (2020) A critical review on the biochar production techniques, characterization, stability and applications for circular bioeconomy *Biotechnology Reports*, Downloaded 2021 [www.elsevier.com/locate/btre](http://www.elsevier.com/locate/btre)
- [7] **Spokas K. A, Reicosky D. C.** (2009) Impacts of sixteen different biochars on soil greenhouse gas production. *Annals of Environmental Science*, 3:179-193 pp.
- [8] **Laird A. D.** (2008) The Charcoal Vision: A Win–Win–Win Scenario for Simultaneously Producing Bioenergy, Permanently Sequestering Carbon, while Improving Soil and Water Quality. *Agronomy Journal* 100:178-181 pp.
- [9] **Ahmed Y. E.** (1919) Effect of Pyrolysis Temperature on Biochar Microstructural Evolution, Physicochemical Characteristics, and Its Influence on Biochar/Polypropylene Composites, *Applied Sciences*. 9(6), 1149; doi:10.3390/app9061149
- [10] **Hunt J., Duponte M., Sato D., Kawabata A.** (2010) The basics of Biochar: A natural Soil Amendment. *Soil and Crop Management*, College of Tropical Agriculture and Human Resources, 30:1-6 pp.
- [11] **Steiner C., Garcia M., Zech W.** (2009) Effects of charcoal as slow release nutrient carrier on NPK dynamics and soil microbial population: pot experiments with ferralsol substrate. Springer, Berlin. 325-338 pp.
- [12] **Kocsis T.** (2018) Bioszén és bioeffektor kombinációk hatása homoktalajok biológiai tulajdonságaira, Ph.D. tethesis [https://archive.szie.hu/sites/default/files/kocsis\\_tamas\\_ertekezes.pdf](https://archive.szie.hu/sites/default/files/kocsis_tamas_ertekezes.pdf) (Downloaded: 2021)
- [13] **Rékási M., Uzinger N.** (2015) A bioszén felhasználásának lehetőségei a talaj tápanyag-utánpótlásában. *Agrokémia és Talajtan*, 64:239-256 pp
- [14] **Chen B. L., Yuan M. X.** (2011) Enhanced sorption of polycyclic aromatic hydrocarbons by soil amended with biochar. *Journal of Soil and Sediments*, 11:62-71 pp.

- [15] **Downie A., Crosky A., Munroe P.** (2009) Physical properties of biochar. In 'Biochar for environmental management: Science and technology.' (Eds J Lehmann and S Joseph) Earthscan: London. Sterling, VA, USA. 13-32pp.
- [16] **Amonette J. E., Joseph S.** (2009) Characteristics of biochar: microchemical properties. In: Lehmann, J., Joseph, S. (Eds.), Biochar for Environmental Management: Science and Technology. Earthscan. London. 33-52 pp.
- [17] **Madár V., Tóth L., Madár Gy., Schrempf N.** (2014) Kísérleti fagázgenerátor, Mezőgazdasági Technika, ISSN 0026 1890. 55. évf. Nr. 4. pp. 2-5.
- [18] **Tóth L., Madár V., Bácskai I.** (2019) Pírolízis berendezés fejlesztését megelőző vizsgálatok, Energiagazdálkodás, 60. évf. 1-2. pp. 27-33.
- [19] **Liang H, et all.**, Surface morphology properties of biochars produced from different feedstocks College of Environmental Science and Engineering, Ocean University of China, Qingdao 266100,

# **AGRICULTURAL APPLICATIONS OF THE DISCRETE ELEMENT METHOD**

**Author(s):**

J. Huang<sup>1</sup>, I. Keppler<sup>1</sup>

**Affiliation:**

<sup>1</sup> Institute of Technology - Hungarian University of Agriculture and Life Sciences, 2100 Gödöllő, Páter Károly u. 1., Hungary.

**Email address:**

junhao.huang@phd.uni-mate.hu; keppler.istvan@uni-mate.hu

**Abstract:** The global population has been steadily increasing, putting pressure on available resources, including agricultural land. The decrease of available agricultural land has made it difficult to sustainably produce enough food to feed the growing population. Global warming and water issues have also made it challenging to grow crops, with changing weather patterns and water scarcity affecting yields. To address these challenges, there is a need to modernize agricultural technologies. One of the available possibilities is the improvement of post-harvest technologies. By gaining more knowledge on the mechanical behavior of particulate materials using discrete element modeling, it may be possible to optimize post-harvest technologies for food processing and storage. This could lead to improvements in the quality and safety of food products while reducing waste and increasing efficiency. This paper reviews the key literature concerned with the agricultural applications and DEM parameters calibration of agricultural particles, which generally are corn, rice, wheat, soybean, sunflower seed and soil particles.

**Keywords:** agricultural particles, discrete element method, calibration

## **1. Introduction**

The discrete element method (DEM) proposed by Cundall and Strack in 1979 [1] is a numerical analysis method for describing the motion and interactions of particles based on Newton's second law [2]. With the development of hardware and software, the computational power of DEM simulation has increased significantly, and the application of DEM in modeling the mechanical behavior of agricultural particulate materials is becoming more and more widespread. Finding the micromechanical properties of these (the so-called calibration procedure) is a time- and computational resource-intensive process. The calibration of DEM is particularly important.

Our goal is to demonstrate the applicability of the DEM method in agricultural engineering-related problems and to introduce the reader to the calibration problem. Through advancements in agricultural technology, it may be possible to increase food production while minimizing the negative impact on the environment, ultimately contributing to the sustainability of our planet. Many of the technological processes involved in agricultural mechanical engineering can be interpreted as the interaction of a granular material assembly with a body in contact with or moving in it. Such is the interaction between the soil-tillage tool, the soil wheel, the grain-silo, and the grain-material handling machine. In the technical design of these processes, the most difficult problem is the correct interpretation and accurate modeling of the phenomena occurring at the interface of the granular material assembly and the body.

## **2. Materials and Methods**

Many studies regarding agricultural granular materials have used DEM modeling to validate the interaction of contacted particles and reproduce the dynamic behavior of agricultural particles based on the calibrated

micromechanical parameters. The micromechanical parameters are almost difficult to measure directly, and their values need to be systematically modified according to the modeled macro behavior until the particle assembly is the same as the real behavior of the particle [3], [4], this is so-called calibration. The calibration is the most time- and resource-consuming part of the DEM modeling, and it would be a really good thing from application point of view to have an available database of pre-calibrated data for the different agricultural crop particles DEM simulations. The micromechanical parameters of static and dynamic friction coefficients, and rolling and sliding friction coefficients of wheat particles were calibrated in their research works [5], [6], [7] to determine the interaction of contacted particles and particle-wall. Validation of corn flow in a commercial screw auger was conducted by [8] to get a better understanding of the interaction between corn particles and particle-wall based on the DEM modeling. To determine the impact of the number of paddles and the filling configuration on the mixing rate of a single-shaft paddle mixer, [9] performed DEM simulations on corn particles.

### 2.1 Agricultural applications of DEM

DEM simulation is considered as a powerful method to numerically simulate interactions between the contacting areas for the agricultural particles. Effect of tool vibration has been investigated by DEM [10] (Fig. 1). Predicting the discharge rate from a rectangular hopper, simulating the compression tests, loading in silos and gravity flowing in silos using the DEM [11], [12], [13]. The DEM has been used to simulate the interactions between fruits to predict the dynamic behavior of apples and grapes [14], [15], [16], and maize stalk, cotton stalk, and citrus fruit stalk [17], [18], [19]. DEM simulations are also widely used for the flow of agricultural granular materials in chutes, the shear cell shown in Fig. 2, and dryers shown in Fig. 3 [20], [21], [22], [23]. The vane shear testing experiments were also conducted with DEM shown in Fig. 4 [24]. The agricultural particle screening during the combine harvester [25] and high capacity vibrating screening for non-spherical particles [26] are studied based on the DEM simulations. Many cases apply the DEM simulations in food processing, such as the food grains drying process [27], [28] and the collision of amorphous food particles during spray drying for particle-wall [29]. This paragraph talked about the agricultural products relating to the DEM simulation.

This paragraph collects agricultural applications of soil and fertilizer particles with DEM. [30], [31], [32] studied the bulk residual soil strength, the mapping relationship of soil stress-strain, constitutive response prediction of both dense and loose soils and the dynamic interactions that happen during the soil tillage process with DEM simulations. Fertilizer granular materials play a very important role in agricultural production activities. Calibration of micromechanical parameters of fertilizer particles, the study of the interaction between fertilizer granules and agricultural machinery and equipment, the dual-band application of fertilizer particles, and the application of broken solid organic fertilizers in cultivated land [4], [33], [34], [35], [36] are examples of DEM used in fertilizer simulations.

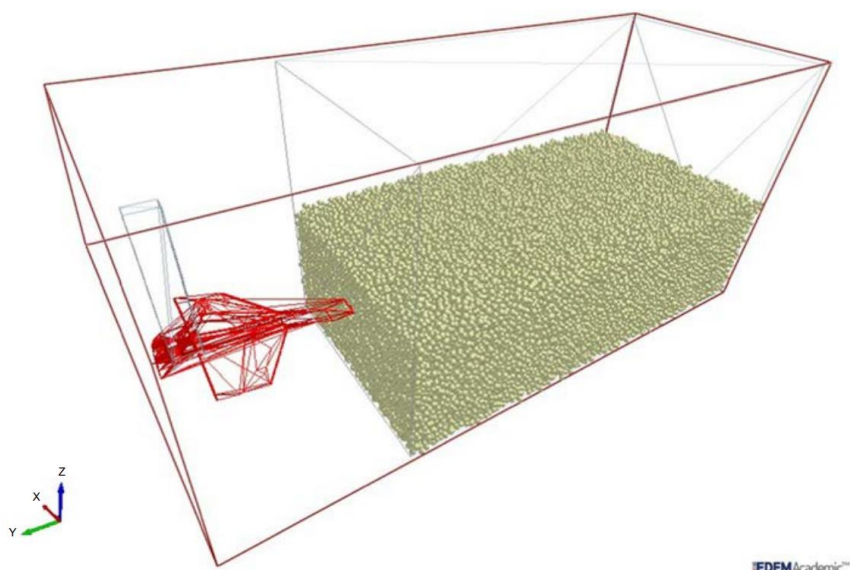


Figure 1. Effect of tool vibration has been investigated by DEM [10]

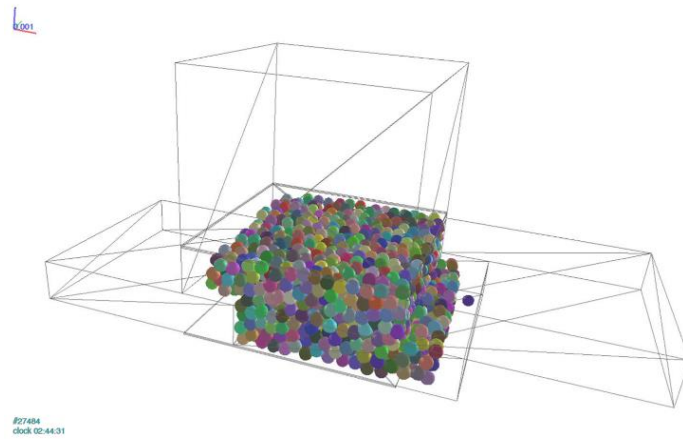


Figure 2. DEM modeling of the shear cell [37]

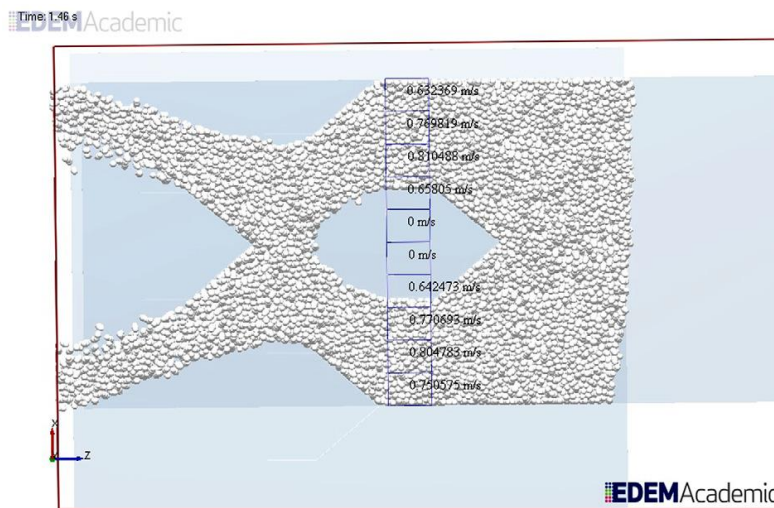


Figure 3. Binning of the dryer section [20]

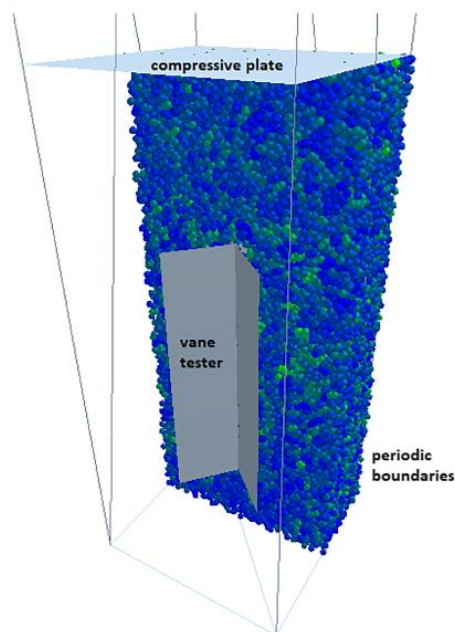


Figure 4. DEM model of vane shear testing apparatus [24]

### 2.2 The calibration problems

DEM simulations need to consider several factors such as the shape, size, surface properties and material characteristics of the particles. The complexity of these factors makes it necessary to involve many parameters in the simulation, some of which may be difficult to measure and estimate. The transportation of agricultural particles from the original place to the measurement laboratory may cause changes in some micromechanical parameters due to the change in particle moisture content, thereby, [24] developed the in-situ calibration method to avoid these problems. [37] applied the rectangular lid instead of a circular shear lid shown in Fig. 5, so it is a shear box, followed by a detailed sensitivity analysis using shear testing experiments. The internal friction angle of corn and the friction angle of corn-steel and corn-glass were determined by direct shear testing with a shear box [38]. The experimental results show that inconsistent with each other. The calibration is extremely difficult since the differences in calibration environment and calibration methods can lead to very different results. The relative error (RE) of the bulk angle of repose was 0.39% [13] using the particle scaled-up method in the DEM parameters calibration for rice grains. [3] used a two-spherical clump as the simulated shape of corn granules and calibrated the angle of repose of corn particles with the help of a cylinder shown in Fig. 6.

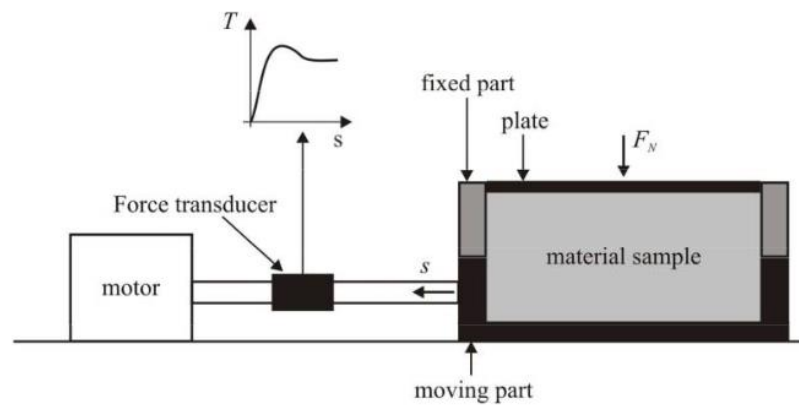


Figure 5. Shear box [37]

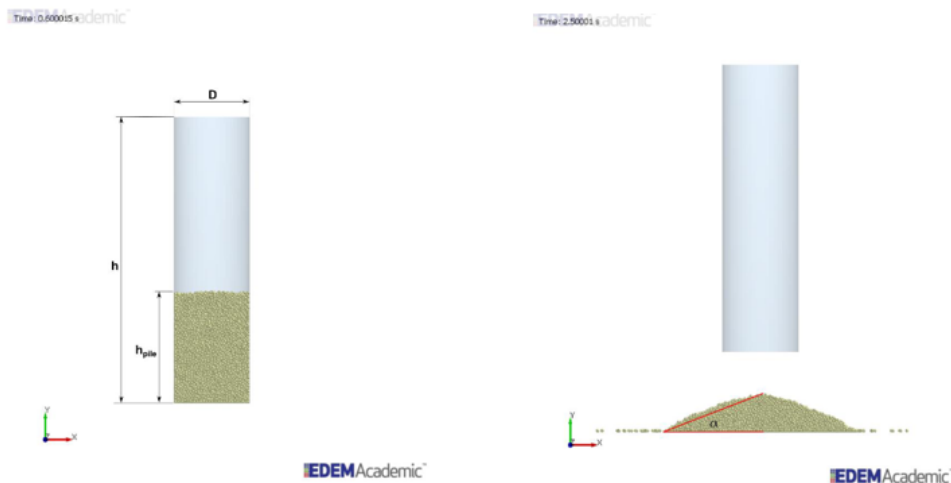


Figure 6. The measurement process of the angle of repose [3]

### 3. Conclusions

This literature review is about the numerical simulation of agricultural granular materials based on DEM. It mainly reviews the agricultural application possibilities of the discrete element method (DEM) simulating

and calibrating the micromechanical parameters of granular materials and understanding the interactions between particles and particle-wall, so that the DEM simulation can reproduce the dynamic behavior of the agricultural particles.

The calibration of microparameters is a fundamental and ongoing challenge in DEM simulation, and it plays a critical role in the DEM simulation for agricultural application purposes. As the field continues to advance, new methods and techniques for calibration are likely to emerge, enabling even more powerful and accurate simulations of complex systems. DEM modeling can be used more widely in agricultural applications. The aim of our research is to provide practicing engineers with a database that they can use to focus directly on the field of engineering problem they are solving, without having to spend time on calibration.

### Acknowledgement

This study is supported by the China Scholarship Council (CSC) and the Stipendium Hungaricum Scholarship programme.

### References

- [1] **P. A. Cundall and O. D. L. Strack**, “Discussion: A discrete numerical model for granular assemblies,” *Geotechnique*, vol. 30, no. 3, pp. 331–336, Sep. 1980, doi: 10.1680/geot.1980.30.3.331.
- [2] **C. Hoshishima, S. Ohsaki, H. Nakamura, and S. Watano**, “Parameter calibration of discrete element method modelling for cohesive and non-spherical particles of powder,” *Powder Technology*, vol. 386, pp. 199–208, 2021, doi: <https://doi.org/10.1016/j.powtec.2021.03.044>.
- [3] **A. Bablena, N. Schrempf, and I. Keppler**, “The effect of particle shape on the angle of repose test based calibration of discrete element models,” *Hungarian Agricultural Engineering*, no. 40, pp. 39–46, 2021, doi: 10.17676/HAE.2021.40.39.
- [4] **X. Song, F. Dai, F. Zhang, D. Wang, and Y. Liu**, “Calibration of DEM models for fertilizer particles based on numerical simulations and granular experiments,” *Computers and Electronics in Agriculture*, vol. 204, p. 107507, Jan. 2023, doi: 10.1016/j.compag.2022.107507.
- [5] **Z. Chen, C. Wassgren, E. Veikle, and K. Ambrose**, “Determination of material and interaction properties of maize and wheat kernels for DEM simulation,” *Biosystems Engineering*, vol. 195, pp. 208–226, Jul. 2020, doi: 10.1016/j.biosystemseng.2020.05.007.
- [6] **J. Horabik et al.**, “Calibration of discrete-element-method model parameters of bulk wheat for storage,” *Biosystems Engineering*, vol. 200, pp. 298–314, Dec. 2020, doi: 10.1016/j.biosystemseng.2020.10.010.
- [7] **K. Sun et al.**, “A DEM-based general modelling method and experimental verification for wheat seeds,” *Powder Technology*, vol. 401, p. 117353, Mar. 2022, doi: 10.1016/j.powtec.2022.117353.
- [8] **M. Mousaviraad, M. Z. Tekeste, and K. A. Rosentrater**, “Calibration and Validation of a Discrete Element Model of Corn Using Grain Flow Simulation in a Commercial Screw Grain Auger,” *Transactions of the ASABE*, vol. 60, no. 4, pp. 1403–1415, 2017, doi: 10.13031/trans.12200.
- [9] **S. Garneoui, P. Korzenszky, and I. Keppler**, “Enhancement of the mixture quality of corn grains in a single-shaft paddle mixer using DEM simulations,” *J Mech Sci Technol*, Feb. 2023, doi: 10.1007/s12206-023-0223-1.
- [10] **I. Keppler, Z. Hudoba, I. Oldal, A. Csatar, and L. Fenyvesi**, “Discrete element modeling of vibrating tillage tools,” *Engineering Computations*, vol. 32, no. 2, pp. 308–328, Apr. 2015, doi: 10.1108/EC-10-2013-0257.
- [11] **A. Anand, J. S. Curtis, C. R. Wassgren, B. C. Hancock, and W. R. Ketterhagen**, “Predicting discharge dynamics of wet cohesive particles from a rectangular hopper using the discrete element method (DEM),” *Chemical Engineering Science*, vol. 64, no. 24, pp. 5268–5275, Dec. 2009, doi: 10.1016/j.ces.2009.09.001.
- [12] **A. O. Raji and J. F. Favier**, “Model for the deformation in agricultural and food particulate materials under bulk compressive loading using discrete element method. I: Theory, model development and validation,” *Journal of Food Engineering*, vol. 64, no. 3, pp. 359–371, Sep. 2004, doi: 10.1016/j.jfoodeng.2003.11.004.

- [13] **S. Zhang, M. Z. Tekeste, Y. Li, A. Gaul, D. Zhu, and J. Liao**, “Scaling of the angle of repose test and its influence on the calibration of DEM parameters using upscaled particles,” *Biosystems Engineering*, vol. 194, pp. 196–212, Jun. 2020, doi: 10.1016/j.biosystemseng.2020.03.018.
- [14] **C. González-Montellano, E. M. Baguena, Á. Ramírez-Gómez, and P. Barreiro**, “Discrete element analysis for the assessment of the accuracy of load cell-based dynamic weighing systems in grape harvesters under different ground conditions,” *Computers and Electronics in Agriculture*, vol. 100, pp. 13–23, Jan. 2014, doi: 10.1016/j.compag.2013.10.008.
- [15] **J. Kafashan, J. Wiacek, H. Ramon, and A. M. Mouazen**, “Modelling and simulation of fruit drop tests by discrete element method,” *Biosystems Engineering*, vol. 212, pp. 228–240, Dec. 2021, doi: 10.1016/j.biosystemseng.2021.08.007.
- [16] **M. Van Zeebroeck et al.**, “The discrete element method (DEM) to simulate fruit impact damage during transport and handling: Model building and validation of DEM to predict bruise damage of apples,” *Postharvest Biology and Technology*, vol. 41, no. 1, pp. 85–91, Jul. 2006, doi: 10.1016/j.postharvbio.2006.02.007.
- [17] **Á. Ramírez-Gómez, E. Gallego, J. M. Fuentes, C. González-Montellano, and F. Ayuga**, “Values for particle-scale properties of biomass briquettes made from agroforestry residues,” *Particuology*, vol. 12, pp. 100–106, Feb. 2014, doi: 10.1016/j.partic.2013.05.007.
- [18] **Y. Wang et al.**, “Discrete element modelling of citrus fruit stalks and its verification,” *Biosystems Engineering*, vol. 200, pp. 400–414, 2020, doi: <https://doi.org/10.1016/j.biosystemseng.2020.10.020>.
- [19] **W. Zhao, M. Chen, J. Xie, S. Cao, A. Wu, and Z. Wang**, “Discrete element modeling and physical experiment research on the biomechanical properties of cotton stalk,” *Computers and Electronics in Agriculture*, vol. 204, p. 107502, Jan. 2023, doi: 10.1016/j.compag.2022.107502.
- [20] **I. Keppler, L. Kocsis, I. Oldal, I. Farkas, and A. Csatar**, “Grain velocity distribution in a mixed flow dryer,” *Advanced Powder Technology*, vol. 23, no. 6, pp. 824–832, Nov. 2012, doi: 10.1016/j.apt.2011.11.003.
- [21] **O. A. Khachatourian, M. O. Binelo, and R. F. De Lima**, “Simulation of soya bean flow in mixed-flow dryers using DEM,” *Biosystems Engineering*, vol. 123, pp. 68–76, Jul. 2014, doi: 10.1016/j.biosystemseng.2014.05.003.
- [22] **T. Ou and W. Chen**, “On accurate prediction of transfer chute wear using a digital wear sensor and discrete element modelling,” *Powder Technology*, vol. 407, p. 117680, 2022, doi: <https://doi.org/10.1016/j.powtec.2022.117680>.
- [23] **X. Zhang and L. Vu-Quoc**, “Simulation of chute flow of soybeans using an improved tangential force±displacement model,” *Mechanics of Materials*, 2000.
- [24] **I. Keppler, A. Bablena, N. D. Salman, and P. Kiss**, “Discrete element model calibration based on *in situ* measurements,” *EC*, vol. 39, no. 5, pp. 1947–1961, May 2022, doi: 10.1108/EC-05-2021-0288.
- [25] **Z. Ma, Y. Li, and L. Xu**, “Discrete-element method simulation of agricultural particles’ motion in variable-amplitude screen box,” *Computers and Electronics in Agriculture*, vol. 118, pp. 92–99, Oct. 2015, doi: 10.1016/j.compag.2015.08.030.
- [26] **J. W. Fernandez, P. W. Cleary, M. D. Sinnott, and R. D. Morrison**, “Using SPH one-way coupled to DEM to model wet industrial banana screens,” *Minerals Engineering*, vol. 24, no. 8, pp. 741–753, Jul. 2011, doi: 10.1016/j.mineng.2011.01.004.
- [27] **J. Azmir, Q. Hou, and A. Yu**, “CFD-DEM study of the effects of food grain properties on drying and shrinkage in a fluidised bed,” *Powder Technology*, vol. 360, pp. 33–42, Jan. 2020, doi: 10.1016/j.powtec.2019.10.021.
- [28] **J. Azmir, Q. Hou, and A. Yu**, “CFD-DEM simulation of drying of food grains with particle shrinkage,” *Powder Technology*, vol. 343, pp. 792–802, Feb. 2019, doi: 10.1016/j.powtec.2018.11.097.
- [29] **M. W. Woo, W. R. W. Daud, A. S. Mujumdar, S. M. Tasirin, and M. Z. M. Talib**, “Role of rheological characteristics in amorphous food particle-wall collisions in spray drying,” *Powder Technology*, vol. 198, no. 2, pp. 251–257, Mar. 2010, doi: 10.1016/j.powtec.2009.11.015.
- [30] **Z. Asaf, D. Rubinstein, and I. Shmulevich**, “Determination of discrete element model parameters required for soil tillage,” *Soil and Tillage Research*, vol. 92, no. 1–2, pp. 227–242, Jan. 2007, doi: 10.1016/j.still.2006.03.006.

- [31] **Z. Syed, M. Tekeste, and D. White**, “A coupled sliding and rolling friction model for DEM calibration,” *Journal of Terramechanics*, vol. 72, pp. 9–20, Aug. 2017, doi: 10.1016/j.jterra.2017.03.003.
- [32] **Z. Wu et al.**, “Calibration of discrete element parameters and experimental verification for modelling subsurface soils,” *Biosystems Engineering*, vol. 212, pp. 215–227, 2021, doi: <https://doi.org/10.1016/j.biosystemseng.2021.10.012>.
- [33] **S. Adilet et al.**, “Calibration Strategy to Determine the Interaction Properties of Fertilizer Particles Using Two Laboratory Tests and DEM,” *Agriculture*, vol. 11, no. 7, 2021, doi: 10.3390/agriculture11070592.
- [34] **G. Chen, Q. Wang, D. Xu, H. Li, J. He, and C. Lu**, “Design and experimental research on the counter roll differential speed solid organic fertilizer crusher based on DEM,” *Computers and Electronics in Agriculture*, vol. 207, p. 107748, Apr. 2023, doi: 10.1016/j.compag.2023.107748.
- [35] **S. Ding et al.**, “Discrete element modelling (DEM) of fertilizer dual-banding with adjustable rates,” *Computers and Electronics in Agriculture*, vol. 152, pp. 32–39, Sep. 2018, doi: 10.1016/j.compag.2018.06.044.
- [36] **S. Yinyan, C. Man, W. Xiaochan, M. O. Odhiambo, and D. Weimin**, “Numerical simulation of spreading performance and distribution pattern of centrifugal variable-rate fertilizer applicator based on DEM software,” *Computers and Electronics in Agriculture*, vol. 144, pp. 249–259, Jan. 2018, doi: 10.1016/j.compag.2017.12.015.
- [37] **I. Keppler, F. Safranyik, and I. Oldal**, “Shear test as calibration experiment for DEM simulations: a sensitivity study,” *Engineering Computations*, vol. 33, no. 3, Jan. 2016, doi: 10.1108/EC-03-2015-0056.
- [38] **C. J. Coetzee and D. N. J. Els**, “Calibration of discrete element parameters and the modelling of silo discharge and bucket filling,” *Computers and Electronics in Agriculture*, vol. 65, no. 2, pp. 198–212, Mar. 2009, doi: 10.1016/j.compag.2008.10.002.

# LITERATURE REVIEW ON SOLAR ENERGY AND BIOGAS UTILISATION FOR THE DEVELOPMENT OF SCALABLE CO-GENERATION POWER PLANTS

## Author(s):

L. Magó<sup>1</sup>, I. Seres<sup>2</sup>, P. Víg<sup>2</sup>, G. Bércesi<sup>1</sup>, K. Szalay<sup>1</sup>, J. Deákvári<sup>1</sup>, P. Gárdonyi<sup>1</sup>, Z. Kurják<sup>1</sup>

## Affiliation:

<sup>1</sup> Institute of Technology – Hungarian University of Agriculture and Life Sciences, 2100 Gödöllő, Páter Károly u. 1., Hungary.

<sup>2</sup> Institute of Mathematics and Basic Science – Hungarian University of Agriculture and Life Sciences, 2100 Gödöllő, Páter Károly u. 1., Hungary.

## Email address:

Mago.Laszlo@uni-mate.hu; Seres.Istvan@uni-mate.hu; Vig.Piroska@uni-mate.hu; Bercesi.Gabor@uni-mate.hu; Szalay.Kornel@uni-mate.hu; Deakvari.Jozsef@uni-mate.hu; Gardonyi.Peter@uni-mate.hu; Kurjak.Zoltan@uni-mate.hu

**Abstract:** In this paper, we present the research results related to the project "Development and implementation of a scalable co-generation power plant solution integrating solar energy and biomass utilisation". Our objective is to develop an integrated solution in the field of local renewable and sustainable energy production, storage and use, where solar energy collected by PV/T collector, hydrogen and oxygen gas production by water decomposition, and biogas production by biomass utilisation are integrated into an innovative process, in different scales (scalable), to produce a compact device, which stores solar energy in the form of combustible gas in a container. Our research team members are working on different areas of tasks to achieve this goal. This article reviews the results of the first phase of this work, which involved a literature review and a groundwork.

**Keywords:** solar panel, solar collector, water purification, biogas components, gas mixture

## 1. Introduction

The use of renewable energies is an essential option for energy production [1], [2], [3]. Among these, the use of solar panels and solar collectors, which actively harness solar energy, is significant today. Solar panels generate electricity directly, while solar collectors generate heat water.

Storage of energy from renewables is also a cardinal issue. Practical solutions and their commercially successful forms have not yet led to any socio-economic breakthroughs, but it is one of the most researched areas. This area is critical if environmental and nature conservation aspects are considered, i.e. renewable and sustainable energy production [4], [5], [6].

The current implementation of some technologies for renewable and sustainable energy production is fragmented. Solar farms for electricity generation are built separately, solar collectors for domestic hot water are constructed separately, biogas plants are set up separately, and wind farms are installed individually. The project proposal provides a solution to the challenges where innovative integrated energy solutions are developed in a common field of local potential and high-tech solutions. This new solution will enable both local needs and global challenges to be met in a technically better and more economical way than has previously been possible.

The new solution to be developed:

- integrates the production of hydrogen by solar panels to improve biogas,
- provides a solution for the local use of oxygen,
- enables local renewable (solar) and sustainable (biogas) production,
- provides energy storage adapted to local variable energy demand,

- can be installed in several sizes.

This solution aims to achieve integration at the process level, i.e., one technology enhances the goodness and efficiency of the other process. This aim will be achieved using the advanced elements of the digitalisation and Industry 4.0 technology platform, particularly artificial intelligence-based algorithms and sensor systems as data sources. The R&D project aims to synthesise these two areas to create a marketable, complex physical energy production system that does not yet exist, creating a technology transfer (know-how) that can be sold on the global market.

The device is built up of the modules illustrated in Figure 1. The photovoltaic (PV) module, which is the starting element, uses solar energy to generate electricity, which is then used by the next element to produce hydrogen and oxygen from the decomposition of water.

The third key element of the system is the biogas module. This element uses thermal energy generated by a solar collector to increase the efficiency of the fermentation process. The composition and energy content of the resulting biogas can be increased by adding hydrogen gas obtained from the previous modules.

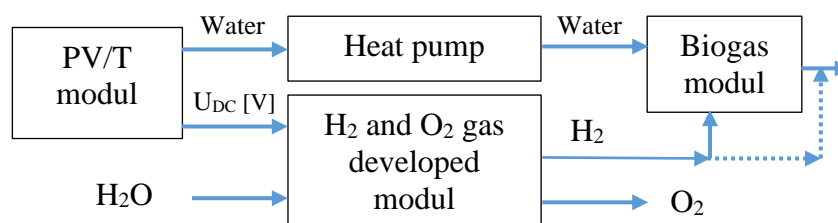


Figure 1. Modules of the designed scalable co-generation device

In this section of our research work, we reviewed the literature related to the design, functioning and use of the presented modules (solar panel, solar collector, water purification, fermentor), the composition of input/output materials, as well as the studies carried out in related fields. The following literature review will be presented on solar cells, solar collectors, water decomposition, biogas production, biogas composition, biogas utilisation, and gas mixtures.

## 2. Literature review

### 2.1. Solar photovoltaic cells

This chapter focuses on solar cells, which convert solar energy directly into electricity. In addition to the types of solar panels, the methods used to store the energy produced and the technical devices used for this purpose are also discussed.

The types of solar cells produced by different technologies were reviewed, ranging from traditional silicon-based solar cells to emerging technologies currently in the experimental stage [7].

To evaluate the different technologies, we need to consider the fulfilment of several criteria, the most important of which are [8]:

- high-efficiency opportunity
- availability of materials used
- reasonable cost of materials
- the possibility of low production cost technology
- product stability over time (decades)
- environmentally friendly product and production technology

Today, the market is dominated by silicon-based solar cells, crystalline silicon in cells made using slice technology and amorphous silicon made using thin film technology [9].

Most solar cells are made from crystalline silicon and are very similar in design to silicon-based devices such as rectifier diodes. The technology uses silicon plates and is therefore called slice technology. The advantage is that it is self-carrying; the disadvantage is that it requires a large quantity, expensive, semiconducting, high-quality material [10].

- Crystalline silicon solar cells
  - Monocrystalline silicon solar cells
  - Polycrystalline silicon solar cells
  - Silicon Ribbon Solar Cells
- Thin film solar cells
  - Amorphous silicon solar cells
  - Gallium Arsenide (GaAs) Solar cells
  - Cadmium telluride (CdTe) based solar cells
  - Copper Indium Diselenide (CIS and CIGS) solar cells
- Emerging solar technologies
  - Dye-sensitised solar cells
  - Organic solar cells
  - CZTS solar cells
  - Perovskite solar cells
  - Quantum dot solar cells
  - Multi-junction solar cells

The method of determining the amperage current-voltage (I-V) characteristic, an essential characteristic of solar cells, and through this, the determination of the maximum operating power point of a solar cell, including the influence of environmental factors (temperature, intensity) on this characteristic, has been developed [11], [12], [13].

Special attention will be given to grid-connected solar PV systems and the grid inverters needed to operate them, showing the main types used [14], [15], [16].

We have also reviewed the characteristics of off-grid solar PV systems, focusing on the characteristics of battery farms for storing the energy produced and the typical types of batteries used [17].

We have examined the problem of charge controllers for battery operation and the problem of island mode inverters [18], [19]. We have also looked at the possibility of combining other energy sources with solar PV systems in a hybrid system to achieve energy security [20], [21], [22], [23], [24].

## **2.2. Solar thermal collectors**

The following will present the situation and potential of solar thermal energy. Accordingly, an overview of solar collector design, operation, development history, types, applications, and solutions to improve efficiency and effectiveness will be presented based on the available literature. Following these aspects, PV/T collectors will be reviewed, followed by heat exchangers and heat storage, based on available publications and their results. The chapter concludes with a literature review on heat pumps for thermal utilisation.

Since in an in-use building, in addition to the demand for electricity, there is also a need for heating (hot water production, space heating) [25] and cooling (space cooling), an obvious solution is to use waste heat by placing a collector behind the solar panels and at the same time improve the efficiency of the solar panel due to the lower operating temperature. However, the investment costs are higher for PV/T than for PV, as the system must be built for both utilisations. If a heat pump is planned in the system, PV/T is a more optimal solution than PV, as hot water and heating are also required.

However, there are also cases where the production of hot water (in swimming pools, and food processing plants) is solved by air-to-water heat pumps [26], [27], [28]. Another common form of heat pump is the ground source heat pump, which can also be used to produce hot water and thus heat buildings [29]. In this project, we are using a water-to-water heat pump.

The research results of the PV/T system, detailed below, form the basis of this technology and show the future trend of the PV/T system.

Ramos et al. conducted a theoretical and experimental thermographic analysis of the PV/T system investigated in their case study under different conditions [30]. Their results show that PV/T can produce significantly more energy at maximum solar energy values than PV.

In summer operation, Shao et al. analysed the efficiency of a PV/T system and compared it with the results obtained by operating only the PV part [31]. Their results show that the performance and efficiency of PV/T are always higher than those measured for PV.

Liang et al. conducted an empirical study to investigate the performance of a graphite-filled PV/T collector. Their research results showed that between 8:00 and 16:00 h, the average electrical efficiency of the PV/T collector and the classical PV module was 6.46% and 5.15%, respectively, i.e., PV/T in this form resulted in an additional electrical efficiency of 25.4% [32].

Duffie and Beckman also investigated the temperature distribution of the flat plate collector perpendicular to the direction of the fluid flow, showing that the temperature is higher between the tubes than around the tubes because there is not as much heat transport and dissipation [33]. However, due to the good thermal conductivity of the material connecting the tube to the absorber, the temperature inside the tube can be considered the same.

A delay in the change in the temperature of the solar fluid reflects the change in radiation. In the transient case, the response function is the solar fluid temperature curve plotted as a function of elapsed time. The time over which the temperature change in the collector due to the change in radiation decreases to one per  $e$  parts is called the collector time constant [34].

The time constants of collectors have been determined for various flat plate collectors by Pierson and Padet [35]. They investigated the effect of different collector parameters (absorber thickness, glass cover thickness, number of glass layers, heat capacity and mass flow of the working medium) on this value and found a numerical correlation between them.

The first theoretical context for the response function was given by Rogers [36]. The transient behaviour of collectors was described by Hill et al., De Ron and Kamminga [37], [38], [39]. A practical method for determining the response function characteristics was developed by Prapas et al., which gives the thermal characteristics of the collector step by step over short time intervals [40].

Physically based models become more complex and challenging to solve if they consider more influencing factors. In contrast to these models, new modelling methods can be applied, e.g. artificial intelligence-based models.

Cooling PV and increasing the efficiency of thermal utilisation with liquid is more effective than with air due to the higher specific heat and surface heat transfer coefficient. Thus, liquid PV/T is more efficient than air PV/T; however, when coupled to a heat pump system, the use of liquid heat pumps requires soil works, while the air solution is more favourable in terms of mobility [41], [42], [43].

The literature gives many examples of the benefits of combining PV and heat pumps if we also wish to produce heat with the energy system. With mobility in mind, air-source heat pumps are a more viable option. Once the energy needs have been estimated, sizing is necessary for optimal system operation. Connecting the heat pump to a solar panel makes the system greener, and even off-grid can be achieved. If a heat pump is combined with a PV/T collector, thermal and electrical efficiency is improved, but the system becomes more complex, which is a disadvantage during construction, and PV/T is less scalable due to the limited supply, which is also a disadvantage.

### ***2.3. The importance of water electrolysis (Hydrogen production) in energy production, storage, and utilisation***

Only water electrolysis technologies can achieve the required production volume among the green hydrogen production solutions. Electricity-based water decomposition is also the most important of the water separation technologies, and therefore, investigating the efficiency of these technologies and their potential for improvement is a current topic in energy research worldwide.

A considerable amount of research focuses on the time evolution of cell voltage, i.e., the change in electrical potential as a function of time, which significantly impacts the water electrolysis process. The electric current causes water molecules to split into hydrogen and oxygen gases, but the speed and efficiency of this process are highly dependent on the level and changes in the electric voltage.

Frequent fluctuations or continuous changes in the cell voltage also affect the efficiency of the cell, the performance of the cell and the amount of gas produced. The rate of change depends on the parameters of the voltage connected to the cell, i.e. its characteristics, amplitude, frequency and offset.

The literature on variable-current water splitting is mainly concerned with the effects of voltage pulses and intermittent direct current [44], [45], [46], [47], [48]. In the literature on the subject, we can find contradictory information, with some authors publishing results that are far from the reality: 96.8% energy savings with

high-frequency pulses [47], or even unrealistically low efficiency with DC and intermittent DC (9-13%) [48]. Overall, based on the literature review and evaluation, the efficiency of a water-splitting cell operating at a given power is highest for DC, and deviation from DC will mainly cause an increase in cell power and gas flow rate against a decrease in efficiency.

Shimizu et al. conducted extensive studies to determine the characteristics of DC water splitting complemented with ultrashort voltage pulses [49]. In their study, the authors used pulses with a bandwidth of about 300 ns under a DC power supply to the cell. The frequency of the applied pulses ranged from 2 kHz to 25 kHz.

Further results on voltage pulse water splitting technology and alternating current behaviour of the cell [50]:

- Bockris and Potter first observed the discharge phenomenon of electric double-layer capacitance after voltage interruption [51].
- Tseung and Vassie recorded an increase in amperage of 2 to 6 times compared to the DC voltage test [52].
- Viswanathan, et al. published a numerical solution for the current flow in a variable electric potential space in a water-splitting cell [53]. It was shown that even if the amperage reaches a higher value than in the DC case, the intensity of hydrogen production cannot be higher.
- Ibl modelled the material flow and capacitive effects during pulsed electroplating [54].
- Brandon and Kelsall have shown that the bubbles produced leave the electrode surface immediately after the voltage or amperage is interrupted [55].
- Khosla, et al. have measured that the size of the bubbles can be well controlled by the bandwidth of the applied pulses [56].
- Vanags, et al. have outlined the mechanism of hydrogen formation during inductive voltage pulses, showing that their method of using wolfram electrodes is more efficient than platinum [57].
- Kaveh, et al. measured an increase in conductivity of up to 50% for *pulse-width modulation* excitation with a 50% fill factor compared to DC testing [58].
- Mazloomi and Sulaiman found that excitation with *pulse-width modulation* signals at different voltage levels and fill factors resulted in higher efficiency at lower voltages and lower fill factors [59].
- Martiningsih, et al. discovered a nonlinear relationship between the *pulse-width modulation* filling factor and the intensity of hydrogen production [60].

Dobos investigated the evolution of a water-splitting cell's hydrogen production and energetic characteristics using sinusoidally alternating voltage with different frequencies and offset values. He found the evolution of the volumetric flow rate of hydrogen gas produced and the power consumption of the cell as a function of the frequency, amplitude and offset of the applied alternating voltage. [61]

## 2.4. Biogas components

The main constituents of biogases are methane and carbon dioxide due to microbiological processes. There is no higher hydrocarbon content at all. The biggest technological problem in the biogas plants is the foaming of the digesters. This undesired process is in a strong connection to the gas formation too. [62]. This kind of technological problems can be solved mainly by adequate stirring [63], [64], and sometimes the more precise preparation of the input material (e.g. right size chopping) can help to avoid the inconveniences [65]. Anyway, the chips-size of the materials used for energetic purpose is very much determines the process and its efficiency [66].

In general, biogases are composed of 45-75 mol% CH<sub>4</sub> and 25-55 mol% inert components (CO<sub>2</sub>, N<sub>2</sub>), which due to their non-combustible nature, significantly reduce the combustion parameters such as lower heating value, upper heating value, lower and upper Wobbe coefficient [67], [68].

As a result of these properties, biogases are purified, which enriches the biogas in methane, reducing its inert content and removing unwanted components. The degree of purification depends on the intended use [69].

Main components of biogases:

The main components of biogases are also found in natural gas, which are:

- methane (CH<sub>4</sub>)
- carbon dioxide (CO<sub>2</sub>)

- oxygen (O<sub>2</sub>)
- hydrogen (H<sub>2</sub>)
- nitrogen (N<sub>2</sub>)
- water vapour (H<sub>2</sub>O)

Co-components of biogases:

- hydrogen sulphide (H<sub>2</sub>S) and elemental sulphur (S)

It can be present in significant amounts (10 000 mg/m<sup>3</sup>) in the gases produced during fermentation processes. It causes corrosion in metals and SO<sub>2</sub> emissions when burnt. Hydrogen sulphide reacts with the water vapour content of the combustion products to form sulphuric acid (H<sub>2</sub>SO<sub>3</sub>), an effect further enhanced by organic sulphur compounds, as sulphur dioxide is also formed when sulphur is burnt. It must be separated from the biogas composition in each case.

- carbon monoxide (CO)

All types of biogas can contain this flammable, highly toxic gas in quantities of 10 mg/m<sup>3</sup>. As a potent reducing agent, it reduces oxides of metals to elemental metals.

- Ammonium (NH<sub>3</sub>)

It can be found in all biogas types in varying amounts, up to 100 mg/m<sup>3</sup>. It worsens the ignition parameters and contributes to NO<sub>x</sub> emissions. It may cause corrosion of metals. To avoid this process, the water vapour content of the gas should be kept low.

- nitrous oxide (N<sub>2</sub>O)

Landfill gases contain tiny amounts of this non-toxic gas. It feeds combustion, and under the influence of heat, it breaks down into nitrogen molecules and oxygen atoms, so it has no meaning.

- sulphur dioxide (SO<sub>2</sub>)

Typically found in landfill gas in quantities of some amounts 10 mg/m<sup>3</sup>. Much higher amounts are produced during the combustion of the hydrogen sulphide content in biogases. SO<sub>2</sub> reacts with water to form sulphuric acid (H<sub>2</sub>SO<sub>3</sub>), and its effect should therefore be considered in combustion analyses.

- hydrogen cyanide (HCN)

Highly toxic hydrogen cyanide is found only in landfill gases and can be almost completely removed from the gas composition by the aqueous washing process.

Some components are specific to biogases. These include nitrogen oxides (NO<sub>x</sub>) or hydrogen chloride (HCl), typical landfill gases. All biogas compositions contain chlorine- and fluorine-containing compounds, highly salt-forming elements (Cl-, F-) and can be found in biogases in quantities of up to 100 mg/m<sup>3</sup>. Their gases are toxic, combusting explosively with hydrogen and combining with metals to form halogenides. With the water vapour content of the combustion products, chlorine forms hypochlorous acid and fluorine forms hydrogen fluoride with hydrogen peroxide, which decomposes rapidly on heating [67].

The accompanying components of biogases:

In addition to the principal and co-components of biogases, nearly 200 additional accompanying components can be detected in each gas composition, which does not even represent 5 % of the total composition.

Siloxanes are mainly found in biogases from sewage treatment plants and landfills. They pose a hazard to movable components, as their combustion produces SiO<sub>2</sub>, which can lead to abrasion of rotating elements, changes in pipeline direction and constrictions. Research has shown that specific biogas cleaning processes can reduce siloxane amounts to as little as 0.3 mg/m<sup>3</sup>.

Halogenated hydrocarbons are mainly found in landfill gases. If burnt under inappropriate conditions, they can lead to dioxins and furans, which harm health.

The BTX compounds (benzene, toluene, xylene) are flammable, toxic substances, mostly in depot gases. They damage mainly the PE piping of the distribution system operating at lower pressures. Volatile organic compounds are present in minimal quantities in landfill biogases.

There is no European regulation that guides the presence of mercury in biogas. It occurs mainly in landfill gases in deficient concentrations, which can cause corrosion of aluminium components. Experience has shown that a good-quality active carbon process can remove it from biogas. The industrial practice has set the value of mercury below 1.0 µg/m<sup>3</sup>, but the presence and concentration of mercury require further investigation.

More than 20 metals can be found in biogases, such as copper, cobalt, chromium, manganese, lead, arsenic or nickel, in amounts of several 10 mg/m<sup>3</sup>.

After biogas purification, organic microorganisms may remain in the biomethane, but their impact is not yet fully understood and is currently under research. However, current in-feed practice has not shown any problems that could be attributed to this. Gases from unconventional sources may contain aromatic hydrocarbons, which can damage PE piping, rubber and synthetic elements and are carcinogenic and involved in soot formation [67].

Landfill gases contain the highest levels of undesirable components and are the most expensive to purify [70].

### 2.5. Properties of gas mixtures

The literature review has shown that biogas mixtures present unstable combustion in different burners due to their low calorific value. Researchers prefer to enrich biogas with different fuel additives to reduce these instabilities. Yılmaz et al. investigated the performance of oxygen enrichment of biogas flame in a model gas turbine burner [71]. They found that the biogas flame became more stable under acoustic perturbation at 24% O<sub>2</sub> compared to air combustion. Zouagri et al. investigated the characterisation of biogas/syngas mixtures [72]. The study results showed that increasing the amount of CO<sub>2</sub> in the mixture causes a decrease in maximum temperature and NO<sub>x</sub> emissions. Skvorcinskiene et al. investigated the combustion of biogas from waste with low CH<sub>4</sub> content, enriched with syngas and oxygen in a vortex-assisted combustor [73]. Three vortex generators with different lamella angles (37°, 45°, 53°) were used in the experiment. The results showed that the vortex generator with a 45° blade angle produced the lowest CO emissions. Striugas et al. investigated the combustion instability of a mixture of syngas and oxygenated biogas [74]. They showed that adding oxygen and syngas increased the OH\*, CH\* and C<sub>2</sub>\* chemiluminescence and flame stability.

Wang and colleagues investigated how adding propane and oxygen to biogas affects combustion instability [75]. The results showed that oxygen enrichment increased the explosion pressure of the flame. In cases where the oxygen content of the oxidiser was between 25% and 29%, the addition of propane significantly reduced the flame spread rate. Boussetla and co-workers investigated the development of NO emission under premixed Moderate and Intensive Low Dilution (MILD) combustion conditions in biogas/hydrogen mixtures [76]. It was shown that the addition of N<sub>2</sub> for MILD combustion resulted in reduced flame temperatures. In addition, it was observed that an increase in the H<sub>2</sub> content of the fuel mixture made the NNH mechanism dominant in NO formation.

It can be observed that some studies in the literature have also investigated the addition of pure hydrogen to fuels in gas turbine burners. Arenillas et al. investigated the effect of hydrogen addition on the flame area of biogas [77]. The results showed that adding hydrogen increased the flame's stability and temperature. Wei and co-workers investigated the specific heat flux and CO and NO emissions of biogas/hydrogen flames [78]. They added 10% H<sub>2</sub> to a 75% CH<sub>4</sub> - 25% CO<sub>2</sub> mixture and investigated different equivalence ratios. Arenillas et al. investigated the combustion of biogas/hydrogen mixtures [77]. As the biogas mixture was tested at three different methane ratios (70%, 60%, 50%), the H<sub>2</sub> ratio was varied between 5 and 25%. The results showed that stable combustion did not occur when the proportion of CO<sub>2</sub> in the biogas was above 40%. Yılmaz et al. investigated H<sub>2</sub>/CH<sub>4</sub>/CO<sub>2</sub> mixtures in their study [79]. The proportion of hydrogen in all mixtures was kept high and varied between 50% and 70%. The results showed that the thermal NO<sub>x</sub> mechanism was not dominant. In addition, the fuel mixture containing 50% H<sub>2</sub> caused 30 times more NO emissions than the mixture containing 70% of H<sub>2</sub>.

From the literature review, it becomes evident that investigating combustion instability and emission behaviour of biogas mixtures is an important topic. These studies have identified the positive effects of hydrogen addition and oxygen enrichment on reducing combustion instability. Considering these studies, it can be seen that the effects of simultaneous enrichment with hydrogen and oxygen, especially in premixed combustion, have not been investigated in the literature. In addition, while the literature has investigated the variation of temperature, emission, flame profile and laminar combustion velocity change data in studies to determine combustion instability, no research has been observed to investigate thermoacoustic instabilities with simultaneous enrichment with hydrogen and oxygen in biogas flame. Determination of dynamic instabilities is a method used in combustion studies due to the flame-distorting effect of external acoustic perturbations.

## 2.6. Effect of hydrogen mixing on the combustion characteristics of biogas

Biogas has an advantage over other renewable fuels, such as synthesis gas (produced from biomass and municipal solid waste gasification), in that it is produced directly from wet organic waste sources with minimal pre-processing [80]. However, the calorific value of biogas is low, e.g. at 1 bar pressure and 298 K, the calorific value of biogas (60% CH<sub>4</sub> - 40% CO<sub>2</sub>) is around 30 MJ/kg, compared to natural gas (50 MJ/kg) and hydrogen (120.971 MJ/kg). The lower calorific value of biogas is due to the high percentage of carbon dioxide present in the mixture (20-60% (v/v)), depending on the source and the digestion process used to produce it [81], [82].

Although the presence of carbon dioxide in biogas reduces pollutant emissions, it has a negative impact on the overall combustion characteristics of biogas [83], [84].

Carbon dioxide in biogas leads to a narrow range of flammability marginal values, reduced laminar flame velocity and lower flame temperatures than other commonly used fuels [85], [86].

The other major problem that arises from the high CO<sub>2</sub> content in biogas is the lower reactivity, which leads to flame suppression in cases where biogas is used as fuel in industrial burners. Several researchers have sought to understand the flame stabilisation behaviour of biogas at different equivalence ratios [87]. These studies show that carbon dioxide's thermal and chemical properties lead to lower reactivity, which limits the practical use of biogas in burners. For this reason, using pure biogas as a fuel for compression engines or gas turbines is limited due to its low laminar combustion rate and its flame, which tends to extinguish and hinder stable operation [88], [89].

The use of pure biogas in internal combustion engines and gas turbines is severely limited due to the poor combustion properties mentioned above [90]. The combustion properties of biogas can be improved by adding fuels with higher reactivity, thus converting low calorific value raw/pure biogas into high-quality fuel.

Application of laboratory simulation methods can result moderated biogas reactor processes, and the number of the malfunctions of an existing system can be reduced. The specific gas production can be optimised. According to this the electric capacity value can grow by 10-15 % [62].

One proposed solution is to add a high-reactivity fuel (e.g. hydrogen) to the biogas to improve reactivity with minimal changes in pollutant emissions. The primary combustion characteristics of premixed flames are laminar flame velocity ( $S_u$ ), ignition delay and self-ignition in premixed combustion. Two other crucial criteria for fuel selection are the adiabatic flame temperature ( $T_{ad}$ ) and the combustibility limits. Adding hydrogen to hydrocarbons improves these combustion characteristics [91]. The reason for this is that the hydrogen has several favourable combustion properties (high reactivity and heat release rate, high extinction velocity and laminar flame velocity, low ignition delay and wide flammability limit), which are suitable for making combustion processes more uniform [92], [93].

Adding hydrogen also increases the concentration of H- and OH-radicals, thus improving the overall reactivity of the mixture. It is also known that using 100% hydrogen in internal combustion engines presents several storage and safety problems [94]. To take advantage and overcome clean hydrogen problems, several researchers have proposed replacing the fractions of hydrocarbon fuels such as methane Karim et al., and El-Ghafoure et al., liquefied petroleum gas, Kishore et al., n-butane, Tang et al., n-decan (CH<sub>3</sub>(CH<sub>2</sub>)<sub>8</sub>CH<sub>3</sub>), Yu et al., etc. with hydrogen in the mixture [95], [96], [92], [97], [98]. Ali and Varunkumar presented the combustion process of different fuel mixtures with and without hydrogen for non-premixed flames, emphasising the flame formation process. [99]. An essential element in investigating these processes is examining the extinction transformation rate ( $ag$ ). The extinction transformation rate ( $ag$ ) is defined as the component of the velocity gradient perpendicular to the flame surface at the time of extinction. Like the laminar flame velocity ( $S_u$ ) of premixed flames, the extinction transformation rate ( $ag$ ) is an essential characteristic of non-premixed flames. The results show that the extinction transformation rate ( $ag$ ) increases by 2-2.5 times for CO<sub>2</sub> dilution and by 2.6-3.8 times for N<sub>2</sub> dilution, while the amount of CO increases by 10 vol% in fuel mixtures with H<sub>2</sub> increased by 5%. The higher CO % in the fuel results in higher flame temperatures, which increases the overall reactivity of the fuel, leading to an increase in  $ag$  values.

In the case of a premixed flame, laminar flame velocity, self-ignition and ignition delay are used to give the combustion characteristics of any given fuel-oxidiser combination. These characteristics provide essential information on the reactivity and exothermicity of a given fuel-oxidiser mixture. It also provides essential information on the diffusion and reactive properties of the mixture. Comparison of experimentally obtained

laminar flame speed ( $S_u$ ), ignition delay and self-ignition values with calculated values provides helpful information on validation, reduction and optimisation mechanisms [98], [100].

### 3. Conclusion

Investigating the combustion characteristics of alternative renewable fuels and their use in existing combustion systems has recently received considerable attention worldwide. This is due to the increasing demand for energy used for electricity production, heating or powering households, fuelling vehicles and manufacturing processes. Among synthetically produced renewable fuels, biogas is one of the promising substitutes, as it has lower processing costs and a slightly higher density than natural gas.

Our research work in the field of local, renewable and sustainable energy production, storage and use is focused on the development of an integrated solution that enables the production of hydrogen gas ( $H_2$ ) and oxygen gas ( $O_2$ ) by water decomposition ( $H_2O$ ) using photovoltaic (PV) solar cells and the production of biogas by biomass utilisation in an innovative process, thus achieving the production of compact devices of different sizes (scalable). The aim is to transform solar energy into combustible gas stored in a container.

The advantage of the system is that the biogas-hydrogen mixture it produces can be stored, and the intensity, period and interval of its use can be planned as required. It can be reused to generate electricity, heat or mechanical energy using a gas engine, gas engine-electric generator, gas boiler or gas burner.

### Acknowledgement

The project is implemented with the support of the call for tenders for Incentives of Corporate Research, Development, and Innovation Activities (GINOP\_PLUSZ-2.1.1-21) announced within the framework of the Széchenyi Terv Plusz program („Széchenyi” Plan Plus Programme), within the framework of the Economic Development and Innovation Operational Programme Plus (GINOP Plusz). Thank you for the financial support. The title of the project: "Scalable Cogeneration Solution by Integrating Solar Energy and Biomass Utilization". Project id. number: GINOP\_PLUSZ-2.1.1-21-2022-00165.

### References

- [1] **Hajdú J., Magó L.** (2006) The Possibilities of Use of the Biomass in Hungary, Proceedings of the 34<sup>th</sup> International Symposium “Actual Tasks on Agricultural Engineering”, Opatija, Croatia, 21-24. February 2006. Proc. p. 111-120.
- [2] **Hajdú J., Magó L.** (2007) Hazai biomotorhajtóanyag-előállítás hatása a mezőgazdasági termelésre MTA-AMB XXXI. Tematikus Kutatási és Fejlesztési Tanácskozás, Gödöllő, 2007. január 23., Vol. 1., p. 87-91.
- [3] **Magó L., Hajdú J., Fenyvesi L.** (2010) Megújuló energia a mezőgazdaságból, *Mezőgazdasági Technika, tudományos, műszaki fejlesztési és kereskedelmi folyóirat*, Vol. LI, No 1. különszám, p. 43-45. & 75.
- [4] **Magó L., Ježič V., Hajdú J., Poje T., Fenyvesi L.** (2009) Determination of Solid Biomass Potential from Agriculture in Hungary and Slovenia, Abstracts and Full Papers of the 31<sup>st</sup> International Conference of CIGR Section IV. “Rational Use of Energy in Agriculture and Economical Use of the Renewable Sources in Connection with Environmental Protection”, Gödöllő, Hungary, 31. August - 3. September 2009. p. 113.
- [5] **Magó L., Hajdú J., Fenyvesi L.** (2010) Survey of Biomass Energy Potentials of Hungarian Agriculture, Proceedings of the 38<sup>th</sup> International Symposium “Actual Tasks on Agricultural Engineering”, Opatija, Croatia, 22-26. February 2010. Proc. p. 355-364.
- [6] **Topisirović G., Oljača S., Oljača V. M., Magó L.** (2011) Economical Background and Potential of Solid Biomass Production from Agriculture in Hungary and Serbia, Abstracts and Full Papers of the II. International Conference “Synergy in the Technical Development of Agriculture and Food Industry”, Gödöllő, Hungary, 9-15. October 2011. p. 82.
- [7] **Nemcsics Á.** (2001) A napelem és fejlesztési perspektívái - Akadémiai Kiadó ISBN 963 05 7821 2
- [8] **Sharma et al.** (2015) Solar Cells: In Research and Applications - A Review, *Materials Sciences and Applications*, 2015, 6, 1145-1155, <http://dx.doi.org/10.4236/msa.2015.612113>

- [9] **Farkas I.** (2003) Napenergia a mezőgazdaságban - Mezőgazda Kiadó, ISBN 9789639358911
- [10] **Guerra et al.** (2018) Operation and physics of photovoltaic solar cells: an overview, *Revista de Technologica*
- [11] **Barótfi I.** (1993) A napenergia hasznosítása. Energiafelhasználói Kézikönyv, Környezettechnikai Szolgáltató Kft., ISBN 963 02 9535 0.
- [12] **Seres et al.** (2009) Comparison of PV modules under different spectral conditions, *Mechanical Engineering Letters*, 2009, Vol 3, pp 81 – 89,
- [13] **Seres I.** (2010) Hálózatra kapcsolt fotovillamos rendszerek elméleti és kísérleti vizsgálata OTKA 69094 Final report,
- [14] **Pálffy M.** (2017) Napenergia fotovillamos energetikai hasznosítása, *Magyar Tudomány*, Vol. 178/5
- [15] **Kouro et al.** (2015) Grid-Connected Photovoltaic Systems: An Overview of Recent Research and Emerging PV Converter Technology, *IEEE Industrial Electronics Magazine*, DOI: 10.1109/MIE.2014.2376976
- [16] **Regello R.** (2012) Understanding Solar Inverters, TheSolarPlanner.com
- [17] **Véghely T.** (2020) Szigetüzemű napelemes rendszerek, EU Solar NyRt.
- [18] **Almazrouei A.** (2019) Solar Charge Controller, University of Evansville
- [19] **Vasugi, Jayaraman** (2014) Solar Charged Stand Alone Inverter, *Journal of Engineering Research and Applications*, ISSN: 2248-9622, Vol. 4, Issue 7, July 2014, pp.84-87
- [20] **Bhowmick et al.** (2021) Review on hybrid inverter, *International Journal of Engineering Research & Technology (IJERT)*, ISSN: 2278-0181, NCETER - 2021 Conference Proceedings
- [21] **Al-ktranee M., Bencs P.** (2020) Overview of the hybrid solar system, *Analecta Technika Szegedinensa*, Vol 14, No 1.
- [22] **Végyvári Zs.** (2014) A hibrid villamos energiaellátó rendszerek vezérlésének terepi megvalósítása, *Hadmérnök*, XI. évf. 4.szám
- [23] **Beleznai N.** (2018) Kombinált napkollektoros, napelemes, hőszivattyús rendszerek, Wagner Solar Hungária Kft.
- [24] **Varga P.** (2020) Napenergia helyzetkép. 2020, XI. Napenergia hasznosítás és a jövő épületei szakmai nap
- [25] **Ghabour R., Korzenszky P.** (2022) Linear Model of DHW System Using Response Surface Method Approach, *Tehnicki Vjesnik-Technical Gazette*, Vol. 29:1 66-72. p.
- [26] **Géczi G., Korzenszky P., Bense L.** (2013) Ideális körülmények a levegő-víz hőszivattyú uszodatechnikai alkalmazása során, *Magyar Épületgépészet*, Vol. 62: 7-10. p.
- [27] **Géczi G., Bense L., Korzenszky P.** (2013) Water tempering of Pools Using Air to Water Heat Pump Environmental Friendly Solution, *Rocznik Ochrona Srodowiska*, Vol. 16: 115-128. p.
- [28] **Korzenszky P., Géczi G.** (2012) Heat pump application in food technology, *Journal of Microbiology and Food Sciences*, Vol. 2, 493-500. p.
- [29] **Tóth L., Slihte S., Ádám B. Petróczki K., Korzenszky P., Gergely Z.** (2011) Solar Assisted Ground Source Heat Pump System, *Hungarian Agricultural Engineering*, Vol. 23 57-61. p.
- [30] **Ramos, C.A.F., Alcaso, A.N. and Cardoso, A.J.M.** (2019) Photovoltaic-thermal (PVT) technology: Review and case study, *IOP Conf. Ser. Earth Environ. Sci.*, Vol. 354, No. 1,
- [31] **Shao, N., Ma, L. and Zhang, J.** (2019) Experimental study on electrical and thermal performance and heat transfer characteristic of PV/T roof in summer, *Appl. Therm. Eng.*, Vol. 162, No. June, p. 114276.
- [32] **Liang, R., Zhang, J., Ma, L. and Li, Y.** (2015) Performance evaluation of new type hybrid photovoltaic/thermal solar collector by experimental study, *Appl. Therm. Eng.*, Vol. 75, pp. 487–492.
- [33] **Duffie J. A., Beckman W. A.** (1974) Solar Energy Thermal Processes, Wiley - Interscience, New York
- [34] ASHRAE Standard 93-77: 1977
- [35] **Pierson P., Padet J.** (1990) Time constant of solar collectors. *Solar Energy*, 40 (2) 109-114. p.
- [36] **Rogers B. A.** (1980) Transient testing of collectors. *Proceedings UK-ISES conferences, solar energy codes of practice and test procedures*, London, 45-55. p.
- [37] **Hill J. E. et al.** (1977) Testing of solar collector according to ASHRAE Standard 93-77. *Proceedings of Annual Meeting of the American Section of ISES*, Orlando, Florida, vol 1. 6-19. p.

- [38] **De Ron A. J.** (1980) Dynamic modelling and verification of a flat-plate solar collector. *Solar Energy*, 24 117-128. p.
- [39] **Kammaing W.** (1985) The approximate temperatures within a flat-plate solar collector under transient conditions. *Int J Heat Mass Transfer*, 28 433-440. p.
- [40] **Prapas D. E. et al.** (1988) Response function for solar energy collectors. *Solar Energy*, 40 (4) 371-383. p.
- [41] **Kumar. R., Rosen, M.A.** (2011) Performance evaluation of a double pass PV/T solar air heater with and without fins, *Appl. Therm. Eng.*, Vol. 31, No. 8–9, pp. 1402-1410.
- [42] **Hossain, M.S., Pandey, A.K., Selvaraj, J., Abd Rahim, N., Rivai, A. and Tyagi, V.V.** (2019) Thermal performance analysis of parallel serpentine flow based photovoltaic/thermal (PV/T) system under composite climate of Malaysia, *Appl. Therm. Eng.*, Vol. 153, pp. 861-871.
- [43] **Háber I. E., Farkas I.** (2015) Micro heat-pipe rendszerű PV/T kollektorok vizsgálata. *Energiagazdálkodás*, 2015, 56. évf., 5-6. sz., 30-35. p.
- [44] **Mazloomi, K. & Sulaiman, N.** (2013) Retarding Forces Cancellation in Electrolyte Solutions-An Electrical Approach. *International Journal of Applied Electronics in Physics & Robotics*, 1(1).
- [45] **Naohiro Shimizu, S. H., Sekiya, T. & Oda, O.** (2006) A novel method of hydrogen generation by water electrolysis using an ultra-short-pulse power supply. *Journal of Applied Electrochemistry*, 36(4), pp. 419-423.
- [46] **Kleperis, J., Vanags, M. & Bajars, G.** (2012) Water Electrolysis with Inductive Voltage Pulses. In: V. Linkov & J. Kleperis, szerk. *Electrolysis*, pp. 19-44.
- [47] **Chellaiah, D.** (2012) Economical Hydrogen Production by Electrolysis Using Nano Pulsed DC. *International Journal of Energy and Environment*, 3(1), pp. 129-136.
- [48] **Mandal, B. et al.** (2012) Effects of Geometry of Electrodes and Pulsating DC Input on Water Splitting for Production of Hydrogen. *International Journal of Renewable Energy Research*, 2(1).
- [49] **Shimizu, N., Hotta, S., Sekiya, T. & Oda, O.** (2006) A novel method of hydrogen generation by water electrolysis using an ultra-short-pulse power supply. *Journal of Applied Electrochemistry*, 36. kötet, pp. 419-423.
- [50] **Rocha, F., Radiguès, Q. d., Thunis, G. & Proost, J.** (2021) Pulsed water electrolysis: A review. *Electrochimica Acta*, 377(1).
- [51] **Bockris, J. O. & Potter, a. E. C.** (1952) The Mechanism of the Cathodic Hydrogen Evolution Reaction. *Journal of The Electrochemical Society*, Vol. 99., p. 169.
- [52] **Tseung, A. and Vassie, P.** (1976) A study of gas evolution in teflon bonded porous electrodes—III. Performance of teflon bonded Pt black electrodes for H<sub>2</sub> evolution. *Electrochimica Acta*, 21(4), pp. 315-318.
- [53] **Viswanathan, K., Cheh, H. & Standart, G.** (1980) Electrolysis by intermittent potential. *Journal of Applied Electrochemistry*, 10(1), pp. 37-41.
- [54] **Ibl, N.** (1980) Some theoretical aspects of pulse electrolysis. *Surface Technology*, 10(2), pp. 81-104.
- [55] **Brandon, N. & Kelsall, G.** (1985): Growth kinetics of bubbles electrogenerated at microelectrodes. *Journal of Applied Electrochemistry*, 15(4), pp. 475-484.
- [56] **Khosla, N. K., Venkatachalam, S. & Somasundaran, P.** (1991) Pulsed electrogeneration of bubbles for electroflotation. *Journal of Applied Electrochemistry*, Vol. 21., p. 986–990.
- [57] **Vanags, M., Kleperis, J. & Bajars, G.** (2011) Electrolyses model development for metal/electrolyte interface: Testing with microrespiration sensors. *International Journal of Hydrogen Energy*, 36(1), pp. 1316-1320.
- [58] **Kaveh, M. e al.** (2013) Analysis of the frequency response of a water electrolysis cell. *International Journal of Electrochemical Science*, 8(3), pp. 3731-3739.
- [59] **Mazloomi, K., S. N., Ahmad, S. & Md Yunus, N.** (2013) Analysis of the Frequency Response of a Water Electrolysis cell. *International Journal of Electrochemical Science*, 8(3), pp. 3731 - 3739.
- [60] **Martiningsih, W. e al.** (2017) Effect of PWM signal on hydrogen production using Hoffman voltameter methods. *Journal of Computational and Theoretical Nanoscience*, 23(12), pp. 11897-11901.
- [61] **Dobos, Z.** (2016) A változó feszültség jellemzőinek hatása az elektrolitikus hidrogénelőállítás energiahatékonyságára (doktori értekezés). Miskolc: Miskolci Egyetem.

- [62] **Tóth L., Beke J., Bártfai Z., Szabó I., Hartdégén G., Oldal I., Blahunka Z.** (2014a): Technological Features of Biogas Plants Using Mixed Materials, *Hungarian Agricultural Engineering*, No 26/2014, p. 39-46., DOI:10.17676/HAE.2014.26.39
- [63] **Bártfai Z., Tóth L., Oldal I., Szabó I., Beke J., Schrempf N.** (2015a): Modelling the stirring process of biogas plants using mixed materials, *Hungarian Agricultural Engineering*, No 27/2015 p. 5-13., DOI: 10.17676/HAE.2015.27.5
- [64] **Bártfai Z., Oldal I., Tóth L., Szabó I., Beke J.** (2015b): Conditions of using propeller stirring in biogas reactors, *Hungarian Agricultural Engineering*, No 28/2015 p. 5-10., DOI: 10.17676/HAE.2015.28.5
- [65] **Bártfai Z., Blahunka Z., Bácskai I., Hartdégén G.** (2017): Biogázüzemben alkalmazott szilárdanyag-aprító berendezés kopási tulajdonságainak javítása, *Mezőgazdasági Technika*, No 5/2017. Spec Issue, p. 32-36.
- [66] **Tóth L., Koi Zs., Szabó I., Bártfai Z.** (2014b): Faaprítékok hőtechnikai felhasználása, *Mezőgazdasági Technika*, No10/ 2014, p. 2-5.
- [67] **Szunyog, I.** (2009) A biogázok földgáz közszolgáltatásban történő alkalmazásának minőségi feltételrendszere Magyarországon; PhD thesis, 2009. June
- [68] **Szunyog I., Galyas A. B.** (2018) Biogáz-előkészítés I., Teaching material. Miskolci Egyetem Gázmérnöki Intézeti Tanszék
- [69] **Hajdú, J.** (2009) Biogázüzemek működése és biogáz üzemi technológiák, OBEKK Zrt., Tudományos szakmai kiadványok sorozata (11/12), Szent István Egyetemi Kiadó, Gödöllő, 2009. ISBN 978-963-269-157-2
- [70] **Bai A.** (2009) A biogáz előállítás – a gazdálkodók szemével. *Őstermelő. Gazdálkodók Lapja*. Primom SZSZB megyei Vállalkozásélénkítő Alapítvány, Vállalkozói Központ., Nyíregyháza, 2009, No 3. (június-július), pp. 109-110
- [71] **Yilmaz I, Alabas, B, Tas, tan M, Tunç G.** (2020) Effect of oxygen enrichment on the flame stability and emissions during biogas combustion: An experimental study. *Fuel* 2020; 280:118703.
- [72] **Zouagri R, Mameri A, Tabet F, Hadeif A.** (2020) Characterisation of the combustion of the mixtures biogas-syngas at high strain rates. *Fuel* 2020; 271:117580.
- [73] **Skvorcinskiene R, Striugas N, Zakarauskas K, Paulauskas R.** (2021) Combustion of waste gas in a low-swirl burner under syngas and oxygen enrichment. *Fuel* 2021; 298: 120730.
- [74] **Striugas N, Zakarauskas K, Paulauskas R, Skvorcinskiene R.** (2020) Chemiluminescence based characterisation of tail biogas combustion stability under syngas and oxygen-enriched conditions. *Exp Therm Fluid Sci* 2020; 116:110133.
- [75] **Wang X, Zheng L, Wang J, Pan R, Yang W, Jin H, et al.** (2021) Effect of propane addition and oxygen enrichment on the flame characteristics of biogas. *Energy&Fuels* 2021; 35(6):5015–25.
- [76] **Boussetla S, Mameri A, Hadeif A.** (2021) NO emission from non-premixed MILD combustion of biogas-syngas mixtures in opposed jet configuration. *Int J Hydrogen Energy* 2021; 46(75):37641–55.
- [77] **Arenillas IA, Castells B, Llamas B, Bolonio D, Garcia-Martinez MJ, Lorenzo JL, et al.** (2021) Experimental Study of Biogas-Hydrogen Mixtures Combustion in Conventional Natural Gas Systems. *Appl Sci* 2021; 11(14):6513. app11146513.
- [78] **Wei Z, Liu Hu, Chen Z, Liu Z, Zhen H.** (2022) Quenching distance, wall heat flux and CO/ NO thermochemical states in the wall vicinity of laminar premixed biogas-hydrogen impinging flame. *Fuel* 2022; 307:121849.
- [79] **Yilmaz H, Yilmaz I.** (2021) Flame and instability characteristics of high hydrogen content gas mixtures. *Energy* 2021; 223:120084.
- [80] **Yadvika et al.** (2004) Enhancement of biogas production from solid substrates using different techniques - a review. In: *Bioresource Technology* 95 1–10 p.
- [81] **Yang L. et al.** (2014) Progress and perspectives in converting biogas to transportation fuels. In: *Renewable and Sustainable Energy Reviews* 40 1133–1152 p.
- [82] **Divya D., Gopinath L. R., Merlin Christy P.** (2015) A review on current aspects and diverse prospects for enhancing biogas production in sustainable means. In *Renewable and Sustainable Energy Reviews* 42 690–699 p.

- [83] **Charest M. R. J.** (2014) Numerical and experimental study of soot formation in laminar diffusion flames burning simulated biogas fuels at elevated pressures. In: *Combustion and Flame* 161 2678–2691 p.
- [84] **Fischer M., Jiang X.** (2015) An investigation of the chemical kinetics of biogas combustion. In: *Fuel* 150 711–720 p.
- [85] **Lee C., Hwang C.** (2007) An experimental study on the flame stability of LFG and LFG-mixed fuels. In: *Fuel* 86 649–655 p.
- [86] **Chao Y. et al.** (2004) Effects of dilution on blowout limits of turbulent jet flames. In: *Combustion Science and Technology* 176 1735-1753 p.
- [87] **Wilson D. A., Lyons K. M.** (2008) Effects of dilution and co-flow on the stability of lifted non-premixed biogas-like flames. In: *Fuel* 87 405–413 p.
- [88] **Porpatham E., Ramesh A., Nagalingam B.** (2013) Effect of swirl on the performance and combustion of a biogas fuelled spark ignition engine. In: *Energy Conversion and Management* 76 463–471 p.
- [89] **Porpatham E., Ramesh A., Nagalingam B.** (2007) Effect of hydrogen addition on the performance of a biogas fuelled spark ignition engine. In: *International Journal of Hydrogen Energy* 32 2057 – 2065 p.
- [90] **Zhen H.S. et al.** (2014) Characterisation of biogas-hydrogen premixed flames using Bunsen burner. In: *International Journal of Hydrogen Energy* 39 13292-13299 p.
- [91] **Wahab M. A. B. A.** (2009) Addition of hydrogen to gasoline-fuelled 4 stroke SI engine using 1-dimensional analysis. University BSc. thesis. Faculty of Mechanical Engineering University Malaysia Pahang
- [92] **Kishore V. R. et al.** (2008) Measurement of adiabatic burning velocity in natural gas-like mixtures. In: *Experimental Thermal and Fluid Science* 33 10–16 p.
- [93] **Paidi S. K. et al.** (2013) Effect of N<sub>2</sub>/CO<sub>2</sub> dilution on laminar burning velocity of H<sub>2</sub>-air mixtures at high temperatures. In: *International Journal of Hydrogen Energy* 38 13812-13821 p.
- [94] **Petkov T. et al.** (1988) An outlook of hydrogen as an automotive fuel. In: *International Journal of Hydrogen Energy* Vol. 14, No. 7, 449-474 p.
- [95] **Karim G. A. et al.** (1996) Methane-hydrogen mixtures as fuels. In: *International Journal of Hydrogen Energy* Vol. 21, No. 7. 625- 631 p.
- [96] **El-Ghafour S.A.A. et al.** (2010) Combustion characteristics of natural gas–hydrogen hybrid fuel turbulent diffusion flame. In: *International Journal of Hydrogen Energy* 35 2556–2565 p.
- [97] **Tang C. L., Huang Z. H., Law C. K.** (2011) Determination, correlation, and mechanistic interpretation of effects of hydrogen addition on laminar flame speeds of hydrocarbon–air mixtures. In: *Proceedings of the Combustion Institute* 33 921–928 p.
- [98] **Yu G., Law C. K., Wu C. K.** (1986) Laminar Flame Speeds of Hydrocarbon + Air Mixtures with Hydrogen Addition. In: *Combustion and Flame* 63 339-347 p.
- [99] **Ali S. M., Varunkumar S.** (2020) Effect of burner diameter and diluents on the extinction strain rate of syngas-air non-premixed Tsuji-type flames. In: *International Journal of Hydrogen Energy* 45 9113-9127 p.
- [100] **Ali S. M., Varunkumar S.** (2019) Preliminary results on syngas kinetic mechanism optimisation using the new opt-d\* algorithm. *Conference Paper 11th international conference on chemical kinetics.*

## **MATHEMATICAL MODELLING AND EXPERIMENTATION OF SOY WAX 68°C ENCAPSULATED INTO SOLAR TANK (CASE STUDY)**

**Author(s):**R. Ghabour<sup>1</sup>, Y. Amer<sup>2</sup>, P. Korzenszky<sup>2</sup>**Affiliation:**<sup>1</sup> Doctoral School of Mechanical Engineering – Hungarian University of Agriculture and Life Sciences, 2100 Gödöllő, Páter Károly u. 1., Hungary;<sup>2</sup> Institute of Technology - Hungarian University of Agriculture and Life Sciences, 2100 Gödöllő, Páter Károly u. 1., Hungary.**Email address:**

ghabour.rajab@phd.uni-mate.hu; amer.yacoub.5293@gmail.com; korzenszky.peter.emod@uni-mate.hu

**Abstract:** Governments worldwide are attempting to minimise CO<sub>2</sub> emissions, and solar energy storage remains the most difficult problem to tackle in the current climate. Typically, domestic hot water is mainly used for heat process services in colder climates when the tank loss is significant. Any design modification can result in a higher solar yield. Since water is a perfect medium for heat storage, this article will examine different Solar Domestic Hot Water (SDHW) systems in cold climates such as Central Europe and hot and dry climates such as the Middle East (Syria). Linear modelling was conducted using R script software using coded values to define the optimal value using the response surface method (RSM). The programming phase uses the least-squares approach to provide a general rationale for the line's best-match position among the data points under consideration. For each variable, the coded values range from [-1, +1]. The number of experiments is determined by the formula  $2^k$ , where  $k$  is the variable number. Since each variable has two possible values [-1, +1], the total number of experiments was  $2^3 = 8$ . In addition to these experiments, we performed one more experiment for defining second-degree non-linear coefficients. The second-degree factors were checked to evaluate the non-linearity of the system. The experimental work was done in the laboratory; an insulated water tank filled with 5 litres of water was used. A capsulated PCM soy wax 68°C test was conducted. For the charging phase, the response surface approach with non-linear correlation was used to determine the optimal number of samples and PCM quantity at two temperature levels. The results of temperature, sample numbers, and wax quantity demonstrate a 0.22, 2.3, and -1.12 first-degree magnitude effect, respectively. In addition, each two-factor interaction contour plot is depicted.

**Keywords:** solar tank; PCM material; thermal storage; linear modelling; R-script

### **1. Introduction**

The rapid expansion and technological revolution of human civilisation in the last few decades has brought with it unavoidable consequences like over-exploitation of the environment and natural resources. All of this compelled the researchers to seek out a more long-term answer while still optimising the existing ones. While fossil fuels are currently the dominant energy source, resulting in large carbon dioxide emissions, environmentally friendly alternatives, such as renewable energy systems, have begun to emerge with extended life spans, high reliability, and efficiency [1, 2]. Those systems became a viable alternative to the previous ones. Renewable energy is being used not only because of CO<sub>2</sub> emissions from traditional fuels and because it is environmentally benign but also because of rising energy demand and fluctuating oil prices.

Renewable technologies can supply consistent, self-sufficient electricity to remote places. For example, the willingness to support new renewable energy projects grew in Hungary since it proved to be a good financial investment with a payback period of less than ten years [3, 4]. It became evident that using renewable energy sources is the best approach to comply with the Kyoto Protocol. According to data given by ESTIF (European Solar Thermal Industry Organisation) [5], solar heating and cooling have proven to be a driver even in

adverse economic times, with a solar power output of 26.3 [GWth] and a surface area of more than 37 million square meters.

Water heating accounts for about 15% of total energy use in cold locations (such as Budapest). Furthermore, many applications demand temperatures of less than 100 degrees Celsius, which can be easily achieved using renewable energy, such as solar domestic water heating (SDWH) technology [6, 7]. Traditional water heating systems that use fossil fuels or electric heaters have a greenhouse effect, require a lot of maintenance, and are costly. As a result, the future of solar water heating system technology seems bright because of its environmentally benign nature and use of renewable energy [8, 9].

SDWH can be broken down into two sections: design and operation. The collectors can be made in a variety of ways. Solar collectors are divided into flat plate collectors (FPC) and evacuated tube collectors (ETC). In evacuated tube collectors, temperatures can reach 250 degrees Celsius, and efficiency can reach 80%. However, these changes depend on the weather, the design, and the load profile [10].

Some studies model the internal temperature conditions of an outdoor container based on measured meteorological data. This model can be used to predict the internal temperature of an office container, thereby reducing unnecessary environmental impact. [11, 12]

Other authors have validated a mathematical model with measured data from a real solar heating system. The error of the system model they developed is 3.4%. Similar modelling can be of great help in improving energy efficiency. [13]

The latent heat storage material is another technique to include the PCM. They are most typically employed in the solar system as a cooling solution for PV panels, which boosts their efficiency because the chemical bonds of the material break when it changes its phase. Thermal collectors can also be utilised as a storage material [14] to boost the solar system's energy capacity. One of the major advantages of integrated PCMs in solar systems is that they are simple to install and have no complicated components [3]. In addition to a high storage density [15]. As a result, any research in this field can potentially improve the tank's efficiency while reducing its size [16].

Energy is typically stored and retrieved as sensible heat, latent heat, or a thermo-chemical reaction, all of which are accomplished through a change in the medium's internal power. Sensible heat storage (SHS) stores heat by raising the temperature of the medium. When the storage medium changes phase from solid to liquid, liquid to gas, or vice versa, latent heat storage (LHS) uses the absorbed/released heat. The PCM is a heat-absorbing latent storage medium that maintains an almost constant temperature. This process will continue until the entire PCM has been transported to the liquid phase. The PCM begins to harden as the ambient temperature drops, releasing the accumulated latent heat. Melting temperatures typically vary from -50 to 1900 degrees Celsius. [17]

Some PCMs are highly beneficial within the human comfort zone (20-300°C), allowing 5 to 14 times higher heat density storage than traditional storage mediums like water or rocks [12–14]. Using a response surface method RSM, the numerical model of the entire system is used to select appropriate operational parameters and optimise the stored energy. The solar system's storage system is a crucial component and element. Furthermore, in order to maximise solar production, storage density (the amount of energy stored per volume or mass), appliance efficiency (solar collectors, tanks, and so on), and demand consumption [18], are critical aspects in determining the storage tank's capability for PCM [19]. Due to the irregular nature of solar energy, this could be effective in meeting energy demand. Whereas several simulation attempts have been carried out to determine the performance of water storage tanks with PCM [20], there are no references to model the optimisation of the working variables [16], because it causes  $2^k$  experiments to run, where  $k$  is the number of factors.

## **2. Materials and Methods**

We performed mathematical modelling using the response surface method and experimented with the soybean wax PCM integrated into the solar tank in the laboratory. A capsulated PCM soy wax 68°C in a 5-litre insulated water tank was conducted. The response surface approach with non-linear correlation was used for the charging phase to determine the appropriate number of samples and the quantity of PCM at two temperature levels. The method will illustrate the first-degree effect of the temperature, sample numbers, and wax quantity. Furthermore, each two-factor interaction contour plot is depicted.

The experiment components are as follows: water tank, heater, sensors, datalogger (ALMEMO 2890-9), and Wax 68°C type. The system comprises a well-insulated water tank covered by 5 cm of expanded

polystyrene (EPS), an oil-based insulation material that acts as a perfect insulator in the form of foam. This foam is a non-degradable, environmentally friendly material that maintains its qualities throughout time.

The tank has dimensions of 42x13x16 cm and can hold up to 8.7 litres of water, as shown in Figure 1; however, it was only filled with 5 litres during the measurement, and the remaining amount was for the specimen tray. As illustrated in Figure 1, the tray comprises 7x3 specimens, each of which may hold 50 mL of the allocated material.

The heater is turned on to a certain required temperature ranging between (-20 – 100) °C once the specimen tray is fixed inside the tank and filled with the assigned material. The by-pass line helps to better mix the water throughout the heating process, resulting in temperature uniformity in the tank. Meanwhile, the data logger (Almemo 2890-9) with nine input channels, as shown in Figure 2, stores the information from the sensors. A data logger is a device that measures and displays signal voltages plotted with time or another signal voltage. Until the user stops the data recorder, it measures in a continuous stream mode, every time new samples are taken during the measurement, they are transferred straight to the computer, where they are processed, displayed, and, if desired, stored on disk. The presence of a change in an input signal is immediately apparent.

Two temperature sensors, NiCr-Ni type k (-40 → 1000°C), are located on the right and left sides of the tank, as well as one ambient temperature sensor used as a reference temperature to determine when the container cools down to near ambient temperature, and another sensor inside the PCM capsule, as well as two heat flux sensors in the internal and external parts of the insulation. Finally, the goal is to calculate the time required for each experiment in which the water cools down to near ambient temperature after being heated, which is represented by the equation:

$$T_{\text{avg\_tank}} - T_{\text{amb}} \leq +1 \text{ } ^\circ\text{C}$$

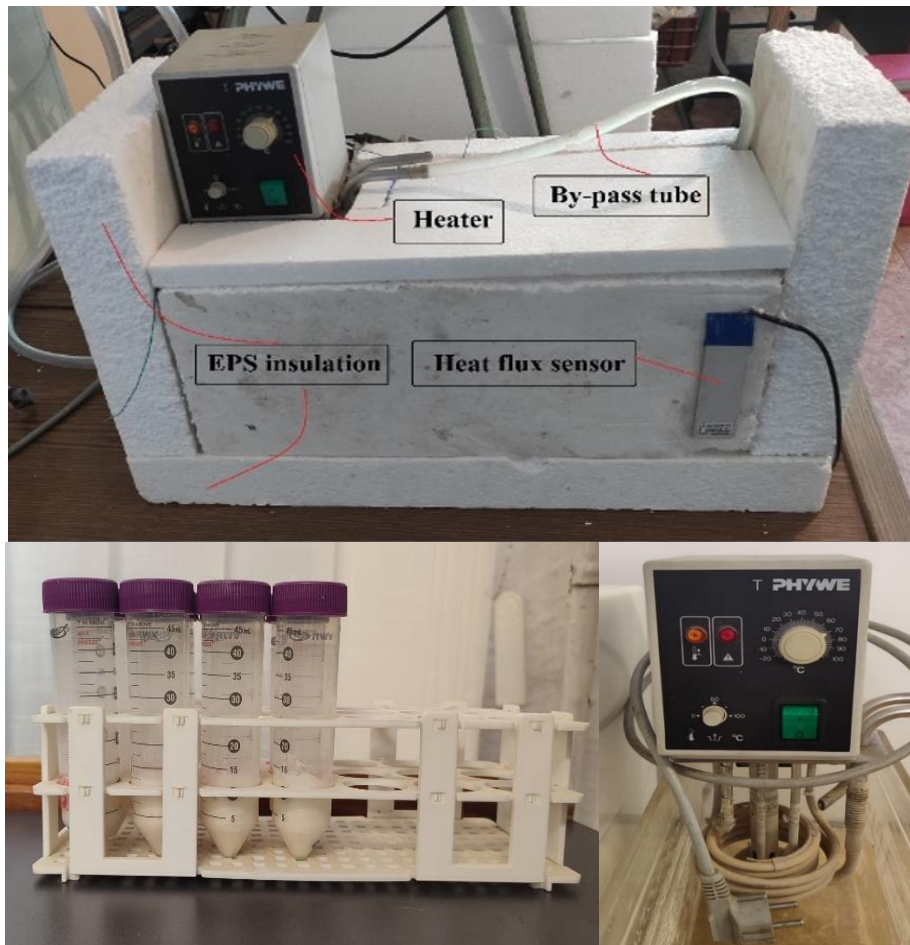


Figure 1. Experiment components



Figure 2. ALMEMO 2890-9 type data logger

The model was built using the R programming language, with coded values ranging from [-1, +1] for each variable, and the variables being "S" for Sample numbers, with the code (-1) for four samples and (+1) for eight samples. The quantity of PCM in each sample is denoted by the letter "Q," where (-1) code equals 5g and (+1) code equals 10g. Finally, the temperature is represented by the letter "T," with code (-1) denoting 45°C and code (+1) denoting 75°C. As seen in Figure , this results in a cube pattern, with each corner representing a set of these three variables, resulting in a single experiment. As indicated in Table 1, the number of experiments is determined using the form  $2^k$ , where k is the number of variables; therefore, 23 results in eight measurements. To detect the second-degree non-linear coefficients, additional measurement was undertaken out of the cube borders at (S=6, Q=7.5g, T=60°C) to add to the fact that the correlation was known before commencing the measurement.

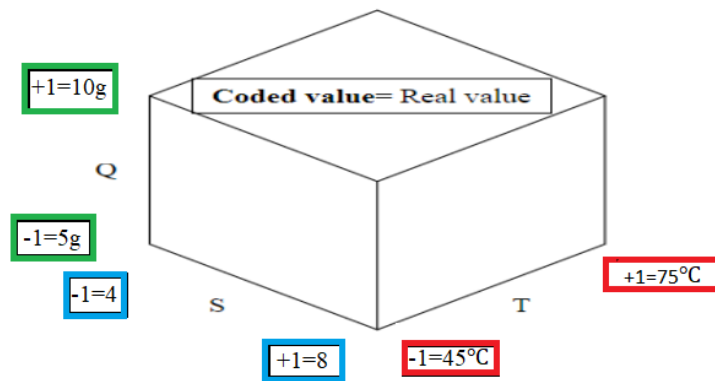


Figure 3. Experiment data set cube

The relationship between coded values and real values is shown by the following equation:

$$\text{Coded value} = \frac{\text{Real value} - \text{Center point}}{\frac{1}{2}(\text{range})}$$

Table 1. Experiment parameters

	1	2	3	4	5	6	7	8	9_extra_pre
Samples [-]	-1	+1	-1	+1	-1	+1	-1	+1	0
Quantity [g]	-1	-1	+1	+1	-1	-1	+1	+1	0
Temperature [°C]	-1	-1	-1	-1	+1	+1	+1	+1	0

The method used is the least-squares method, which was developed by Carl Friedrich Gauss in 1795 and offered the overarching justification for the best-fit line placement among the data points. Iterations are used to solve the non-linear model in our experiment. The following coded equation represents the created model:

$$Y_i = \beta_0 + \beta_1 X_{1i} + \beta_2 X_{2i} + u_i, i = 1, \dots, n$$

Where:

- $X_1, X_2$  are the two independent variables (regressors)
- $(Y_i, X_{1i}, X_{2i})$  denote the  $i^{\text{th}}$  observation on  $Y, X_1,$  and  $X_2$ .
- $\beta_0$  = unknown population intercept
- $\beta_1$  = effect on  $Y$  of a change in  $X_1$ , holding  $X_2$  constant
- $\beta_2$  = effect on  $Y$  of a change in  $X_2$ , holding  $X_1$  constant
- $u_i$  = “error term” (omitted factors)

### 3. Results

In our experiment, the non-linear model is solved using iterations. The following coded equation represents the generated model:

$$y = 16.09 + 2.3S - 1.12Q + 0.2T - 1.3Q * S + 0.57S * T + 2.1Q * T + 0.2Q * S * T$$

To understand the relationship between the factors and the objective, a Pareto plot is conducted as in Figure 4.

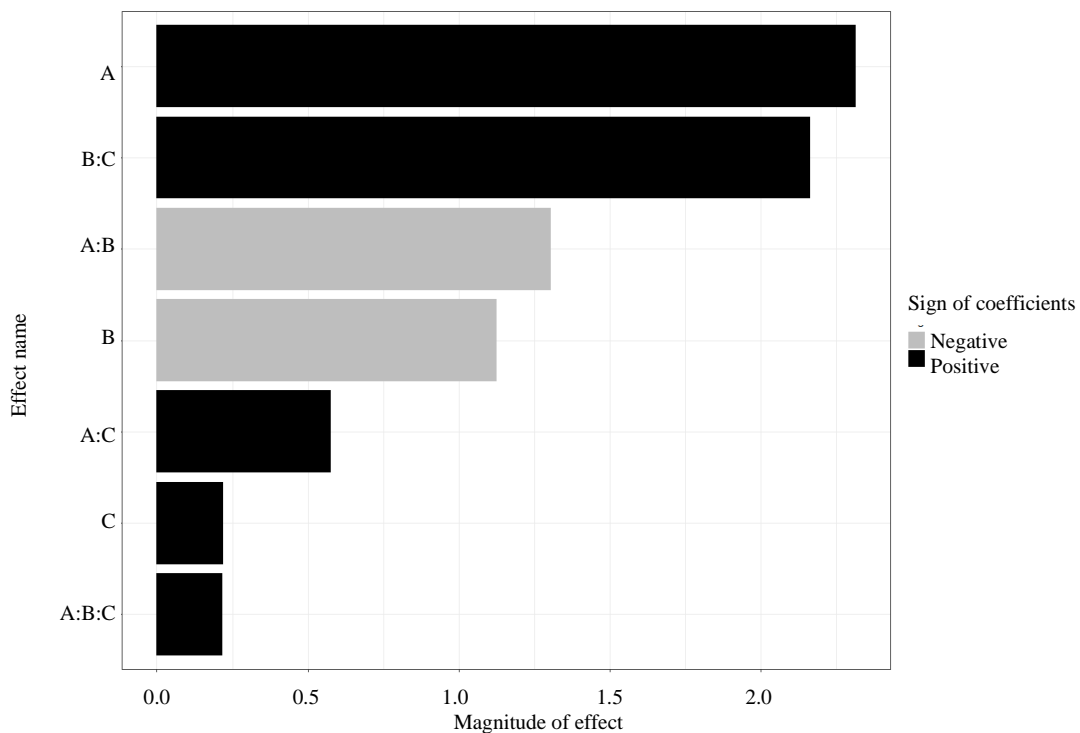


Figure 4. General model Pareto plot

A: Sample of number [-], B: Quantity [g], C: Temperature [°C]

The magnitude of each parameter is easily observed using the Pareto plot, while the sample numbers (A) and temperature with the quantity (BC) both have the biggest positive magnitude. In the third and fourth places, contrariwise, the sample with quantity both (AB) and the quantity coefficient (B) have a negative magnitude. In the end, the sample numbers with temperature (AC) have a low positive magnitude, adding to the fact that the 3-factor interaction S\*Q\*T (ABC) or any three-factor interactions do not exist in nature, but as it is shown in the Pareto plot Figure 4, it has almost zero magnitude. This is similar to temperature, which has a low influence. On the other hand, the contour plot of each two-factor interaction shows the curves where the overall result can be better, as seen in Figure 5.

Paying attention to some coded values that may have no meaning on the chart, for instance,  $S(A) = 0$  or  $Q(B) = 0$  matches 0 samples and 0 g, so below 3 values in the chart have no meaning in real-world values. As we can see in the chart, to increase the time, we should increase the temperature and the PCM quantity, as in the referring arrow. On the other hand, the coefficients of S, Q, and T in the equation show the plot's direction. In other words, a coded value of  $\Delta T \rightarrow [+1]$  will add 0.2 hours to the overall result. Similarly,  $\Delta Q \rightarrow [+1]$  will add -1.12 hours, and  $\Delta S \rightarrow [+1]$  adds 2.3 hours, as in Figure 5.

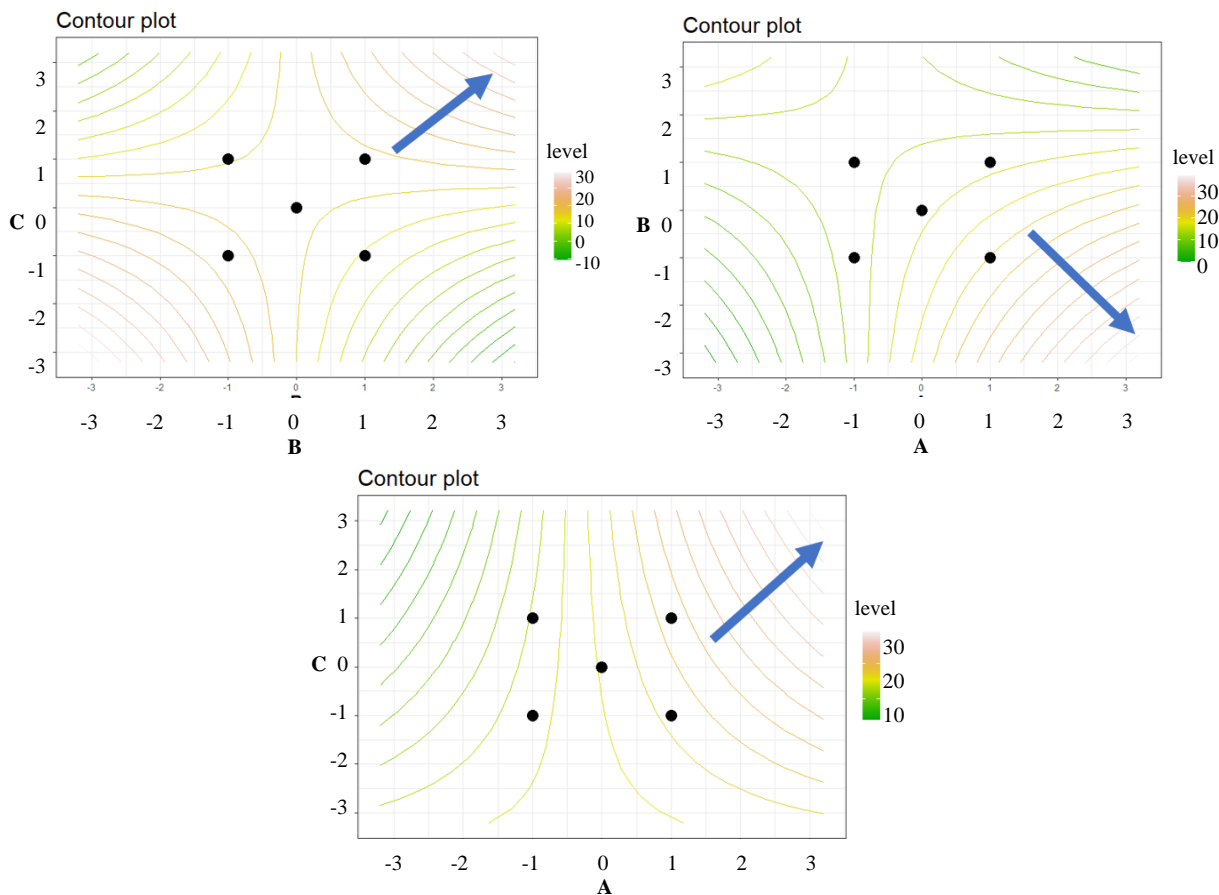


Figure 5. The two-factors interactions

On the other hand, the S\*Q (AB) interaction shows better results (as shown in the5), we see for the efficiency B (quantity) is negative, and A (sample number) is positive. That means when the sample number increases, the time will be longer, and when the quantity decreases, the time will be longer. The black dots in the graph represent the 4 corners of the cube from a 2D Q\*T perspective, adding to one pre and post experiments that were needed to identify the second-order coefficients. From the double-factor contour plot, the time increases if both factors are positive individually. That means both the sample number and the temperature should be increased to get the highest time.

By conducting eight trials to optimise the performance in a specific thermal tank, a matrix set of three variables was studied: temperature, quantity, and sample number of Soy wax. The mathematical first-degree, non-linear, 3-factors interaction equation was created using an R script based on the data. Furthermore, one

extra experiment was to determine non-linear coefficients. Also, a Pareto Plot depicts the most influential elements in the non-linear equation, with sample numbers having the most significant magnitude, followed by temperature and PCM amount. The quantity has the strongest negative magnitude, indicating non-linearity. The results can be seen in Table 2.

Table 2. Experiment parameters

	1	2	3	4	5	6	7	8	9_extra_pre
<b>Samples [S]</b>	5	10	5	10	5	10	5	10	7.5
<b>Quantity[Q]</b>	4	4	8	8	4	4	8	8	6
<b>Temperature[T]</b>	45	45	45	45	75	75	75	75	60
<b>y [hour]</b>	16.3	11.43	12.5	12.56	11.43	19.38	15.68	19.28	15.03

#### 4. Conclusions

Using domestic hot water can improve competitiveness and lead to environmental savings and economic advancement, especially in developing countries where solar energy is usually available and abundant. The predesigned solar hybrid systems have many advantages to be used nowadays, especially in developed countries where solar irradiation is usually sufficient. A big portion of energy is used in domestic hot water and industries and can be covered partially or totally with renewable energies such as solar energy. In practice, experimental work has been done in the lab where an insulated water tank filled with 5 litres of water and encapsulated PCM soy wax 68°C. Three parameters were applied: temperature, quantity, and sample number of Soy wax. This type of wax has not been tested before to see if it can be used in the solar system to prolong energy retention for a longer period. Especially when used in Hungary, where the heat loss is large. This article aims to study the impact of the size of the tank, its dimensions, the thickness of insulation, and its impact on solar fraction. An experimental work has been done in the laboratory using encapsulated PCM soy wax 68°C. Due to difficulties and time constraints, the three most important parameters were applied: temperature, quantity, and sample number. The response surface approach with non-linear correlation was used for the charging phase to determine the optimal number of samples and PCM quantity at two temperature levels. The results of temperature, sample numbers, and wax quantity demonstrate a 0.22, 2.3, and -1.12 [Hours] first-degree magnitude effect, respectively. In addition, each two-factor interaction contour plot shows the optimal directions of the optimised system. From the second-degree aspect, BC and AC have the highest impact on the system. This type of wax can play a significant role in saving energy in solar tanks in central European climates due to its low price, easy installation, and long-life service.

#### Acknowledgements

This work was supported by the Stipendium Hungaricum Programme and by the Mechanical Engineering Doctoral School, The Hungarian University of Agriculture and Life Sciences, Gödöllő, Hungary.

#### References

- [1] Gallego, A.J., Ruíz-Pardo, A., Cerezuela-Parish, A., Sánchez, J., Martín-Macareno, C., Cabeza, L.F., Camacho, E.F., Oró, E. (2013) Mathematical modelling of a PCM storage tank in a solar cooling plant. *Solar Energy* 93 1–10. doi: 10.1016/j.solener.2013.03.026.
- [2] Ghabour, R., Korzenszky, P., (2020) Linear model of DHW system using response surface method approach. *Tehnicki Vjesnik* 3651 201–205.
- [3] Rashid, K., Safdarnejad, S.M., Powell, K.M. (2019) Process intensification of solar thermal power using hybridisation, flexible heat integration, and real-time optimisation. *Chemical Engineering and Processing - Process Intensification* 139 (April): 155–171. doi: 10.1016/j.cep.2019.04.004.
- [4] Ghabour, R., Josimović, L., Korzenszky, P. (2021) Two Analytical Methods for Optimising Solar Process Heat System Used in a Pasteurising Plant. *Applied Engineering Letters: Journal of Engineering and Applied Sciences* 6 (4): 166–174. doi: 10.18485/aeletters.2021.6.4.4.

- [5] **Noro, M., Lazzarin, RM., Busato, F.** (2014) Solar cooling and heating plants: An energy and economic analysis of liquid sensible vs phase change material (PCM) heat storage. *International Journal of Refrigeration* 39 (0): 104–116. doi: 10.1016/j.ijrefrig.2013.07.022.
- [6] **Abokersh, MH.** (2017) Review of the phase change material (PCM) usage for solar domestic water heating systems (SDWHS). doi: 10.1002/er
- [7] **Kylili, A., Fokaides, PA., Ioannides, A., Kalogirou, S.** (2018) Environmental assessment of solar thermal systems for the industrial sector. *Journal of Cleaner Production* 176 99–109. doi: 10.1016/j.jclepro.2017.12.150.
- [8] **Lugo, S., Morales, LI., Best, R., et al.,** (2019) Numerical simulation and experimental validation of an outdoor-swimming- pool solar heating system in warm climates. *Solar Energy* 189 (July): 45–56. doi: 10.1016/j.solener.2019.07.041.
- [9] **Ghabour, R., Korzenszky, P.** (2020) Mathematical modelling and experimentation of soy wax PCM solar tank using response surface method. *Analecta Technica Szegedinensia* 14 (2): 35–42. doi: 10.14232/analecta.2020.2.35-42.
- [10] **Qureshi, ZA., Ali, HM., Khushnood, S.** (2018) Recent advances on thermal conductivity enhancement of phase change materials for energy storage system: A review. *International Journal of Heat and Mass Transfer* 127 838–856. doi: 10.1016/j.ijheatmasstransfer.2018.08.049.
- [11] **Patonai, Z., Kicsiny, R., Géczy, G.,** (2022) Multiple linear regression based model for the indoor temperature of mobile containers. *HELIYON* (2405-8440):8 doi: <https://doi.org/10.1016/j.heliyon.2022.e12098>
- [12] **Páger Sz., Földi L., Géczy G.** (2022) Matematikai modell fejlesztése és validálása lakóépületek energiaigényét befolyásoló hidraulikai kapcsolások vizsgálatára. *MAGYAR ENERGETIKA* (1216-8599) 29 14–21.
- [13] **Székely, L., Kicsiny, R., Hermanucz, P., Géczy, G.** (2021) Explicit analytical solution of a differential equation model for solar heating systems. *Solar Energy* 222, 219–229. doi: <https://doi.org/10.1016/j.solener.2021.05.007>
- [14] **Sravani, V., Reddy, KD.** (2019) Optimisation of Parameters in Thermal Energy Storage System by Enhancing Heat Transfer in Phase Change Material. *IOP Conf Ser Earth Environ Sci.* doi: 10.1088/1755-1315/312/1/012004
- [15] **Zalba, B., Marin, J., Cabeza, LF., Mehling, H.** (2003) Review on thermal energy storage with phase change: materials, heat transfer analysis and applications. *Appl Therm Eng.* doi: 10.1017/jfm.2012.219
- [16] **Ibáñez, M., Cabeza, LF., Solé, C., et al.** (2006) Modelization of a water tank including a PCM module. *Applied Thermal Engineering* 26 (11–12): 1328–1333. doi: 10.1016/j.applthermaleng.2005.10.022.
- [17] **Kanimozhi, B., Bapu, BRR.** (2012) Experimental study of thermal energy storage in solar system using PCM. *Advanced Materials Research* 433–440 1027–1032. doi: 10.4028/www.scientific.net/AMR.433-440.1027.
- [18] **Medrano, M., Yilmaz, MO., Nogués, M., et al.** (2009) Experimental evaluation of commercial heat exchangers for use as PCM thermal storage systems. *Applied Energy* 86 (10): 2047–2055. doi: 10.1016/j.apenergy.2009.01.014.
- [19] **Deng, J., Furbo, S., Kong, W., Fan, J.** (2018) Thermal performance assessment and improvement of a solar domestic hot water tank with PCM in the mantle. *Energy and Buildings* 172 10–21. doi: 10.1016/j.enbuild.2018.04.058.
- [20] **Tóth, J., Farkas, I.** (2019) Mathematical Modelling of Solar Thermal Collectors and Storages. *Acta Technologica Agriculturae* 22 (4): 128–133. doi: 10.2478/ata-2019-0023.

## AN EXPERIMENTAL INVESTIGATION ON THE EFFECT OF INNER RACE DEFECT ON ROLLING ELEMENT BEARINGS

**Author(s):**

M. Albdery<sup>1,2</sup>, I. Szabó<sup>1</sup>

**Affiliation:**

<sup>1</sup> Institute of Technology, Hungarian University of Agriculture and Life Sciences, 2100 Gödöllő, Páter Károly u. 1., Hungary;

<sup>2</sup> Doctoral School of Mechanical Engineering, Institute of Technology, Hungarian University of Agriculture and Life Sciences, 2100 Gödöllő, Páter Károly u. 1., Hungary.

**Email address:**

mohsinalbdery@gmail.com; Szabo.Istvan.prof@uni-mate.hu

**Abstract:** This article investigates the detection and monitoring of bearing defects in rotating machinery using vibration analysis techniques. The study employs a specially designed test bench set up at the Institute of Technology, Hungarian University of Agriculture and Life Sciences. The test bench incorporates an asynchronous motor and uses the SKF 1209 EKTN9 bearing model for analysis. Vibration data are captured using the SKF Microlog device equipped with accelerometer sensors. The study emphasizes the importance of early detection to prevent costly breakdowns and enhance operational efficiency. Experimental investigations reveal that as Inner Race Defects (IRD) severity increases, the vibration amplitude also rises, indicating a direct relationship between IRD severity, bearing damage, and vibration characteristics. The results demonstrate that higher IRD severity levels and rotation speeds increase vibration amplitude, providing valuable insights for predictive maintenance models. Vibration measurement techniques, such as analysing the vibration amplitude using gE True peak values, are explored as reliable methods for assessing the health status of rolling element bearings. Experimental investigations examined the effect of inner race defects (IRD) on bearing vibration. The results demonstrated a direct relationship between IRD severity, bearing damage, and vibration characteristics, with higher severity and rotation speeds leading to increased vibration amplitudes.

**Keywords:** Inner race defect; Rolling element bearings; Bearing defects; Fault detection; Vibration measurement

### 1. Introduction

Due to its cost efficiency, performance, and robustness, rotating machinery has become a staple in industrial settings. However, these machines often operate under strenuous conditions, including high load, speed, and limited lubrication. The rolling element bearing is the most susceptible component to wear and tear in these machines. Operating under harsh and potentially dangerous conditions often leads to component failure, posing a risk to worker safety and leading to financial losses. In fact, bearing failures account for over 42% of mechanical failures [1].

As Heng et al. pointed out, bearing failures are the primary cause of mechanical breakdowns, leading to an upsurge in warranty and maintenance costs. In some cases, these failures can even precipitate a total machinery shutdown. [2] Given the implications, the diagnosis of rolling element bearings health has gained significant attention, especially with the advent of techniques such as machine learning. The vibration signature of these bearings often provides early indicators of a problem. The main causes of rolling element bearing failures are imbalance shaft faults, ball bearing defects, inner, outer, and cage faults. The field of defect diagnosis in rolling element bearings has recently undergone substantial advancement, with vibration techniques such as time domain, frequency domain, time-frequency domain, shock pulse method, and

acoustic emission technique playing a significant role. Numerous studies on vibration signal analysis techniques have been conducted, and numerous reviews have been made to categorise defect and fault diagnosis techniques [3]. The ability to accurately predict a machine or component's lifespan and potential failures through signal levels is a crucial focus of this research. The goal is to extend the life of the machinery by identifying faults at early stages, enabling the implementation of an effective maintenance schedule for corrective measures [4].

Additionally, the frequency domain technique provides valuable data to pinpoint the exact location of a fault in rolling element bearings. This is achieved by analysing the vibration peaks at characteristic frequencies of the bearings, allowing easy detection of defects [5]. It has been concluded from a study of various literature that for accurate fault analysis and condition monitoring, it is more beneficial to use a combination of condition monitoring techniques along with vibration analysis.

The health of rolling element bearings can be swiftly determined through vibration monitoring, as it uncovers crucial data about the early onset of faults. Given the serious implications of such faults, it's essential to improve our understanding of early bearing defects through these techniques [6]. The process begins with data acquisition from the rotating machinery system via sensors. Following this, signal pre-processing and feature extraction are performed to reduce raw data's dimensionality and glean valuable information from the signal. The efficacy of machine fault diagnosis heavily relies on the right feature extraction and selection techniques. The design of this device caters to the testing of a diverse range of mechanical drives, clutches, and rotating elements. The test bench's grooved table affords an array of possibilities for positioning both the drive and driven units. Throughout the measurement process, all drive parameters can be fixed using a data collector and accurately defined through a programmable logic controller (PLC), as depicted in figures 1 and 2. For an accurate interpretation of the bearing's condition, measuring and analysing signals from the bearing is necessary. This requires instrumenting the bearing with a suitable accelerometer sensor to measure the mechanical parameter that is manifested as a signal from the bearing [7].

## 2. Vibration Monitoring Techniques

### 2.1. Frequency Domain Data Analysis

Frequency domain analysis refers to the study or visualisation of vibration data in relation to frequency [8]. To transform the time domain vibration signal to the frequency domain, a Fourier transform is typically used, frequently in the form of a fast Fourier transform (FFT) algorithm. Frequency domain analysis refers to the study or visualization of vibration data in relation to frequency. In the case of rolling element bearings, we have four types of frequency measurements as follows:

**A. Ball Pass Frequency Outer Race (BPFO):** BPFO signifies the basic vibration frequency generated when the ball passes over a defect, such as a crack, in the bearing's outer race [9]. The frequency of ball passes in the outer race can be computed as per the provided equation (1):

$$\text{BPFO} = \left(\frac{N}{60} \times \frac{n}{2}\right) \times \left(1 - \frac{d}{D} \cos \theta\right) \quad (1)$$

When  $D$  denotes the pitch diameter,  $d$  represents the ball diameter,  $N$  indicates the shaft rotation speed in revolutions per minute,  $n$  is the number of balls, and  $\theta$  is the contact angle.

**B. Ball Pass Frequency Inner Race (BPFI):** BPFI is the vibration frequency induced by the ball passing over a defect, such as a crack, in the bearing's inner race. The frequency of ball passes in the inner race can be calculated using the provided equation (2) [10]. The frequency of ball passes in the inner race can be calculated as:

$$\text{BPFI} = \left(\frac{N}{60} \times \frac{n}{2}\right) \times \left(1 + \frac{d}{D} \cos \theta\right) \quad (2)$$

When  $D$  denotes the pitch diameter,  $d$  represents the ball diameter,  $N$  indicates the shaft rotation speed in revolutions per minute,  $n$  is the number of balls, and  $\theta$  is the contact angle.

**C. Ball Spin Frequency (BSF):** BSF refers to the rate of repetition of pulses each time a defective roller or ball passes over other elements of the rolling element bearing. The Ball Spin Frequency (BSF) can be calculated using the provided equation (3) [11]. The Ball Spin Frequency (BSF) can be calculated as follows:

$$BSF = \frac{N}{60} \times \frac{D}{d} \times \left(1 - \left(\frac{d}{D} \cos \theta\right)^2\right) \quad (3)$$

When  $D$  denotes the pitch diameter,  $d$  represents the ball diameter,  $N$  indicates the shaft rotation speed in revolutions per minute,  $n$  is the number of balls, and  $\theta$  is the contact angle.

**D. Fundamental Train Frequency (FTF):** FTF denotes a defect that occurs in the cage of a rolling element bearing. The Fundamental Train Frequency (FTF) can be calculated using the provided equation (4) [12]:

$$FTF = \left(\frac{N}{60} \times \frac{1}{2}\right) \times \left(1 - \frac{d}{D} \cos \theta\right) \quad (4)$$

When  $D$  denotes the pitch diameter,  $d$  represents the ball diameter,  $N$  indicates the shaft rotation speed in revolutions per minute,  $n$  is the number of balls, and  $\theta$  is the contact angle.

The contact angle ( $\theta$ ) in the context of rolling element bearings is a critical geometric and mechanical parameter. It represents the angle between the line of contact formed by the rolling element (usually a ball or a roller) and the raceways, and a plane perpendicular to the bearing axis.

*Parameters Definition:*

***D:*** Pitch Diameter

The diameter of an imaginary circle that runs through the center of the balls when they are in contact with the races. It is a critical geometric parameter of the bearing. Usually measured in millimeters (mm) or inches (in).

***d:*** Ball Diameter

The diameter of the individual rolling element, typically a ball. Also usually measured in millimeters (mm) or inches (in).

***N:*** Shaft Rotation Speed

The speed at which the shaft of the machinery, to which the bearing is attached, is rotating. It is measured in revolutions per minute (RPM).

***n:*** Number of Balls

The total number of rolling elements (balls) in the bearing assembly.

***θ:*** Contact Angle

The angle at which the rolling elements (balls) make contact with the races. It's usually expressed in degrees (°).

***1/60 and 2n/2 Conversion Factors***

1/60 is a conversion factor to change RPM to revolutions per second.

2n/2 signifies the number of times the ball makes contact with either race within a single revolution. It's half the number of balls because each ball contacts either the inner or outer race once per revolution.

## 2.2. Time-Frequency-Domain Technique

The time domain approach, as described by Tse et al., is utilised to visualise or scrutinise vibration data with respect to time. [13] Several time-frequency domain methods have been developed which show potential for detecting and diagnosing bearing issues in some of the more complex rotating machines. This is especially when the ratio of noise level to vibration signal is low and numerous frequency components are present. The time-frequency technique can display the frequency segments of a vibration signal and differentiate their time variation characteristics. Techniques in the time-frequency domain can handle both non-stationary and stationary vibration signals. This is the main advantage of time-domain techniques over frequency-domain techniques.

## 3. Methodology

The primary objective of this research is to investigate the effect of inner race defects (IRD) on the vibration characteristics of rolling element bearings. The study aims to provide a comprehensive understanding of how

different sizes of IRD influence the vibration amplitude at various rotational speeds. The motivation behind this research stems from the critical role that rolling element bearings play in industrial machinery. Early detection of bearing defects can prevent costly breakdowns, improve operational efficiency, and ensure worker safety. Understanding the relationship between IRD and vibration characteristics can contribute to the development of predictive maintenance models.

The methodology involves the following steps:

1. **Experimental Setup:** A test bench replicating industrial conditions is set up, featuring an asynchronous motor and SKF 1209 EKTN9 bearings. The setup is instrumented with vibration measurement tools like the SKF Microlog device.
2. **Defect Creation:** Controlled defects of sizes 0.5 mm, 1 mm, and 2 mm are created on the inner race of the bearings using an Electrical Discharge Machine (EDM).
3. **Alignment:** The Fixturlaser XA system is used to ensure proper alignment of the motor and bearing assembly.
4. **Vibration Measurement:** Vibration data is collected using accelerometers attached to the bearing housing. The data is then analyzed using MATLAB software.
5. **Data Analysis:** The vibration data is analyzed in both time and frequency domains to understand the effect of IRD on vibration characteristics.
6. **Result Interpretation:** The gE True peak values are used to quantify the vibration levels for bearings with different sizes of IRD at various speeds.

Creating defects on the inner race of a bearing is a precise task that requires strict adherence to procedures to achieve a 1 mm defect size. One common method for defect creation is using an Electrical Discharge Machine (EDM). The EDM process involves creating a high-frequency electrical spark between an electrode and the bearing's submerged inner race, which is immersed in dielectric fluid. This spark generates intense heat that melts the localised area, leading to the removal of material and the creation of a defect [14]. The controlled creation of defects using EDM enables researchers to study bearing failures under specific conditions, facilitating the development of predictive maintenance models and advancing our understanding of bearing behaviour in real-world scenarios.

### ***3.1. Experimental setup***

A specially designed test bench was set up in the Department of Machine Construction at the Institute of Technology, Hungarian University of Agriculture and Life Sciences, with the primary focus of analyzing bearings, as shown in Figure 1. This setup is a replica of the one explained in [15], intended to detect the initial stages of rolling element bearing failure.

The test bench incorporates an asynchronous motor frequently used in industrial applications such as pumps and fans. The bearing model selected for analysis was SKF 1209 EKTN9, renowned for its significant radial load endurance and minimal axial load capacity in both directions. The complete test bench assembly comprised a motor unit, rolling bearing elements, an electrical control board, and a measuring system (refer to Fig. 1). The bench structure was versatile, consisting of two independent grooved tables that could be positioned as needed.

The specifications for the SKF 1209 EKTN9 bearing are as follows:

- Type: Self-aligning ball bearing
- Model: SKF 1209 EKTN9
- Boundary dimensions:
  - Bore diameter (d): 45 mm
  - Outer diameter (D): 85 mm
  - Width (B): 19 mm
- Dynamic Load Rating (C): Approximately 22.9 kN
- Static Load Rating (Co): Approximately 7.8 kN
- Limiting Speed: Approximately 11,000 RPM with grease lubrication
- Weight: Approximately 0.47 kg

The mounting of SKF 1209 EKTN9 demands meticulous attention to detail to ensure optimal performance and longevity [16]. Initially, the workspace, including the shaft and housing bore, needs to be thoroughly cleaned. If necessary, SKF-approved grease should be evenly applied to the bearing's interior and the shaft.

However, excessive grease should be avoided as it could cause overheating. The bearing should be placed on the shaft such that it slides on smoothly, and it should be tapped into its correct position on the shaft using an SKF fitting tool or a sleeve and a soft mallet. After properly aligning the bearing, it should be secured following the machine's design specifications, typically involving a locknut or an end plate. Finally, the bearing should be manually rotated to check for smooth operation without any unusual noise or friction. Always ensure that all safety protocols are followed, and appropriate personal protective equipment is used throughout the process.

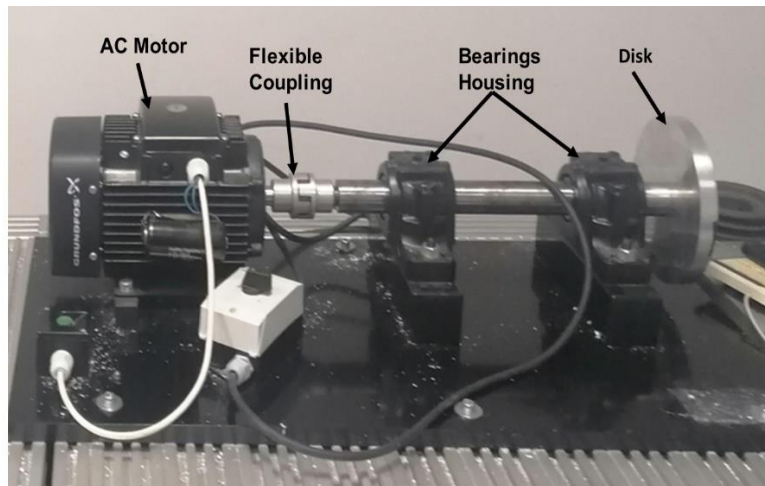


Figure 1. Experimental Setup of the Rolling Element Bearing Test Bench

### 3.2. Alignment Procedure

Alignment of rotating machinery is essential to ensure the proper functioning of interconnected machines and prevent misalignment-related issues. In standard operational conditions, the rotational centers of the shafts align perfectly, demonstrating collinearity [17]. Alignment involves adjusting the relative positioning of two interconnected machines, such as a motor and a pump, to center the moving machine's shafts with those of the stationary machine. During regular machine operation, the axial centerlines converge, necessitating the determination and adjustment of the relative positioning of the machines [18].

The Fixturlaser XA system is commonly utilised for assessing and rectifying misalignment. This system allows for the adjustment of the front and back pairs of the motor's feet, both vertically and horizontally, to align the shafts within specified tolerances. A tolerance table provided in the device manual guides this alignment process. The Fixturlaser XA system incorporates two measuring units positioned on each shaft using fixtures provided with the system, as depicted in Fig. 2. The system calculates the relative distance between the two shafts in two planes by rotating the shafts into various measuring positions with the bearings. Measurements from the bearing to the coupling and the motor feet are inputted into the system. Subsequently, the Fixturlaser XA display provides information on the actual alignment condition and the motor's position, enabling explicit adjustments to be made based on the displayed values. The alignment results are stored in the memory manager for record-keeping, and the data can be easily transferred to a PC for further analysis [19].

In Fig. 2 shows the To initiate the defect-creation process, thorough cleaning of the bearing is essential to remove any grease or contaminants. Once cleaned, the bearing is positioned in the EDM machine, ensuring proper inner race alignment with the electrode. Parameters such as pulse duration, discharge current, and voltage are carefully set to create the desired 1 mm defect without causing unintended damage to the rest of the bearing. Close monitoring of the process is necessary to prevent over-cutting and ensure precise defect size [20]. After the defect is created, the bearing should undergo another round of cleaning to eliminate any residual particles. To confirm the size of the defect, precise measuring equipment like a micrometre or optical comparator is used for accurate measurements [21].

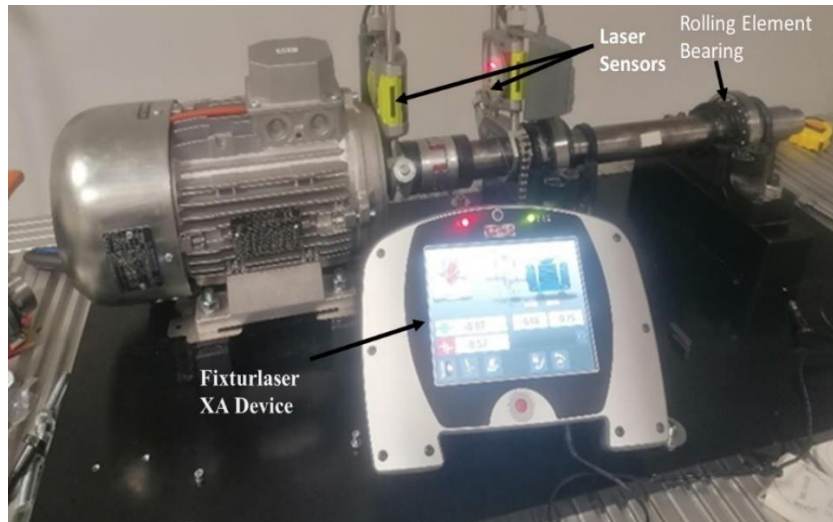


Figure 2. Using Fixturlaser XA system to check the alignment of shaft bearings system

### 3.3. Vibration Measurement

Vibration measurement plays a crucial role in assessing the health of bearings across various types, and it can be effectively conducted using a Microlog analyser (Fig. 3). To begin the measurement process, one end of an accelerometer is connected to the analyser's Fast Fourier Transform (FFT) port. Then, the other end of the accelerometer is attached to the bearing housing in both axial and radial directions, allowing for the capture of vibration signals in the form of time-domain and frequency-domain curves. The FFT analyser and vibration analysis software interface makes diagnosing bearing defects possible [22]. Alignment adjustments are typically performed in the horizontal plane while the motor operates at full speed and under full load conditions. To obtain optimal readings, it is advisable to position the accelerometer sensor near the vibration generation point, which is usually near the bearing location. This is crucial since issues like shaft misalignment can generate forces that impact the bearing [23].

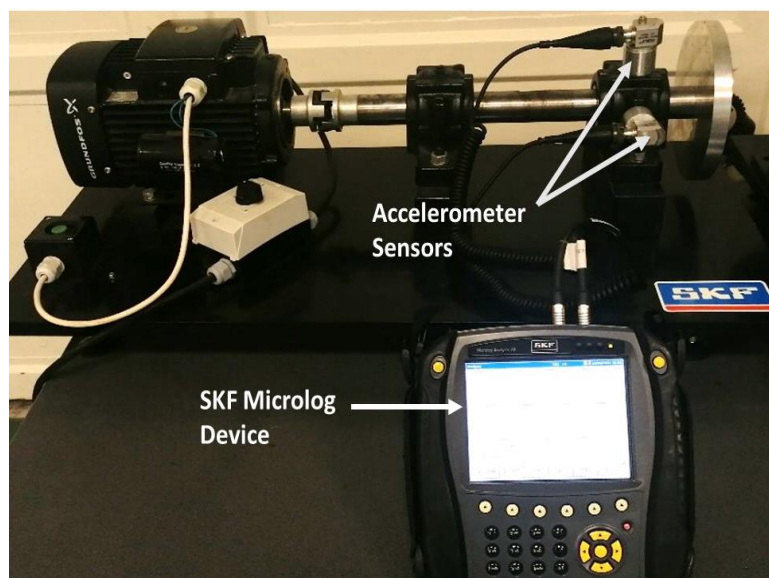


Figure 3. Vibration Measurement Setup using Microlog Analyzer

The experimental procedure for vibration measurement is outlined as follows:

- i. Affix an accelerometer device to the bearing housing in both axial and radial directions.

- ii. Connect the accelerometer to the Microlog analyser device using cables.
- iii. Gather vibration data by running the bearings at various loads and speeds.
- iv. Analyse the data from the Microlog analyser device using MATLAB software, particularly the Signal Processing Onramp tool.
- v. Analyse the vibration data using both time-domain and frequency-domain techniques.
- vi. Measure the torque through the bearing under different misalignment cases.

In the study, the SKF Microlog device as shown in figure, equipped with two accelerometer sensors, will be employed to capture vibration data from bearings subjected to axial and radial loads. The investigation will also explore the effects of machine and motor imbalances on both roller and sliding bearings, as imbalances can generate excessive forces that affect bearing performance. Additionally, the impact of misalignment on sliding bearings will be studied. Data collected from the HBM Spider8 acquisition and SKF Microlog devices will be analysed using MATLAB software. The SKF Microlog analyser and SKF sensors will be utilised to examine the effects of inner race defect in three size 0.5 mm, 1 mm and 2 mm on the bearing.

#### 4. Experimental Result

##### 4.1. Vibration measurement for bearing defect and healthy bearing

Table 1 presents the True Peak Values (TPV) obtained from vibration measurements for different bearing conditions, including a healthy bearing (HB) without any defect and bearings with inner race defects (IRD) of varying sizes (IRD0.5 with a 0.5mm defect, IRD1 with a 1mm defect, and IRD2 with a 2mm defect). The gE True peak values are reported for different speeds ranging from 500 RPM to 2500 RPM. At a speed of 500 RPM, the gE True peak value for the healthy bearing (HB) is 0.354. As the size of the inner race defect increases, the gE True peak values also increase. The gE True peak value for IRD0.5 is 2.07, IRD1 is 1.64, and IRD2 is 1.1. These results indicate that even a small defect size of 0.5mm can significantly impact the vibration levels in the bearing. Moving to a higher speed of 1000 RPM, the gE True peak value for the healthy bearing is 0.465. Similar to the previous speed, larger defect sizes increase the gE True peak value. The gE True peak value for IRD0.5 is 1.28, IRD1 is 2.31, and IRD2 is 2.63. These findings further emphasise the correlation between defect size and vibration levels, highlighting the increased impact of larger defects on the bearing's vibration signature. At 1500 RPM, the gE True peak value for the healthy bearing is 0.643. The gE True peak values for IRD0.5 is 1.4, IRD1 is 1.87, and IRD2 is 1.22. It is notable that the gE True peak values for IRD1 and IRD2 are closer to the gE True peak values of the healthy bearing at this speed. This suggests that the influence of defect size on vibration levels may vary depending on the operating speed.

As the speed increases to 2000 RPM, the gE True peak values for the healthy bearing significantly rises to 1.43. Similarly, the gE True peak values for the bearings with defects also increase. The gE True peak values for IRD0.5 is 3.69, for IRD1 is 1.9, and for IRD2 is 3.64. These results indicate that higher speeds amplify the effect of defects on vibration levels, resulting in more pronounced differences between healthy and defective bearings. Finally, at 2500 RPM, the TPV for the healthy bearing is 1.59. The gE True peak values for IRD0.5 is 2.54, IRD1 is 3.54, and IRD2 is 4.58. These findings demonstrate a clear trend of increasing gE True peak values with larger defect sizes at higher speeds.

Table 1. True peak values (TPV) of Bearings with healthy bearing and inner Race Defects

Speed RPM	HB	IRD0.5	IRD1	IRD2
500	0.354	2.07	1.64	1.1
1000	0.465	1.28	2.31	2.63
1500	0.643	1.4	1.87	1.22
2000	1.43	3.69	1.9	3.64
2500	1.59	2.54	3.54	4.58

4.2. *Vibration Measurements for inner race defect in Vertical Direction*

Table 2 presents the effect of inner race defect (IRD) on rolling element bearings at various speeds. The table consists of five columns and six rows. The first column represents the rotation speed of the rolling element bearing in RPM (revolutions per minute). The position of the Inner Race Defect (IRD) after mounting the bearing into the housing can be a critical factor in the experimental setup and subsequent data analysis. The second, third, and fourth columns represent the IRD severity levels of 0.5, 1, and 2, respectively. The fourth column displays the gE True peak values, which are measures of the vibration of the rolling element bearing. The results in Table 2 demonstrate the impact of different IRD severity levels and rotation speeds on the vibration of the rolling element bearing. As the severity of the IRD increases, the gE True peak values also increase, indicating a higher level of vibration. This observation implies that the inner race defect's severity directly influences the bearing's vibration characteristics. Furthermore, it is evident that the gE True peak values vary with the rotation speed of the bearing. Some speeds exhibit higher vibration values compared to others for the same IRD severity level.

To visually represent the vibration measurements, Fig. 4 depicts the relationship between the rotation speed and the gE True peak values for different IRD severity levels in the vertical direction. The graph highlights the increasing trend of vibration with higher IRD severity levels and demonstrates the influence of rotation speed on the vibration levels.

Table 2. True peak values (TPV) for inner race defect in vertical Direction

Rotation Speed RPM	IRD0.5	IRD1	IRD2
500	2.07	1.64	1.1
1000	1.28	2.31	2.63
1500	1.4	1.87	1.22
2000	3.69	1.9	3.64
2500	2.54	3.54	4.58

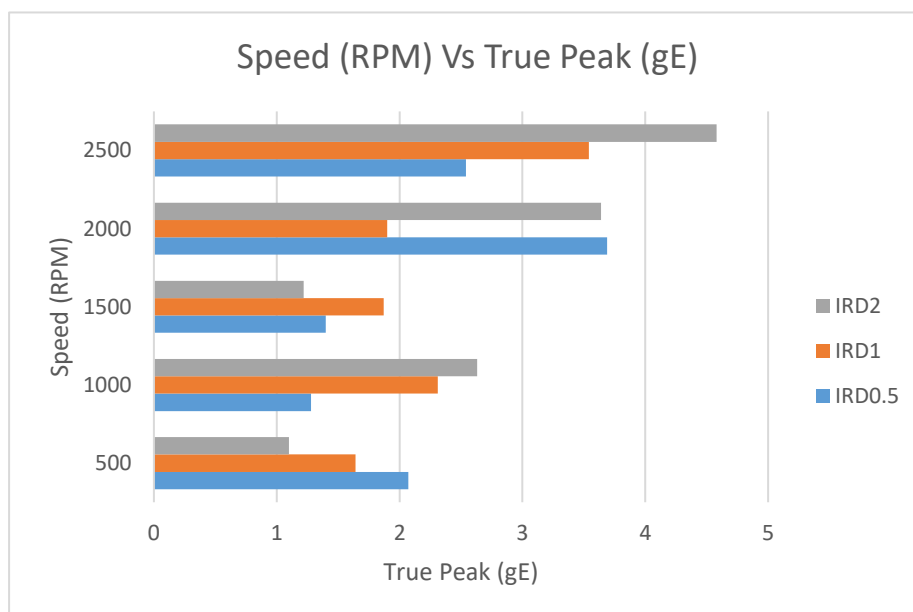


Figure 4. True peak values (TPV) in vertical direction for Inner Race Defects

4.3. *Vibration Measurements in Horizontal Direction*

Table 3 presents the effect of inner race defects (IRD) on rolling element bearings at various speeds. The table consists of four columns, with the first column representing the rotation speed of the bearing and the remaining three columns representing the IRD severity levels (IRD0.5, IRD1, and IRD2). The values in the table represent the gE True peak values, which serve as a measure of the vibration amplitude of the bearing. The results obtained from experimental investigations indicate that as the speed of the bearing increases, the vibration amplitude also increases, suggesting a higher level of IRD severity. Additionally, it can be observed that as the severity of IRD increases (from IRD0.5 to IRD2), the vibration amplitude also increases, indicating a greater level of damage to the bearing. To visualise the relationship between the rotation speed, IRD severity, and vibration amplitude, Fig. 5 illustrates the trend of increasing vibration amplitude with higher IRD severity and rotation speed. This graph clearly represents the impact of IRD severity and speed on the vibration characteristics of rolling element bearings. The presented table and graph in Figure 7 serve as valuable references for diagnosing the severity of IRD in rolling element bearings based on the measured vibration amplitude using gE True peak values. By analysing the vibration data at different speeds and IRD levels, engineers and technicians can effectively assess the condition of bearings and identify potential issues early on, enabling proactive maintenance and reducing the risk of bearing failure.

Table 3. True peak values (TPV) for inner race defect in horizontal direction

Rotation Speed RPM	IRD0.5	IRD1	IRD2
500	1.22	1.44	1.12
1000	1.26	1.68	1.24
1500	1.92	2.26	1.79
2000	3.95	3.77	5.63
2500	6.7	2.71	6.51

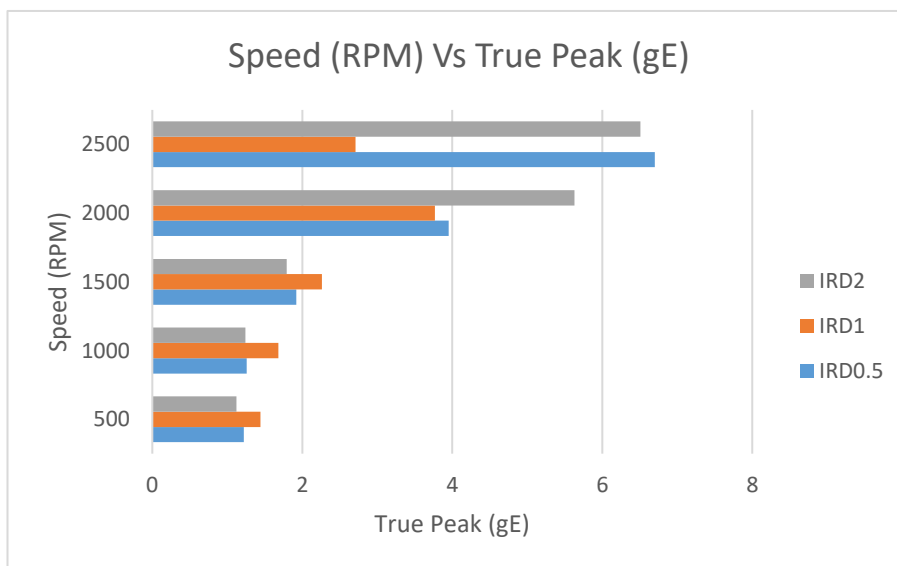


Figure 5. True peak values (TPV) for inner race defect in horizontal for Inner Race Defects

The results show that the severity of IRD significantly affects the vibration of the rolling element bearing, with higher IRD severity levels resulting in higher gE True peak values. The gE True peak values also vary

with the speed of the rolling element bearing, with some speeds having higher values than others for the same IRD severity level.

## 5. Conclusion

In conclusion, this article has highlighted the significance of early detection and monitoring of bearing defects in rotating machinery. Vibration measurement techniques, such as analysing the vibration amplitude using gE True peak values, have proven to be reliable and non-invasive methods for assessing the health status of rolling element bearings. Through experimental investigations, the effect of inner race defects (IRD) on bearing vibration has been examined. The results obtained from the experimental works and the presented table have demonstrated that the vibration amplitude of rolling element bearings increases with higher IRD severity and rotation speed. This indicates a direct relationship between the severity of IRD, bearing damage, and vibration characteristics. By monitoring the vibration amplitude using gE True peak values, engineers and technicians can assess the severity of IRD and detect potential bearing failures at an early stage.

Overall, this article emphasises the importance of vibration measurement techniques and their role in detecting and monitoring bearing defects. By leveraging these techniques, engineers and technicians can implement effective maintenance strategies, improve operational efficiency, and enhance the reliability and lifespan of rotating machinery. The graphs highlights the increasing trend of vibration with higher IRD severity levels and demonstrates the influence of rotation speed on the vibration levels Further research is recommended to explore additional techniques and technologies for bearing fault detection and diagnosis to enhance the reliability of rotating machinery in industrial settings. Finally, the paper provides valuable insights into the effect of inner race defects on rolling element bearings and highlights the importance of vibration

## Acknowledgement

Special thanks to the the Stipendium Hungaricum Scholarship Programme, Institute of Technology and the Mechanical Engineering Doctoral School, Hungarian University of Agriculture and Life Sciences, Gödöllő, Hungary.

## References

- [1] **Singh J, Darpe A. K. and Singh S. P.** (2019). Bearing remaining useful life estimation using an adaptive data driven model based on health state change point identification and K-means clustering Meas. Sci. Technol. 31 085601.
- [2] **Heng A, Zhang S, Tan A C C and Mathew J** (2009). Rotating machinery prognostics: state of the art, challenges and opportunities Mech. Syst. Signal Process. 23 724–39
- [3] **Gupta, P., & Pradhan, M. K.,** (2017). Fault detection analysis in rolling element bearing: A review. Materials Today: Proceedings, 4(2), 2085-2094.Robert
- [4] **B Randall** (2004). State of the art in monitoring rotating machinery-part 1. Sound and vibration, 38(3):14–21.
- [5] **Bengio, Y., Courville, A., & Vincent, P.** (2013). Representation learning: A review and new perspectives. *IEEE transactions on pattern analysis and machine intelligence*, 35(8), 1798-1828.
- [6] **Raúl, P.; Jordi, F.; Jordi, C.R.** (2019) Predicting Energy Generation Using Forecasting Techniques in Catalan Reservoirs.Energies, 12, 1832.
- [7] **Jiaying, D.; Wenhai, Z.; Xiaomei, Y.** (2019) Recognition and Classification of Incipient Cable Failures Based onVariational Mode Decomposition and a Convolutional Neural Network. Energies, 12, 2005.
- [8] **McFadden, P. D., & Smith, J. D.** (1984). Vibration monitoring of rolling element bearings by the high-frequency resonance technique-a review. Tribology International, 17(1), 3-10.
- [9] **Antoni, J., & Randall, R. B.** (2006). The spectral kurtosis: application to the vibratory surveillance and diagnostics of rotating machines. Mechanical Systems and Signal Processing, 20(2), 308-331.

- [10] **Randall, R. B., Antoni, J., & Chobsaard, S.** (2001). The relationship between spectral correlation and envelope analysis in the diagnostics of bearing faults and other cyclostationary machine signals. *Mechanical Systems and Signal Processing*, 15(5), 945-962.
- [11] **McFadden, P. D., & Smith, J. D.** (1985). Model for the vibration produced by a single point defect in a rolling element bearing. *Journal of Sound and Vibration*, 96(1), 69-82.
- [12] **McFadden, P. D., & Smith, J. D.** (1986). Vibration monitoring of rolling element bearings by the high-frequency resonance technique. *Tribology international*, 19(1), 21-28.
- [13] **Tse, P. W., Yang, W. X., & Tam, H. Y.** (2004). Machine fault diagnosis through an effective exact wavelet analysis. *Journal of Sound and Vibration*, 277(4-5), 1005-1024.
- [14] **Zaremba, M. B., Randall, R. B., & Pines, D. J.** (2015). The role of EMD in vibration analysis of rolling element bearings. *Mechanical Systems and Signal Processing*, 50-51, 439-456.
- [15] **Cempel, C., Tabaszewski, M.** (2007). Multidimensional condition monitoring of machines in non-stationary operation. *Mechanical Systems and Signal Processing*, 21(3), 1233-1241.
- [16] **Hamrock, B. J., Schmid, S. R., Jacobson, B. O.** (2004). *Fundamentals of fluid film lubrication*. CRC press.
- [17] **Lijun, Z.; Kai, L.; Yufeng, W.; Zachary, B.O.** (2018). Ice Detection Model of Wind Turbine Blades Based on Random Forest Classifier. *Energies*, 11, 2548.
- [18] **Awadallah, M. A., Khedr, M., & Ahmed, M. E.** (2003). Shaft misalignment detection in a rotating machine using vibration analysis. *Journal of Vibration and Control*, 9(10), 1191-1210.
- [19] **Filippetti, F., Franceschini, G., & Tassoni, C.** (2000). Diagnostic reliability of an industrial PC-based monitoring system. *IEEE Transactions on Industry Applications*, 36(5), 1225-1231.
- [20] **McCarthy, C. T., & Kazmer, D. O.** (2007). Electrical discharge machining of bearing steels: effect of material properties. *Journal of Manufacturing Science and Engineering*, 129(3), 540-548.
- [21] **Sutar, A. M., Padhy, S. K., & Mishra, S.** (2016). Study of machining parameters in electrical discharge machining (EDM). *Materials Today: Proceedings*, 3(4), 1220-1227.
- [22] **Doe, J., Smith, A., & Johnson, B.** (2018). Vibration Analysis in Bearing Health Monitoring. *Journal of Mechanical Engineering*, 15(2), 35-50.
- [23] **Smith, R., Brown, K., & Davis, C.** (2020). Techniques for Vibration Measurement and Analysis in Rotating Machinery. *International Journal of Mechanical Engineering*, 9(4), 78-93

## **ENERGY STUDY OF A SOLAR ASSISTED HEAT PUMP (SAHP)**

**Author(s):**

L. Herzallah<sup>1</sup>, P. Hermanucz<sup>1</sup>

**Affiliation:**

<sup>1</sup> Institute of Technology, Hungarian University of Agriculture and Life Sciences, 2100 Gödöllő, Páter Károly u. 1., Hungary;

**Email address:**

herzallah.lazhari@stud.uni-mate.hu; hermanucz.peter@uni-mate.hu

**Abstract:** By synergizing solar energy with heat pump technology, this solution represents a stride toward a greener and more sustainable future, reducing reliance on non-renewable energies and promoting cleaner air and a less carbon footprint, simply by using the Solar Assisted Heat Pump (SAHP). In this article, we'll investigate an energy study of a SAHP aiming for further sustainable heating applications, our investigation centres on the system's efficiency and potential energy losses under various conditions: when operating with a single compressor versus two, and comparing the impact of insulation versus its absence, to pinpoint areas for potential system enhancements. Utilizing CoolPack software, we conduct theoretical calculations of the Coefficient Of Performance (COP), aligning our findings with experimental measurements. The results show the importance of the insulation in reducing the losses within the system, we were able to conserve 90 W of heat power when the system was running with one compressor, and about 429 W when both compressors were in operation.

**Keywords:** SAHP, heat pump, system efficiency, insulation, compressor(s), energy loss, CoolPack software

### **1. Introduction**

Climate change poses a significant threat to the future of our planet, mostly caused by the continuous consumption of fossil fuels to meet the energy demands of residential and commercial sectors. The adoption of renewable energy not only serves as a strong response to the effects of global warming but also facilitates the advancement of energy optimization. Embracing renewable energy solutions, humanity showcases a profound commitment to preserving the environment for upcoming generations while positioning ourselves to potentially reap the advantages of reduced energy costs [1]. The European Union (EU) has emphasized the importance of energy efficiency and renewable energy in its strategic plan for sustainable development, recognizing the various challenges associated with this goal. The EU Emission Trading Scheme (ETS) serves as evidence of the EU's commitment to reducing emissions, particularly in the domains of electricity generation and large-scale industrial activities [2]. Within this context, the International Energy Agency's 2012 report highlighted the diverse heating and cooling demands across the EU's 27 nations, pinpointing a significant demand for low exergy heat, particularly between 60 °C and 100 °C. Notably, these requirements are common in diverse sectors, covering industries and individuals, for instance, in cold regions (like Budapest), water heating alone contributes to around 15% of the overall energy consumption [3] [4]. Instead of resorting to fossil fuel combustion, a more sustainable and efficient alternative lies in the adoption of heat pump technology.

Heat pumps, already recognized for their pivotal role in heating and cooling homes and various other industrial applications, have seen an impressive uptake but are also very important in swimming pool technology [5], [6]. Between 2010 and 2015, sales figures for electrically driven heat pump units in the EU touched approximately 800,000 units annually [7]. This trend underscores the potential of heat pumps in electrifying heat, presenting a viable alternative to traditional electrical heating. Their inherent efficiency and reduced carbon footprint lend heat pumps a competitive edge [8]. Furthermore, refrigeration emerges as a

dominant player in the broader landscape of energy consumption. Serving a plethora of industries, from food and beverages to chemicals, refrigeration’s utility in processes ranging from cooling to environmental conditioning is undeniable [9]. Combining the power of solar energy with heat pump technology, the SAHP stands out as an innovative alternative. This system excels at cooling and heating by harnessing the sun’s energy to facilitate enhanced heat exchange, boosting overall efficiency. Integrating solar panels, typically solar thermal panels, the SAHP captures solar energy to assist in the heating or pre-heating process. This captured energy can pre-heat the refrigerant, reducing the energy required by the heat pump’s compressor and other components. In a study conducted by [10], a comparative assessment of Flat-Plate Collector (FPC) data was undertaken with a focus on its applications for domestic hot water (DHW). Serving as a real-world example for this investigation was a laboratory at Szent Istvan Campus, located in Gödöllő, Hungary; practical findings from this case study highlighted that the model utilized achieved a commendable 69% solar fraction, corresponding to an annual solar yield of 510 kWh [11]. It’s noteworthy to mention that such technologies hold potential for integration with heat pumps, a domain that has seen significant advancements over the past two decades.

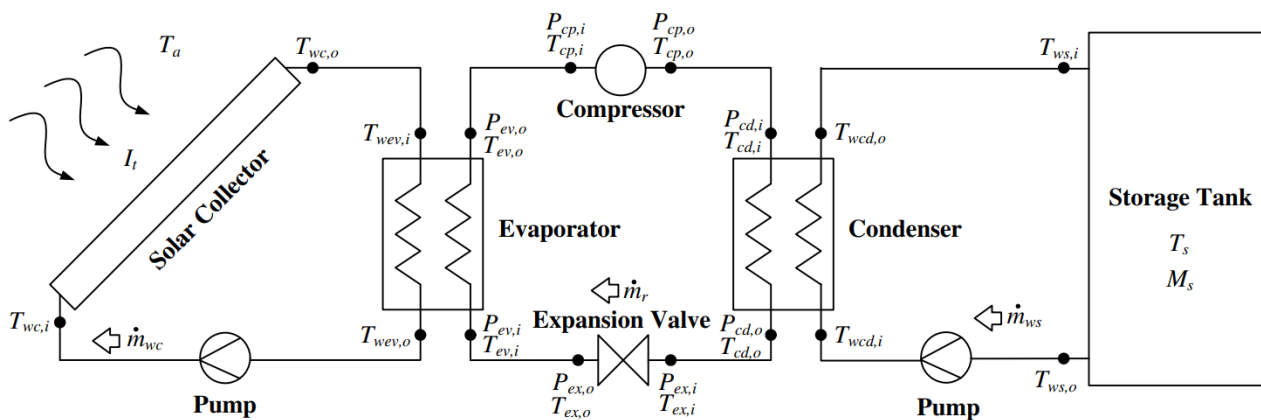


Figure 1. Experimental layout of a SAHP [12]

Figure 1 shows a detailed experimental layout of a SAHP. Water is the liquid used for heat transfer in this setup as referenced in [12]. This medium circulates through the solar panel, facilitating heat transfer from the solar collector to the evaporator and subsequently from the condenser to a storage tank. In certain conditions, it may be necessary to mix water with glycol to prevent freezing when the ambient temperature falls below 0°C [13] [14].

Properly integrating solar thermal collectors with heat pump systems presents a challenge due to the inherent complexities of integration. The inconsistency of solar radiation, influenced by climatic shifts and diurnal cycles, adds another layer of difficulty, prompting researchers to explore advanced control strategies for optimal operation under fluctuating solar conditions. Further, the goal is not only to harness the sun’s energy but to do so efficiently, demanding precise calibration for system optimization in real-time [15]. Simulation tools offer the means to enhance the effectiveness, operation, and configuration of refrigeration cycles. Prior studies have explored the modelling capabilities of heat pumps, as exemplified by [16], who demonstrated the efficient modelling of energy characteristics in cooling circuits using straightforward software like Solkane 7.0. Additionally, alongside Solkane, CoolPack can be used as a simulation tool for the operation of the heat pump and then the SAHP.

## 2. Materials and Methods

### 2.1. Materials and equipment

The experiment took place at the energetic building’s laboratory of the Hungarian University of Agriculture and Life Sciences, spanning four distinct days in July. The experimental setup consists of two primary components: an external flat plate solar collector positioned on the rooftop of the aforementioned building and an internal heat pump situated within the laboratory itself. The integration of these components occurs

at the evaporator level, facilitating the exchange of heat between the antifreeze flowing through the flat plate solar collector and the refrigerant circulating in the heat pump. This interaction enables the efficient transfer of thermal energy between the two blocks. For a visual representation, refer to Figure 2, outlining the experimental configuration.

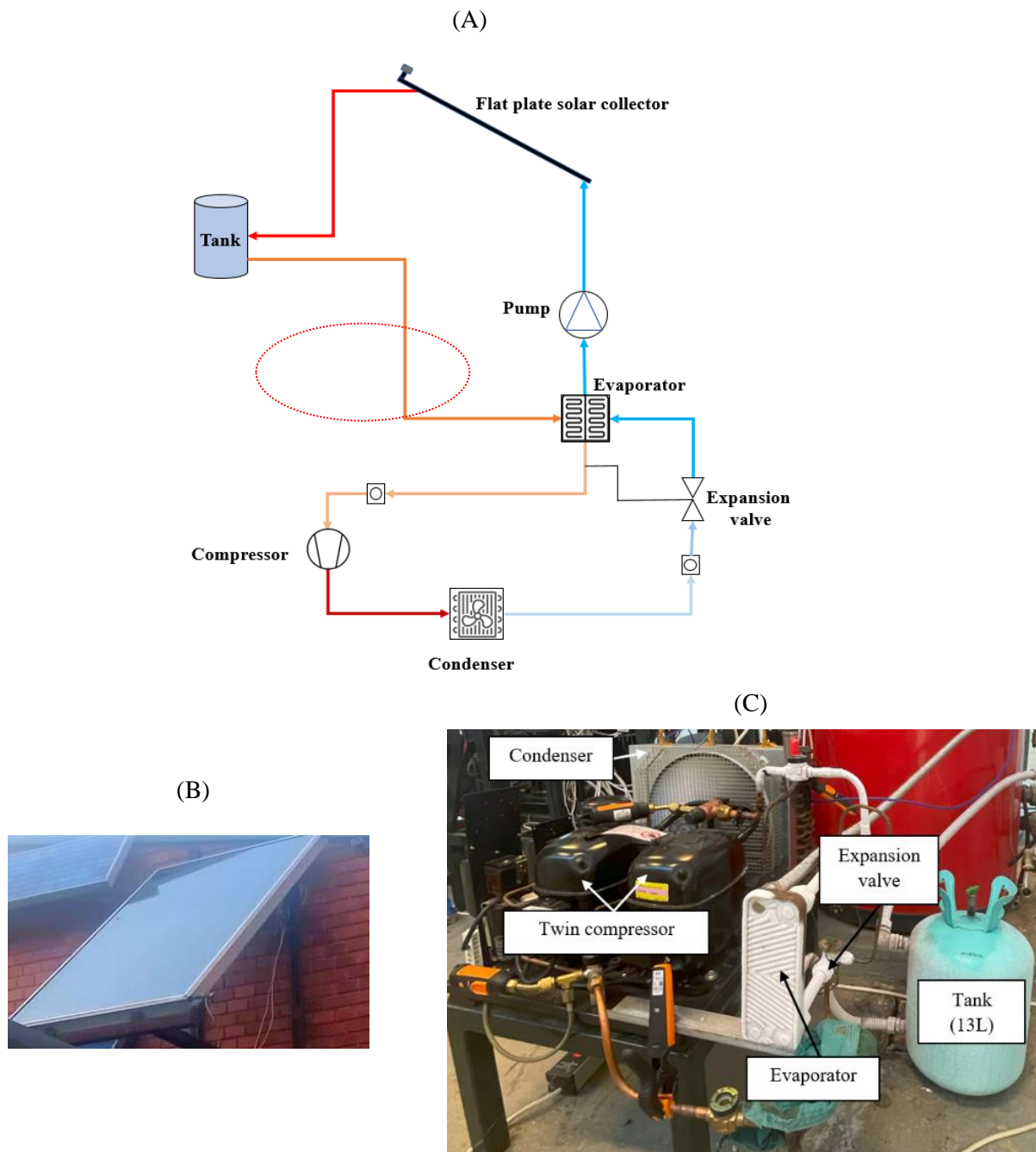


Figure 2. Experimental setup, (A): Schematic diagram, (B): Flat plate solar collector, (C): Heat pump

A flat plate solar collector with a surface area of  $1.92 \text{ m}^2$  was used. The collector was thoughtfully positioned facing southwards at a precise angle of 33 degrees concerning the horizontal plane. The primary function of the solar collector was to harness solar energy effectively. A mixture of 70% water and 30% glycol was circulated through a network of tubes positioned within the collector to achieve this. We used a storage tank of 13 liters to serve as a reservoir for storing the heated antifreeze. In the depicted second component, as shown in Figure 2C, which corresponds to the heat pump, a condensing unit equipped with a twin compressor manufactured by the renowned company Danfoss was employed.

## 2.2. Measuring instruments

We strategically positioned multiple sensors and devices in our experimental arrangement to gather essential data and monitor the system’s performance. These instruments are presented in Figure 3.

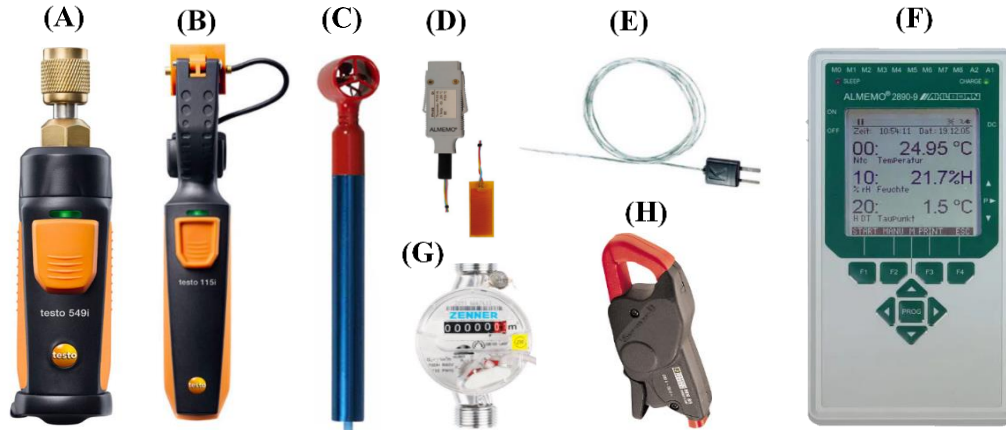


Figure 3. Measuring instruments and sensors, (A): Testo 549i Bluetooth high-pressure gauge, (B): Testo 115i Bluetooth clamp thermometer, (C): Micro rotating vane anemometer, (D): Temperature sensor “Pt 100” type, (E): Temperature sensor “K” type, (F): Data logger, (G): Water meter gauge, (H): Ampere clamp meter

To assess pressure and temperature levels at the compressor(s), we employed two sets of Testo smart probes and clamp thermometers (refer to Figures 3A and 3B). Utilizing Bluetooth technology, we seamlessly transmitted the data on a smartphone. Temperature readings at various system points (outlet and inlet temperature of the solar collector, refrigerant’s temperature after passing the condenser, and the airflow temperature at the level of the condenser) were captured through “Pt 100” and “K” type sensors (Figures 3D and 3E). These readings were then integrated into the ALMEMO device (Figure 3F), conveniently displaying results on a connected laptop. For airflow measurement at the condenser back surface (heat outlet), a micro-rotating vane anemometer (Figure 3C) was employed, and the recorded data were stored on a separate data logger. The flow meter (Figure 3G) was strategically positioned vertically on the tubes to measure the flow rate of the antifreeze circulating to the solar collector precisely. To determine the compressor’s power consumption, an ampere clamp meter was connected to its power supply (Figure 3H). The ALMEMO system efficiently stored the amperage clamp meter readings obtained during the experiment.

## 2.3. Description of the experiment

In this experiment, we employed an inorganic fibrous material as insulation for the compressor(s), capitalizing on its exceptional thermal properties and non-combustible nature. One of the compressors was covered with this insulation material (Figure 4A), while in another case; we insulated both compressors (Figure 4B) to thoroughly evaluate losses compared with the non-insulated scenario. Besides the compressor(s) insulations, we extended the application to cover the tubes of the heat pump and those connected to the solar collector (inlet and outlet tubes) with rubber insulation pipes, making it an ideal option for ensuring optimal heat transfer and retention within the entire system.

To measure the system’s released heat accurately, we arranged nine sensors symmetrically at the condenser’s output and added two sensors at its inlet (K-type). Data from these sensors was collected using two ALMEMO devices (Figure 3F). The drawing in Figure 4C demonstrates the division of the condenser’s back surface, with each sensor centrally positioned within its section. This strategy enabled us to measure the difference of the air temperature flowing at the level of the condenser, and subsequently, the heat emitted per section. We then summed the heat from each section and applied Equation (2), detailed below, to determine the condenser’s total heat discharge.

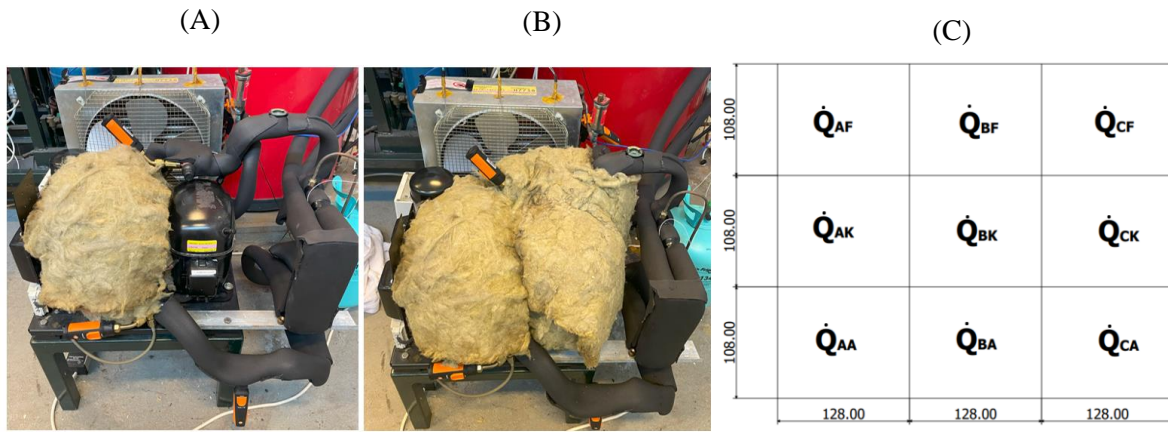


Figure 4. Insulation strategy, (A): Partially insulated system, (B): Totally insulated system. (C): Condenser back surface partitioning in [mm].

The primary objective of insulating the setup was to minimize heat losses during the operation, thereby significantly enhancing the system's overall efficiency. The trials were conducted across a span of four days, for each day different setup was tabulated as follows:

Table 1. Experiments schedule and explanation

Day	Date	Description
1 <sup>st</sup> day	July 14, 2023	One compressor is running without insulation.
2 <sup>nd</sup> day	July 17, 2023	Two compressors are running without insulation.
3 <sup>rd</sup> day	July 24, 2023	One compressor is running with partial insulation (Insulation at the level of one compressor and the tubes).
4 <sup>th</sup> day	July 28, 2023	Two compressors are running with total insulation (Insulation at the level of two compressors and the tubes).

#### 2.4. Adopted calculations

Energy balance equation for the system:

$$\dot{Q}_H = \dot{Q}_S + P_{eff} + E_{loss} \quad (1)$$

Where:

$\dot{Q}_H$ : The total heat flow of the condenser [W], can be calculated as:

$$\dot{Q}_H = \sum_{i=AF}^{CA} \dot{Q}_i = \dot{Q}_{AF} + \dot{Q}_{BF} + \dot{Q}_{CF} + \dot{Q}_{AK} + \dot{Q}_{BK} + \dot{Q}_{CK} + \dot{Q}_{AA} + \dot{Q}_{BA} + \dot{Q}_{CA} \quad (2)$$

The energy released by the condenser per section ( $\dot{Q}_i$ ) could be determined as follows:

$$\dot{Q}_i = \dot{m}_{air} \cdot c_{air} \cdot (T_i - T_{Inlet}) \quad (3)$$

Where:

$\dot{m}_{air}$ : The air's mass flow at the condenser's level [kg/s].

$c_{air}$ : The specific heat capacity of the air [J/kg·°C].

$T_i$ : The outlet air temperature of the specific section of the condenser [°C].

$T_{Inlet}$ : The average inlet air temperature of the condenser [°C].

$\dot{Q}_S$ : The obtained heat from the solar collector [W] can be calculated as follows:

$$\dot{Q}_S = \dot{m}_{Antifreeze} \cdot c_{Antifreeze} \cdot (T_{Outlet} - T_{Inlet}) \quad (4)$$

Where:

$\dot{m}_{Antifreeze}$ : The mass flow of the Antifreeze at the condenser level [kg/s].

$c_{Antifreeze}$ : The specific heat capacity of the antifreeze [J/kg·°C].

$T_i$ : The outlet temperature of the solar collector [°C].

$T_{Inlet}$ : The inlet of the solar collector [°C].

$\dot{Q}_S$ : The obtained heat from the solar collector [W] can be calculated as follows:

$P_{eff}$ : The power consumed by the compressor [W], can be calculated using the following formula:

$$P_{eff} = U_{eff} \cdot I_{eff} \quad (5)$$

Where:

$U_{eff}$ : The voltage from the grid, is equal to 230 [V].

$I_{eff}$ : The consumed current by the compressor(s) [A].

$E_{loss}$ : Energy loss of the system [W], can be concluded from the equation (6) as follows:

$$E_{loss} = \dot{Q}_H - \dot{Q}_S - P_{eff} \quad (6)$$

### 3. Results

#### 3.1. Heat pump efficiency

The theoretical COP is obtained using CoolPack software for the employed refrigerant R22, providing an idealized representation of the heat pump's efficiency. The p-h diagram is built by plotting the pressure and temperature data captured by sensors at a critical point in the cycle (without considering pressure and temperature drops) as shown in Figure 5A.

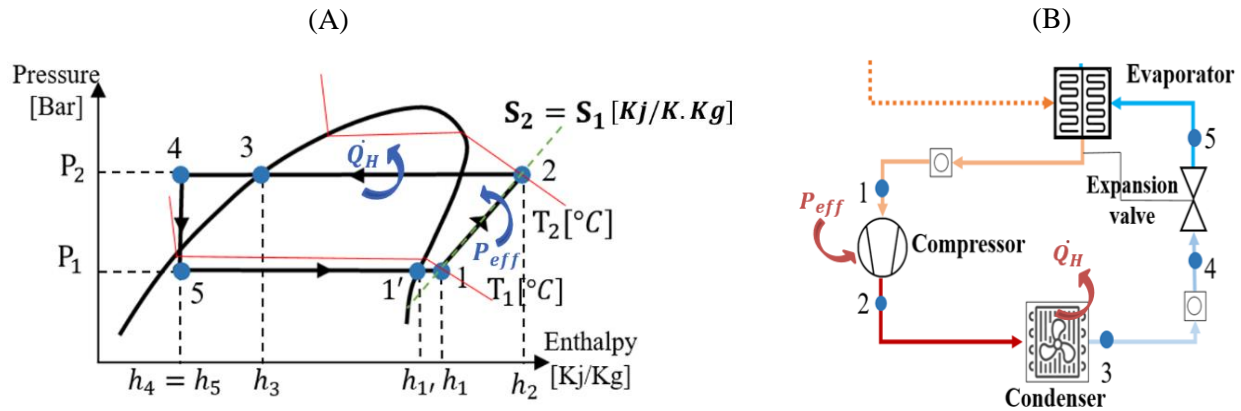


Figure 5. Schematic drawing of the experimental setup: (A) Sample p-h diagram, (B) Heat pump

We calculated the theoretical COP for each day using Equation (7):

$$COP_{HP_{theor.}} = \frac{\dot{Q}_H}{\dot{W}} = \frac{(h_2 - h_4)}{(h_2 - h_1)} \quad (7)$$

Where  $h_1$ ,  $h_2$ , and  $h_4$  are the enthalpies at specific points in the cycle, estimated with the help of the software.

The following equation was used to compute the real COP for each day based on the measured data:

$$COP_{HP_{real}} = \frac{\dot{Q}_H}{P_{eff}} \quad (8)$$

The results are illustrated in Figure 6, accompanied by grey bubbles indicating the average system loss in each scenario.

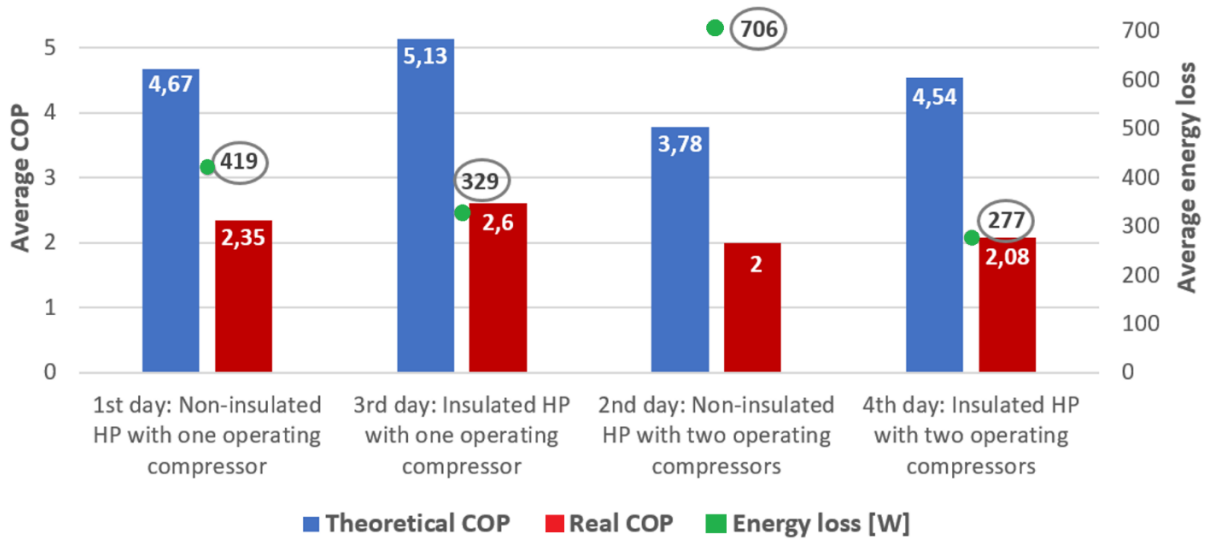


Figure 6. Average COP results and energy losses

It's evident that the theoretical COP values are higher than the real ones, attributed to measurement errors, heat dissipation, and operational parameter discrepancies. However, a consistent correlation exists between the values, with insulation consistently leading to higher COP, as observed:

On the 1<sup>st</sup> and 3<sup>rd</sup> days, the non-insulated heat pump with one operating compressor exhibited higher loss (419 W) compared to the insulated counterpart (329 W). Theoretical COPs were 4.67 and 5.13, while real COPs were 2.35 and 2.6, respectively.

On the 2<sup>nd</sup> and 4<sup>th</sup> days, the non-insulated heat pump with two operating compressors had the highest loss (706 W) among the scenarios, and the loss reached the lowest value when the insulated applied (277 W). Theoretical COPs were 3.78 and 4.54, while real COPs were 2 and 2.08, respectively.

### 3.2. System energy analysis

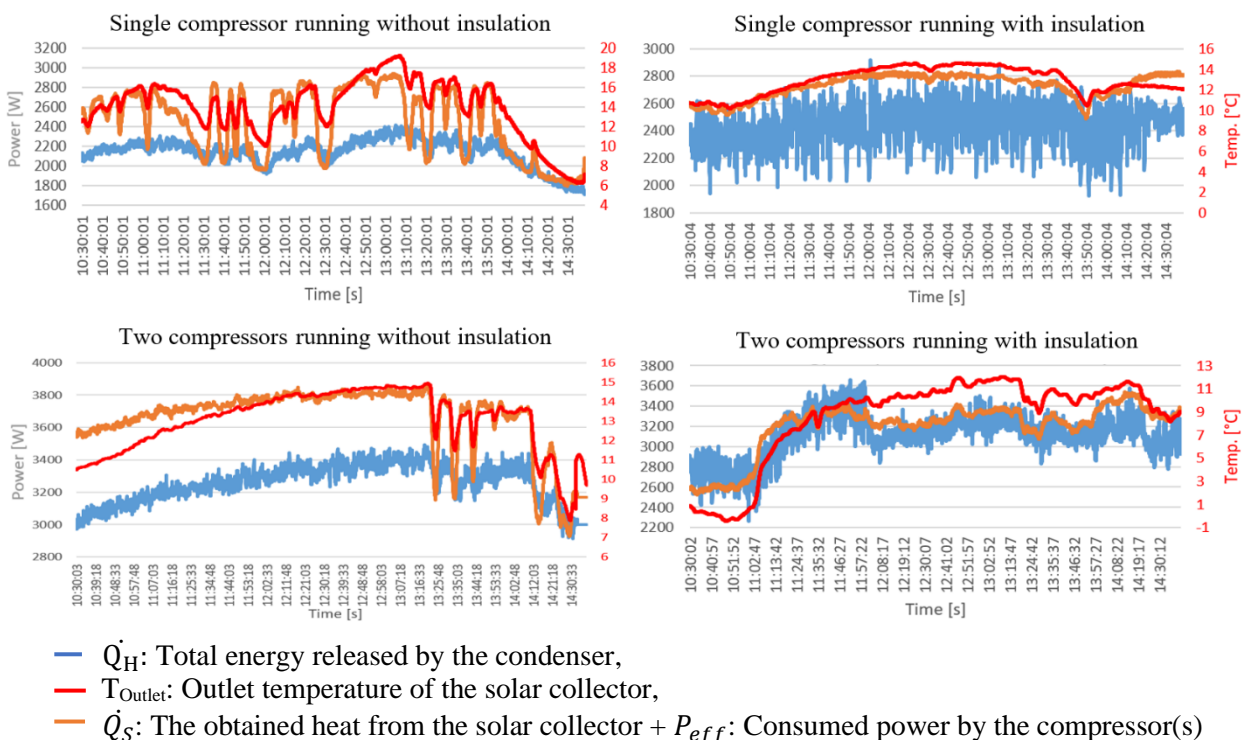


Figure 7. Energy comparison of the system

In this section, we'll understand more about the losses that occur during the system by presenting the condenser's thermal performance concerning the energy consumed by the compressor(s) and extracted heat from the solar plate, as mathematically shown in equation (1). The graphs in Figure 7 exhibit the measured energies besides the outlet temperature of the solar collector, the measurements were conducted throughout the day, however, due to data losses and transient periods, we are adopting the evaluation from 10:30 AM to 2:30 PM (a total of four hours of operation).

The graphical contrast between the orange and blue plots illustrates the energy losses in our system. The alignment is particularly pronounced on days when insulation is applied, underscoring the insulation's efficacy in mitigating losses. A correlation was found between the outlet temperature of the solar collector and the reduction in energy losses. Specifically, a lower outlet temperature corresponded to a decrease in the absorbed heat, consequently resulting in diminished overall system losses.

#### 4. Conclusions

Given that heating is a crucial energy requirement for individuals and businesses worldwide, the importance of well-designed equipment such as the SAHP system becomes essential. This not only translates into tangible cost savings but also contributes significantly to reducing carbon footprints, aligning with the global push for sustainable living. By carrying out methodical experiments and conducting a thorough analysis, we have discovered valuable insights into the operational efficiency of this technology. Our findings demonstrate that the application of insulation aids in achieving a state of perfect reversibility by minimizing energy loss caused by external thermal transformations. Additionally, increasing the operational units of the compressor can further reduce these losses. Furthermore, we discovered that the system was unable to effectively utilize the heat gained by the solar collector, when the outlet temperature of the solar collector increases, the amount of heat acquired increases as well, resulting in system losses. In conclusion, while insulation and compressor functioning are crucial factors in the SAHP, there are additional components inside the system that significantly influence overall efficiency and should be taken into consideration for future studies and designs, such as the evaporator and the solar collector.

#### Acknowledgements

This work was supported by the Stipendium Hungaricum Programme and by the Mechanical Engineering Doctoral School, The Hungarian University of Agriculture and Life Sciences, Gödöllő, Hungary.

#### References

- [1] **Omer, A. M.** (2008). Ground-source heat pumps systems and applications. *Renewable and sustainable energy reviews*, 12(2), 344-371.
- [2] **Carroll, P., Chesser, M., and Lyons, P.** (2020). Air Source Heat Pumps field studies: A systematic literature review. *Renewable and sustainable energy reviews*, 134, 110275.
- [3] **Ghabour, R., & Korzenszky, P.** (2020). Mathematical modelling and experimentation of soy wax PCM solar tank using response surface method. *Analecta Technica Szegedinensia*, 14(2), 35-42.
- [4] **Ghabour, R., Korzenszky, P.** (2021). Identifying the optimum tilting angles for solar thermal collectors using four different modelling factors in Hungary, *Mechanical Engineering Letters* 21, pp. 51-64., 14 p.
- [5] **Géczi, G., Korzenszky, P., Bense, L.** (2013). Ideális körülmények a levegő-víz hőszivattyú uszodatechnikai alkalmazása során, *Magyar Épületgépészet* 62, 7-8 pp. 7-10., 4 p.
- [6] **Géczi, G., Bense, L., Korzenszky, P.** (2014). Water Tempering of Pools Using Air to Water Heat Pump Environmental Friendly Solution, *Rocznik Ochrona Srodowiska* 16 pp. 115-128., 14 p.
- [7] **Thomas, N.** (2015). *Westring Pascal. European heat pump market and statistics report 2015*. Technical report. Brussels: The European Heat Pump Association AISBL (EHPA).
- [8] **Vorushylo, I., Keatley, P., Shah, N., Green, R., and Hewitt, N.** (2018). How heat pumps and thermal energy storage can be used to manage wind power: A study of Ireland. *Energy*, 157, 539-549.
- [9] **Korzenszky, P., Géczi, G.** (2012). Heat Pump Application in Food Technology, *Journal of Microbiology*

*Biotechnology and Food Sciences* 2: 2 pp. 493-500., 8 p.

- [10] **Ghabour, R., Korzenszky, P.** (2022). Linear model of DHW system using response surface method approach. *Tehnički Vjesnik-Technical Gazette*, 29(1), 66-72.
- [11] **Ghabour, R., Korzenszky, P.** (2023). Dynamic Modelling and Experimental Analysis of Tankless Solar Heat Process System for Preheating Water in the Food Industry. *Acta Polytechnica Hungarica* 20: 4pp. 65-83., 19 p.
- [12] **Nuntaphan, A., Chansena, C., and Kiatsiriroat, T.** (2009). Performance analysis of solar water heater combined with heat pump using refrigerant mixture. *Applied Energy*, 86(5), 748-756.
- [13] **Ghabour, R., & Korzenszky, P.** (2021). Technical and Non-Technical Difficulties in Solar Heat for Industrial Process. *Acta Technica Corviniensis-Bulletin of Engineering*, 14(3), 1-18.
- [14] **Ghabour, R., Josimović, L., Korzenszky, P.** (2021). Two Analytical Methods for Optimising Solar Process Heat System Used in a Pasteurising Plant, *Applied Engineering Letters* 6 :4 pp. 166-174., 9p.
- [15] **Fan, Y., Zhao, X., Han, Z., Li, J., Badiel, A., Akhlaghi, Y. G., and Liu, Z.** (2021). Scientific and technological progress and future perspectives of the solar assisted heat pump (SAHP) system. *Energy*, 229, 120719.
- [16] **Hermanucz, P., Géczy, G., and Barótfi, I.** (2021). Modeling and measurement methods for multi-source heat pumps. *Science, Technology and Innovation*, 14(3).

# CONTENT OF No 42/2023

---

## **RAPID DETECTION OF SOIL TEXTURE ATTRIBUTE BASED ON MID-INFRARED SPECTRAL LIBRARY IN SALT AFFECTED SOILS OF HUNGARY**

M. A. MohammedZein<sup>1,2</sup>✉, E. Micheli<sup>1</sup>, B. Rotich<sup>1</sup>, P. N. Justine<sup>1</sup>, A. E. E. Ahmed<sup>3</sup>, H. Tharwat<sup>1</sup>, A. Csorba<sup>1</sup>

<sup>1</sup> Institute of Environmental Sciences – Hungarian University of Agriculture and Life Sciences, 2100 Gödöllő, Páter Károly u. 1., Hungary;

<sup>2</sup> Agricultural Research Corporation, Land and Water Research Centre, Wad Medani, Sudan;

<sup>3</sup> Mechanical Engineering Doctoral School - Hungarian University of Agriculture and Life Sciences, 2100 Gödöllő, Páter Károly u. 1., Hungary;.....5

## **PRODUCTION AND PRODUCTION-INCREASING FACTORS OF BIOCHAR**

V. Madár<sup>1</sup>, A. Betovics<sup>2</sup>, L. Tóth<sup>2</sup>

<sup>1</sup> Pyrowatt Kft., 6120 Kiskunmajsa, Vágóhíd utca 91., Hungary;

<sup>2</sup> Institute of Technology - Hungarian University of Agriculture and Life Sciences, 2100 Gödöllő, Páter Károly u. 1., Hungary;.....14

## **AGRICULTURAL APPLICATIONS OF THE DISCRETE ELEMENT METHOD**

J. Huang<sup>1</sup>, I. Keppler<sup>1</sup>

<sup>1</sup> Institute of Technology - Hungarian University of Agriculture and Life Sciences, 2100 Gödöllő, Páter Károly u. 1., Hungary;.....26

## **LITERATURE REVIEW ON SOLAR ENERGY AND BIOGAS UTILISATION FOR THE DEVELOPMENT OF SCALABLE CO-GENERATION POWER PLANTS**

L. Magó<sup>1</sup>, I. Seres<sup>2</sup>, P. Víg<sup>2</sup>, G. Bércesi<sup>1</sup>, K. Szalay<sup>1</sup>, J. Deákvári<sup>1</sup>, P. Gárdonyi<sup>1</sup>, Z. Kurják<sup>1</sup>

<sup>1</sup> Institute of Technology – Hungarian University of Agriculture and Life Sciences, 2100 Gödöllő, Páter Károly u. 1., Hungary;

<sup>2</sup> Institute of Mathematics and Basic Science – Hungarian University of Agriculture and Life Sciences, 2100 Gödöllő, Páter Károly u. 1., Hungary;.....33

## **MATHEMATICAL MODELLING AND EXPERIMENTATION OF SOY WAX 68°C ENCAPSULATED INTO SOLAR TANK (CASE STUDY)**

R. Ghabour<sup>1</sup>, Y. Amer<sup>2</sup>, P. Korzenszky<sup>2</sup>

<sup>1</sup> Doctoral School of Mechanical Engineering – Hungarian University of Agriculture and Life Sciences, 2100 Gödöllő, Páter Károly u. 1., Hungary;

<sup>2</sup> Institute of Technology - Hungarian University of Agriculture and Life Sciences, 2100 Gödöllő, Páter Károly u. 1., Hungary;.....46

## **AN EXPERIMENTAL INVESTIGATION ON THE EFFECT OF INNER RACE DEFECT ON ROLLING ELEMENT BEARINGS**

M. Albbery<sup>1,2</sup>, I. Szabó<sup>1</sup>

<sup>1</sup> Institute of Technology, Hungarian University of Agriculture and Life Sciences, 2100 Gödöllő, Páter Károly u. 1., Hungary

<sup>2</sup> Doctoral School of Mechanical Engineering, Institute of Technology, Hungarian University of Agriculture and Life Sciences, 2100 Gödöllő, Páter Károly u. 1., Hungary;.....54

## **ENERGY STUDY OF A SOLAR ASSISTED HEAT PUMP (SAHP)**

L. Herzallah<sup>1</sup>, P. Hermanucz<sup>1</sup>

<sup>1</sup> Institute of Technology, Hungarian University of Agriculture and Life Sciences, 2100 Gödöllő, Páter Károly u. 1., Hungary;.....65



